

Chapter 1

Introduction

1-1 Introduction of Organic Thin Film Transistors (OTFTs)

The concept of using the field-effect transistor (FET) was first proposed by in 1930s.[1] In a FET, a capacitor is placed under or above a conducting channel between two Ohmic contacts, which are named as the source and drain electrodes. The carrier density in the channel is controlled by the voltage applying to the capacitor. In 1960s, the first fabricated silicon-based metal-oxide-semiconductor FET (MOSFET) was achieved.[2] Till now, the MOSFET is the most widely used in microelectronics and in integrated circuits. In 1970s, organic FETs (OFETs) have been indicated as a potential electronic device, and Koezuka and coworkers also reported a device with conducting (or conjugated) polymers (CPs).[3-5] Recently, small conjugated molecules, their semiconducting properties have been more recognized, which enables such materials for electronic applications. OFET is on the architecture of the thin film transistor (TFT), which has proven with low conductivity materials, is similar to the case of amorphous hydrogenated silicon (a-Si:H).[6] The performance of OFETs has continuously and now competes with amorphous silicon FETs, which are now applicable to large areas electronics. The charge transport mechanisms in organic semiconductors are also be made and various models developed for the OFETs are also examined in the past ten years. Various materials and fabrication techniques have been detailed and several common OTFT structures were plotted as follows:

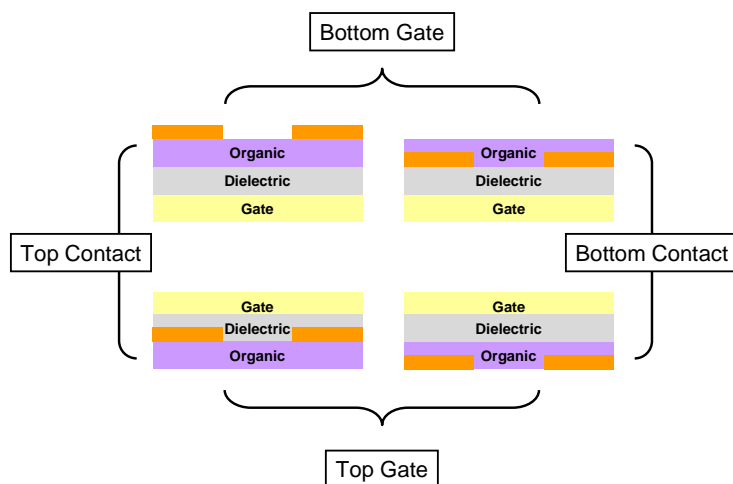


Fig. 1-1 Four fundamental OTFT structures with different electrode and gate configuration.

For high performance OFETs, the organic thin films with high structural ordering are required. Among the proposed candidates for electronic applications, such as large area and mechanically flexible organic electronics, the pentacene-based devices stand out owing to the relatively high field effect mobility and its ability of forming highly ordered films on various types of substrates. It seems to be the best candidates for organic thin film transistors (OTFTs). It is well-known that the charge transport properties of conjugated molecules, such as pentacene or anthracene, are intrinsically correlated with their crystalline structure. For example, with its degree of orientation, and with its grain size, the exact correlations are still not well understood. Hence, controlling and optimizing film quality is essential to develop the device applications by using pentacene. Pentacene ($C_{22}H_{14}$) is a planar molecule, which is composed of five linked benzene rings.[7] In its bulk phase, pentacene is a triclinic structure (space group P1h) with a density of 1.32g/cm^3 . There are two molecules per unit cell arranged within a herringbone configuration. Pentacene is reported to have two phases in the bulk structures. The vacuum-deposited pentacene film forms a structure that refers as the “thin film phase”.[8-10] The pentacene film has been found to coexist

with the “thin-film phase” on evaporated thin films beyond a critical thickness. The charge transport in pentacene film depends on an efficient π -orbital overlap between the molecules and molecular packing in pentacene thin films produce such structures.

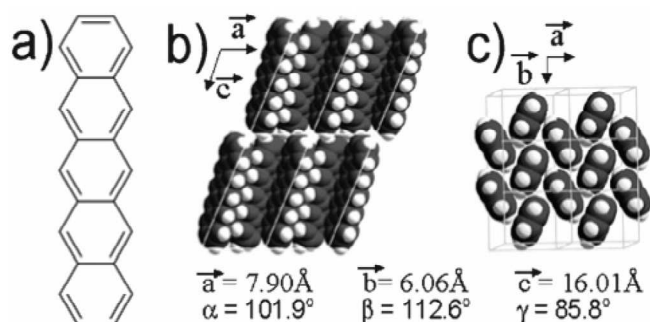


Fig. 1-2 Pentacene chemical and crystalline structures.

[*Chem. Mater.*, **16**, 4497-4508 (2004)]

In crystalline pentacene film, the van der Waals force of the intermolecular bonding and its anisotropy of the individual molecules result in the main differences in its growth mechanisms. These differences bring opportunities for applications but brings new challenges in understanding the fundamental properties of thin films of organic molecular crystals. To control organic thin film growth in vapor phase, it is necessary to adapt the conventional epitaxy models for inorganic molecular beam epitaxy (MBE). A amount of works on pentacene film morphology, degree of order, crystal quality, and nucleation and growth processes in pentacene thin films has been reported.[11-13] Some applications of growth models to explain recent experiments on the nucleation, dislocations, and growth of pentacene thin films are investigated. [14] Though of great importance, we do not attempt here to describe the electronic properties of pentacene films.

1-2 The Fabrication of OTFTs

1-2-1. Organic Molecule Beam Deposition (OMBD)

Inorganic films growth by MBE and organic growth by molecular beam deposition (OMBD) have some similarities and differences. In MBE, the substrate is a clean, single crystal, and the absorbers are usually single atoms or dimmers on the surface. Moreover, the atoms are assumed to be an isotropic surface (sphere) and the orientation of the ad-atom relative to “substrate” or to “other atoms” is irrelevant for the strength of interaction. For the reason, lattice matching is usually a requisite for crystal growth, because it affects stress building-up. In general, thin films grow yield the three modes, which depicted in following Figure: layer-by-layer (Frank-van der Merwe mode), layer-plus-island (Stranski-Krastanov mode), and island mode (Volmer-Weber): [15, 16]

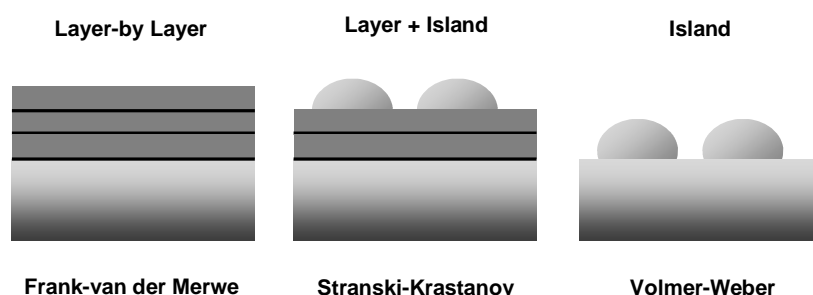


Fig. 1-3 Three types of growth mode in conventional molecular beam deposition.

In the general, the layer-by-layer mode occurs when the atoms diffuse to form two-dimensional (2D) islands and are more strongly bonded to the substrate than to other adatoms. The island mode occurs when the interactions within the adsorbates are stronger than to the substrate, forming three-dimensional (3D) islands.[14] The layer-plus-island mode occurs when the layer formation becomes less favorable and the film develops island after one or more layers lower the free energy. In the case of organic crystals, the interactions between molecules in the crystal are weaker than van der Waals interactions. Besides, the molecules are not spherically symmetric, the

strength of the molecule-molecule and molecule-substrate interactions (the system free energy) depends on the relative orientation of the ad-molecules. Thus, the conditions for a given growth mode will depend on the balance of the anisotropic interactions between the molecules, e.g. their neighbors and the substrate. For example, if the substrate is smooth and flat,[17] molecules have a tendency forming self-assemble crystalline, and regard the crystal orientation of the substrate. The molecules stand nearly vertical and a layer-by-layer growth occurs when the lateral pentacene-pentacene interactions are stronger than the pentacene-substrate or pentacene-pentacene interlayer ones. This opens up the possibilities of multilayer structures and the lattice matching is no longer a criteria.[18] However, there are still some similarities in organic thin film growth and inorganic film. Some cases of coincident epitaxy (as van der Waals epitaxy or quasi-epitaxy) on organic films have been reported. The diffusion-limited and scaling theories have been reported to explain the formation of the initial layer on inert surfaces, and a distributed growth model has also been applied for the subsequent layers.

In general, the crystalline orientation of the pentacene film (especially for the first monolayer) is determined by the balance of the pentacene-substrate and pentacene-pentacene interactions. The experimental results of the influence from substrates on the formation of the first layer and the following layers various substrate materials can be calculated by *ab initio* calculations for pentacene-substrate interactions.[19] When pentacene is deposited onto flat, and smooth substrates, such as the oxide or polymeric dielectrics,[20-21] pentacene molecules stand nearly vertical on the substrate. The (001) plane has the lowest surface energy in pentacene crystals. With a weak interacting or passivated substrate, the pentacene-pentacene interactions are stronger than pentacene-substrate interactions, pentacene will form with (001) plane parallel to the substrate plane, and leave the lowest surface energy.

On the other hand, if the substrate is a more active one, such as clean Si or a clean metal, the interactions between pentacene-substrate will become more important and may involve charge transfer at the interface. This makes pentacene molecules lie flat on the surface and some typical morphologies are not reproduced.

The structure obtained in the evaporated thin films has been referred to in the literature as the “thin-film phase”. Recently, the “grazing incidence X-ray diffraction” (GID) [14, 22] data from a single layer of pentacene grown on silicon oxide estimate the unit cell vectors $a:7.578\text{\AA}$, $b:5.909\text{\AA}$, and $c:89.95^\circ$. Before the “thin-film phase” was identified as different from the bulk, electron diffraction experiments of pentacene on estimated $a:7.41\text{\AA}$ and $b:5.76\text{\AA}$. [23] However, a triclinic structure was reported recently on salt substrates, and another orthorhombic cell with four molecules in the unit cell was also reported (although in that structure molecules were not standing vertical on the substrate). It is clear that increasing the substrate temperature and lowering the deposition rates will decrease the nucleation density and therefore increase the average grain size. Indeed, there exists a considerable amount of data to support this prediction. The “thin film phase” of crystalline domains in pentacene thin films is a substrate-induced structure different from the bulk. It has been reported that nucleation of the bulk phase starts beyond a certain critical film thickness. [24]

1-2-2. Spin-coating and Inject Printing Process

Besides vacuum deposition, two approaches have also been used to obtain organic semiconductor thin films from solution: [25] (1) a soluble precursor from solution and converted into the solid state semiconductor; or (2) direct deposition of a soluble and curable semiconductor. The solution-process can be applied on the fabrication of large area devices. The process is free of vacuum chamber or instrument and the pumping

time. Therefore, the fabrication cost can be significantly lowered. The well-known solution-processes are “spin-on coating” and “inject printing”. The economical deposition can be accomplished by the spin-on coating within a very short time. The patterning method may also be achieved in a single step with the aid of inject printing. Heating also plays an important role in the solution-process. The solvable materials for solution-process sometimes are the precursor of organic semiconductor or the mixture of conjugated oligomers with solvents. Most conjugated oligomers and polymers used as semiconductors are insoluble in common solvents. Sometimes, these may either affect molecular packing or increase the π - π stacking distance between molecules and result in mobility changes.[26] In addition, the mobility of these materials is low may due to partially cross-linked during the polymerization process and results in low molecular ordering. To improve such issues, several researchers have synthesized soluble precursors, which can be converted into the final semiconductor intrinsic layer after film depositio. Pentacene transistors with high mobilities have been reported using this approach.[14] Oligothiophene based transistors have also been reported with reasonable mobilities. High mobilities have been reported with several oligomers by optimizing the deposition conditions. Both spin-coating and solution-casting are commonly used for solution deposition. In the spin-coating method, the solvent dries relatively fast allowing less time for molecular ordering compared to that in solution-casting.[27-30] But the film uniformity is usually better for spin-coated films. These films can be annealed afterward to improve molecular ordering as discussed later. For materials with tendencies to form highly ordered molecular packing, it was found that even spin-coated films can achieve very high motilities. The structure analysis with grazing incidence wide-angle X-ray diffractions (GIWAX),[31] indicated that the polymer conformations are similar to the solvent used for film preparation. For polymer semiconductors, their molecular

weight and polydispersity also have great impact on the morphology of their thin films. Recent work has shown that the mobility of spin-coated regioregular poly(3-hexylthiophene) differs by several orders of magnitudes depending on the molecular weight of the polymer. The mobility was found to increase with molecular weight. Low-molecular-weight PHTs (number-averaged molecular weight less than 10000) were found to form rodlike morphology, whereas high-molecular-weight polymers formed isotropic nodules. It is unclear whether the difference in mobility is due to the sharper interface between rods in the low-molecular-weight films or the fact that the larger-sized molecules require less hopping between molecules. A simple diagram of explaining the spin-coating process is:

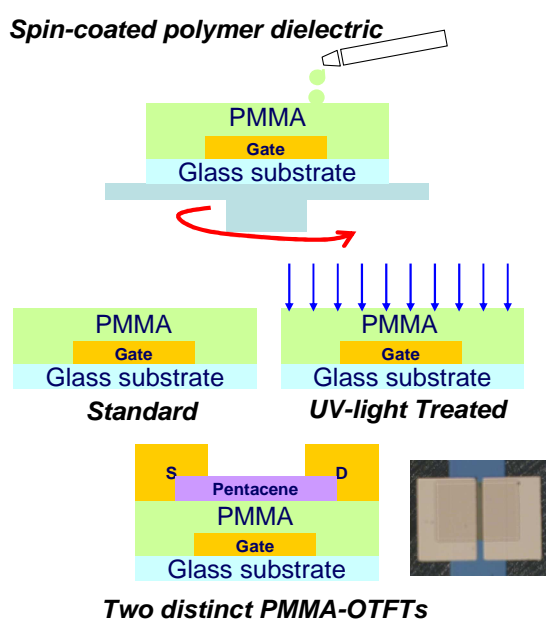


Fig. 1-4 The solution-based process of fabricating OTFT dielectric and organic film.

Alternative methods of patterning from the printing industry are being examined to replace photolithographic patterning. Printing methods, such as flexographic marking and jet printing, are used routinely to make large-area, low-cost high-resolution documents and graphics. Important questions for these technologies are whether they

can achieve the multilevel registration (better than 10 μ m) required for backplanes and whether they can be performed in high yield with very low numbers of defects.

Contact printing comprises a set of patterning methods where a pattern of ink is defined on a flexible stamp and then transferred to a substrate by mechanical contact. The stamp may be directly patterned with features, inked, and then placed into contact with a substrate, such as in flexographic printing, or the ink may be transferred from a rigid, patterned master to a flexible transfer surface that is placed in contact with the substrate, such as in offset printing. Because contact printing is purely mechanical, no optical exposure system is required to define a pattern, reducing the complexity of the patterning tool. One of the first printing methods examined to pattern conductors in large AM-TFT backplanes was offset printing. A UV-curable ink [32] was placed in patterned wells in a rigid glass plate and then transferred to a silicone-based roller that was placed into contact with a metallic film. The transferred ink was then cured by UV exposure and used as a wet etch resist. Features of 35 μ m with separations of 10 μ m were created in metals and silicon using this technique. While this method was used successfully to fabricate poly-Si TFTs, its further use requires exploration of inks that are adequate etch resists and have low ionic impurities, which can contaminate dielectric and organic semiconducting layers. The physical limits of micro scale offset processes have been examined and depend critically on the capillary, viscous, and adhesive forces on the ink. One of the most widely researched techniques for patterning metallic conductors is the printing of a patterned SAM of an organothiolate that is used as a wet etch barrier on a metal (Ag, Au, Pd, Cu). Micrometer-scale features with edge resolutions of >200nm with gold and >75nm with palladium can be readily patterned. The drawback of the use of SAMs as etch resists is the limited number of metals that can be patterned. The gate electrodes of an AM-TFT backplane are typically fabricated from Al or Mo-Cr due to their low cost, high conductivity, and

compatibility with PECVD deposited dielectric layers. Micro contact printing has been used to fabricate both the gate and the data levels of prototypes of AM-TFT backplanes. The IBM group has developed a iCP-based process for gate electrodes based on etching of an electroplated copper layer. They used electroplated Cu layer as an etch mask for an underlying electrolessly plated NiB layer.[33] After definition of the NiB electrodes, they removed the Cu layer by wet etching leaving only the NiB layer. This process has been performed on 15-in. glass substrates. Rogers and coworkers have fabricated the source and drain level electrodes of an AM-OTFT backplane using gold electrodes that were patterned by iCP. They patterned 10 μm features with registration of $>50\mu\text{m}$ to electrodes defined by photolithography on a 5-in. by 5-in. substrate. In other work, a gold film supported by a PDMS film was patterned by iCP and then laminated onto an organic film to form the source and drain contacts of a TFT. This method creates a staggered OTFT, a structure that typically has lower contact resistance than a coplanar structure. The main challenges for soft lithographic techniques are the fidelity of patterned features and registration over multiple patterned levels. A method referred to as “wave printing” [34] that uses a traveling air pressure wave to press a stamp into contact with a substrate has been shown to reduce distortions. The commercially demonstrated inject printing system is shown:



Fig. 1-5 The inject-printing system and its printing head [Fujifilm Dimatix, Inc]

1-2-3. Dielectric and Interface Engineering

The carrier transport in organic semiconductors is different from that in in-organics. Organic semiconductors should be viewed as “molecular solids”, even in the case of polymeric or organic semiconductor. As a result, the dielectric will affect carrier transport and mobility much stronger than that in inorganic materials. First, the dielectric can affect the morphology of organic semiconductor and the orientation of molecular,[35] with the balance between the dielectric semiconductors (especially in bottom interface). Second, the interface roughness and sharpness will also be influenced by the dielectric itself,[36] the deposition conditions, and the surface energy. Studies of interface roughness indicate that it is an important key to high performance OFETs. Increased roughness will lead to valleys in the device channel region, which may act as carrier traps. Roughness also degrades the growth of uniform,[37] crystalline domains and the nucleation density. Another effect on OFETs performance is gate voltage dependent mobility and the variation of threshold voltages. A reasonable possibility is that the carrier concentration controlled by the across gate-dielectric by changing the occupation level of the interface density of states (DOS). At the same time, the gate field may force the carriers to travel in the vicinity of the interface in a 2D fashion rather than allowing them to optimize their route through more efficient paths through the 3D bulk.[36]

The first OFET devices were deposited on Si substrates with SiO₂ as the insulator. The choice of using Si substrate was convenient, as SiO₂ can be thermally grown on the heavily doped Si wafers, which served as the gate electrode. SiO₂ has been well-optimized to form a defect-free interface with Si, its top surface (relevant for an OFET) is much less defined, as it is subjected to ambient processing steps during OFET fabrication. The SiO₂ surface is likely to contain Si-OH defects and water, depending on its processing method. Alkali ions inside the oxide film influence

further the operation of device characteristics, particularly hysteresis and threshold voltages.[38] Surface states on inorganic oxides are a particular problem leading to interface trapping and hysteresis. The growth of pentacene on SiO₂ has been widely studied under different deposition conditions. Importantly, it was demonstrated that the nucleation density was strongly influenced by the substrate quality: grain sizes were larger on Si (001) surfaces passivated with a cyclohexene layer than on SiO₂. [39] Dendritic growth in pentacene is often associated with high mobility and is typically achieved when the substrate temperature is between 20 and 130°C, with a deposition rate of 1-3Å/s. How much the dielectric substrate matters is clearly demonstrated by the large number of surface treatment studies in the literature. Surface treatments such as hexamethyldisilazene (HMDS) were first employed at Philips in the early 1990s to protect SiO₂ and define a uniform layer on top of it before depositing the organic semiconductor (OSC).[40] HMDS is used in standard silicon processes before applying photoresists for better adhesion. Several studies investigated the properties of self-assembled monolayers (SAMs), such as HMDS, octadecyltrichlorosilane (OTS), other silanes, alkanephosphonic acid, which covalently attached to the SiO₂. [41] Mobility increase has been characteristic for many organic semiconductors. A possible explanation for increased field-effect mobility is due to the increased grain size of the semiconductor. This is assisted by high molecular surface mobility and reduced interaction with the hydrophobic substrate surface. Surface energy is significantly reduced on “silanized” substrates with a very high contact angles (>100°). Increased grain size associated with SAMs was reported for pentacene. One suggestion, indicated by scanning electron microscopy (SEM) and X-ray diffraction (XRD), is that OTS may increase the density of flat-lying molecules and is reasonable for increasing the holes mobility in pentacene OTFTs. Longer alkyl and branched alkyl chains have also been particularly

effective, increasing the mobility up to $3.3\text{cm}^2/\text{v}\cdot\text{sec}$ and, although hydrophobic,[42] reported to lead to a high degree of continuity in the first few molecular layers. The long alkyl chains may also improve the roughness of the dielectric layer. Interestingly, when studying a range of silane treatments, the IBM group found that the hydrophobicity alone could not explain the observed differences in pentacene performance.[43] The orientation of the terminal groups on the SAM seemed to be a key; terminal bonds parallel to the surface produced highly ordered films with high carrier mobility. The most commonly accepted and optimized orientation for pentacene is the long axis of the molecule being perpendicular to the substrate. The role of the dielectric surface treatments is still not entirely clear and may be a combination of several effects such as influencing surface energy and smoothness, inducing molecular orientation, and neutralizing surface defects. The commonly used interface modification is illustrated as:

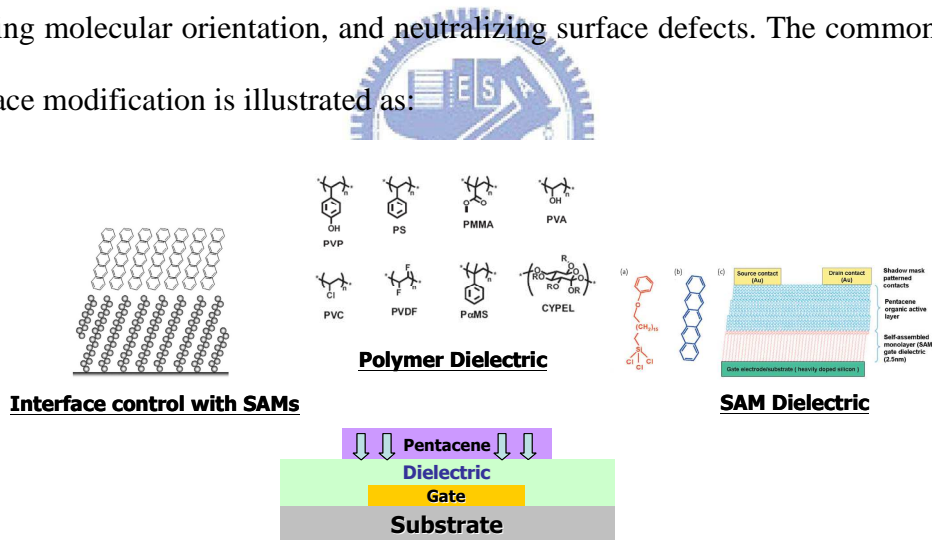


Fig. 1-6 The surface treatment on dielectric for OTFT fabrication.

[*Nature (London)* 431, 963 (2004)]

The dielectrics discussed up to now have all been the “bottom gate” devices. The deposition of inorganic dielectrics on top of the OSC as a “top gate” device would be difficult. The surface treatments employed on inorganic material would be practically impossible to use in top gate devices. Organic dielectrics, however, offer the freedom to form up both top and bottom gate devices more easily by the use of solution-based

and printing techniques. Some organic insulator materials reported in the literature. Pentacene growth was compared on organic and inorganic dielectrics such as SiO₂, Si₃N₄, PVP, and benzocyclobutene (BCB), all in bottom gate systems. Some crystalline sizes difference was observed, but it did not lead to significant differences in mobility or subthreshold swing.[44] It was suggested that once deposition conditions are optimized to obtain similar morphology and the intrinsic behavior of the pentacene device. The surface roughness, however, appeared to be a very important parameter, and polymeric insulators can generally produce smooth surfaces. In a very interesting study, the 3M team used thin, 10nm layers of poly (α-methylstyrene) (RMS) on top of the SiO₂ dielectric.[45] Pentacene film was then be deposited on the RMS layer yielded mobilities up to 5cm²/v-sec, independent of the molecular weight of the styrene polymer. The presence of the RMS layer was the strongest contributor to high mobility among the other parameters studied, such as chamber pressure, deposition rate, and the number of crystal grains. It was also found that the crystal size or the type of grains was difficult to correlate with mobility.[45] The use of organic polymers such as PMMA has generally resulted in higher mobility and better device reliability compared to the process dependent SiO₂. A good gate insulator should preferably have no dependence of capacitance on frequency. Interestingly, mobilities as high as 0.1-0.5cm²/v-sec were obtained using a relatively polar insulator, PVP in oligothiophene FETs. The presence of long alkyl chains may provide some screening effect from dipolar effects as well as from interface defects on the insulator.

1-3 Motivation

The goal of our study is to fabricate high performance OTFT with pentacene active layer. We investigated new dielectric material with low surface energy, which surface

energy is matched to the pentacene film. The dielectric leakage and its mechanism were also studied by changing the process parameter for the optimization of dielectric properties. We also tried to develop the OTFT photon and gaseous detectors. By using the dielectric treatment, we tried to improve the photo sensitivity and investigate its interaction process. The gaseous detection was also verified in isolated chamber.

1-4. Organization of Thesis

1-4-1. High Performance Aluminum Nitride Organic Thin-Film Transistors

The RF-sputtered AlN film was used as the gate insulator in pentacene-based OTFTs. With the dielectric breakdown field larger than 5MV/cm and the relative electrical permittivity as 7 in the AlN film, the proposed TFTs exhibit low operation voltage, low subthreshold swing ($\sim 0.4\text{V/decade}$) and high on/off current ratio ($>10^6$). By adjusting the AlN sputtering process, it was found that smooth morphology of AlN film (surface roughness $<2\text{\AA}$) can be obtained by lowering down the process temperature. This atomically smooth dielectric surface leads to the growth of large pentacene grains and improves the leakage current and also the field effect mobility.

Besides, we tried to reduce the AlN gate-leakage by altering the reactive gas (Ar/N₂) ratio during the sputtering process. Thus, the thin ($<100\text{nm}$) and low-leakage AlN gate dielectric was achieved. The demonstrated AlN-OTFTs can be operated at low voltage ($<5\text{V}$). Low threshold voltage (-1.5V) and extremely low sub-threshold swing ($\sim 104\text{ mV/dec}$) were also obtained.

Finally, we reported on the low-voltage ($<5\text{V}$) pentacene-based organic thin film transistors (OTFTs) with a hydrophobic aluminum nitride (AlN) gate-dielectric. In this work, a thin (about 50nm), smooth (roughness about 0.18nm) and low-leakage AlN gate dielectric is obtained and characterized. The AlN film is hydrophobic and the surface free energy is similar to the organic or the polymer films. The

demonstrated AlN-OTFTs were operated at a low voltage (3V-5V). A low threshold voltage (-2V) and an extremely low subthreshold swing (~170mV/dec) were also obtained. Under low-voltage operating conditions, the on/off current ratio exceeded 10^6 , and the field effect mobility was mobility was $1.67\text{cm}^2/\text{V}\cdot\text{sec}$.

1-4-2. High Photo Responsivity of Pentacene-based Organic Thin-Film Transistors

A simple UV-treatment process on PMMA dielectric is proposed to enhance photo responsivity of pentacene-based OTFTs. The UV-treatment creates excess negatively-charged sites on the PMMA dielectric, which makes the device exhibiting a large photo-induced current and prolongs the recovery of persistent conductance. In order to describe time-dependent photo-induced current, equations with double time constants are proposed. Based on time-constant fittings, slow-varied response is found to be influenced by the UV treatment. The rapid-varied response is independent of gate bias and UV treatment. A plausible model for spatial carrier-distribution is discussed and proposed to describe this observed phenomenon.

1-4-3. Gated-Four-Probed OTFTs in Ammonia (NH₃) Gas Sensing

Pentacene-based organic thin-film transistors (OTFTs) were used as ammonia (NH₃) gas sensors in this study. The electronic characteristics of OTFT, such as drain current, threshold voltage, and field-effect mobility were sensitive to variations in NH₃ concentration. When NH₃ concentration was increased, drain current and field-effect mobility were reduced and threshold voltage negatively shifted. By using Gated-four-probed analysis, the effects of NH₃ gas on pentacene film and contact resistance were investigated. It was also found that device dimensions were an important factor, influencing the behavior of field-effect mobility in OTFT gas

sensing.

1-4-4. Vertical Channel Organic Thin Film Transistors

We had fabricated vertical channel organic thin film transistors with channel length smaller than 100nm. It is found that Fowler-Nordheim tunneling is the dominant mechanism to explain this ultra short-channel device behavior. To improve the gate control capability, meshed-like source electrode pad had been used. This significantly lowers down the gate and drain driving voltage ($<10\text{V}$), improves the saturation characteristics and reduces the leakage current. The improvement may be due to the fringing field around the source electrode that suppresses the tunneling effect.



Chapter 2

Theoretical Backgrounds

2-1. Transport in Organic Semiconductors

2-1-1 Molecule Orbits and Localized/Delocalized States

In the molecular theory, the electrons distribute around the nuclear molecule. The electron motion can be described by the wave function. The molecular orbits are formed by the linear combination of atomic orbits. Generally, we name such molecular orbit method as linear combination of atomic orbital (LCAO).[1] The molecular orbits is similar to the atomic orbits, a specific molecular orbit can be occupied by a pair of electrons, which has different spin state, respectively. For a simplified case, we can consider a two atom wave functions case: [2, 3]

$$\Psi = a \cdot \Phi_a + b \cdot \Phi_b$$

Ψ is the molecular orbit, which is a linear combination of two different atomic wave function Φ_a and Φ_b with constant a and b , respectively. We may solve the Schrödinger's equation to obtain the energy E as:

$$\begin{aligned}\widehat{H}\Psi &= E\Psi \\ \widehat{H} &= -\frac{\hbar^2}{2m}(\nabla_a^2 + \nabla_b^2) + V_a + V_b \\ E &= \frac{\int \Psi^* \widehat{H} \Psi d\tau}{\int \Psi^* \Psi d\tau} = \frac{\int (a \cdot \Phi_a + b \cdot \Phi_b)^* \widehat{H} (a \cdot \Phi_a + b \cdot \Phi_b) d\tau}{\int (a \cdot \Phi_a + b \cdot \Phi_b)^* (a \cdot \Phi_a + b \cdot \Phi_b) d\tau}\end{aligned}$$

Where \widehat{H} is the system Hamiltonian with V_a and V_b . We may obtain the energy E as:

$$\begin{aligned}E &= \frac{a^2 H_{aa} + 2ab H_{ab} + b^2 H_{bb}}{a^2 + 2ab + b^2} \\ (H_{aa} - E) \cdot (H_{bb} - E) - (H_{ab} - E \cdot S_{ab})^2 &= 0\end{aligned}$$

$$H_{ij} = \int \Phi_i^* \hat{H} \Phi_j \cdot d\tau, S_{ij} = \int \Phi_i^* \Phi_j d\tau$$

We may let $H_{aa} = E_a$, $H_{bb} = E_b$, and $H_{ab} = \beta$. We will get the split energy levels as:

$$E_I = \frac{1}{2}[(E_a + E_b) - \sqrt{(E_a - E_b)^2 + 4\beta^2}]$$

$$E_{II} = \frac{1}{2}[(E_a + E_b) + \sqrt{(E_a - E_b)^2 + 4\beta^2}]$$

As a result, we may plot the energy diagram to illustrate the molecular orbit energy.

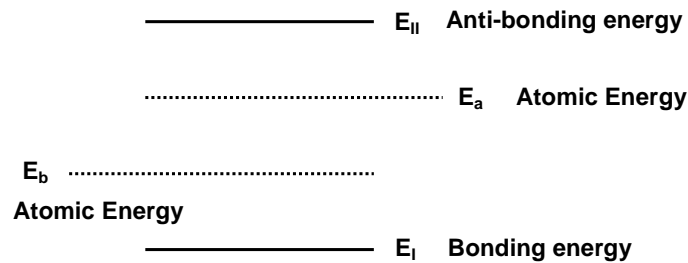


Fig. 2-1 The bonding and anti-bonding molecular orbit energy.

The molecule energy level E_I is lower than the lowest atomic energy level E_b , which energy level (state) is named as “bonding-state”. On the other hand, the molecule energy level energy level E_{II} is higher than the highest atomic energy level E_a , which energy level is named as “antibonding-state”.^[4] In the view of spatial orbit distribution, we may plot the corresponding molecular orbit Ψ_I and Ψ_{II} for E_I and E_{II} as a diagram of:

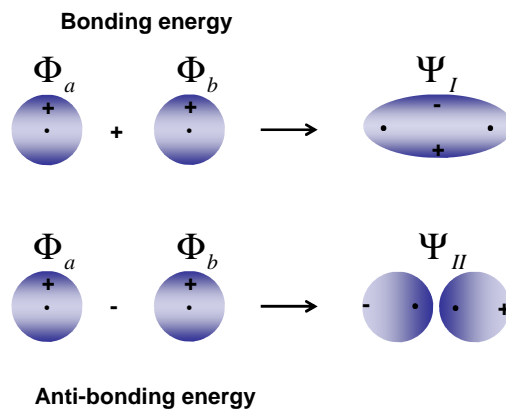
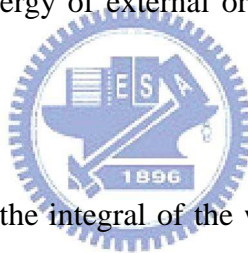


Fig. 2-2 The bonding and anti-bonding molecular orbitals.

The electrons are occupied from the lowest energy level to the highest level. When the atomic orbitals form into the molecular orbitals, those will follow three principles.

(a) Energy Similar

If we consider from the view of energy difference between E_a and E_b , the lower energy difference will result in a more stable molecule structure. That implies the total system energy of the molecule structure is also lowered with the decrease of energy difference. If $E_a = E_b$, that will form a molecule orbit efficiently with a strongest bonding force. If $|E_a - E_b| > 0$, the bonding force of the molecule orbit will slightly reduced. If $|E_a - E_b| \gg 0$, it will be hard to form a molecular or crystal. We may summary that if the electron energy of external orbit is similar, that will form up a molecular orbit more easily.



(b) Maximum Superposition

As we previously stated, β is the integral of the wave function overlap. The larger β indicates the more the wave function overlap. A larger β will also result in the more stable molecule orbit.

(c) Symmetric

The parameter S_{ab} and β is the wave function integration and energy integration between two atomic orbitals, respectively. If the orbit has high symmetry and high atomic orbital overlap, and the wave function has similar superposition symbol, which will be an effective bonding.

In the theory of molecule orbit, the orbitals are generally classified into (a) σ orbital, (b) π orbital, and (c) δ orbital, respectively.[5] In σ orbital, we can not observe any nodes of the molecule orbit when we watch the orbit from its axial. In π orbital, it will be an anti-symmetry structure and there exists a surface with nodes on it. In δ orbital,

the electron cloud is distributed in two different directions and this orbit has two surfaces with nodes. We may illustrate these orbits as:

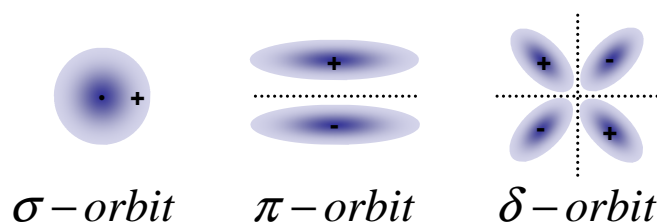


Fig. 2-3 The σ bonding, π bonding and δ bonding molecular orbitals.

The dashed-line is the node surface and the illustration is viewed from one side of the molecule axial.

As for the organic materials, the fundamental composition is come up with carbon (C) and hydrogen (H) atoms. The σ orbit may form up by the hybrid orbit of 1s hydrogen orbit and sp^3 carbon orbit. The π orbit is formed up by the un-hybrid p orbit, which is perpendicular to the sp^2 surface. Unlike the σ orbit, the electron is not only fixed on a specific location (localized) but it can move inside the whole molecule orbit (delocalized).[6] From the view of solid state physic, the localized electron is usually captured at a fixed place, such as the defect states, potential well, and other trap states. If the electron can move freely in the material, such as the periodical lattice or organic crustal, it will be viewed as a delocalized orbit. The delocalized orbit which owns π bonding is named as “conjugate molecule” .[7]

Due to the insufficient of long term lattice structure, the band-like carrier transport can not well satisfy the experimental results. The use of momentum and wave vector \vec{k} in organic electronic states is no more valid. Since the density of states and the energy band structure is determined by the electronic bonding, we should reconsider and modify the band theory in organic materials. The energy band in the organic material is differed from the inorganic material. In the organic materials, there is still

existed several electronic states inside the energy gap (E_g). The amorphous structures should be the origins of these electronic states,[8] which also distribute inside the organic material.[9] When the carrier travels inside the organic material, the long term lattice order is no more existed; as a result, the carrier will be scattered more serious in organic materials. Hence, the mean free path of the carrier will be reduced significantly. The carrier is more likely to be localized at some specific molecule or electronic state. The carrier can only travel inside the material by hopping or tunneling between these electronic states. Only when the carrier density and energy is increased, the carrier mean free path will increase at the same time. The carrier will turn into the extended states, as show in the following diagram, and it will travel with a higher mobility.[10]

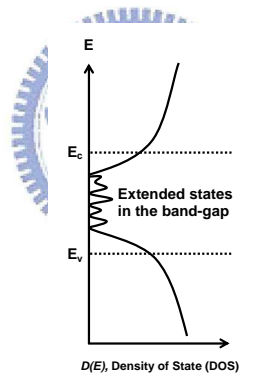


Fig. 2-4 The band diagram of extended states and mid-gap states.

2-1-2 Energy Band and Tunneling Model

After the observation of “negative” temperature coefficient in drift mobility in organic material, the Bloch band theory for carrier transport was proposed.[11] Some assumption was also considered: (a) The periodical potential approximation, (b) The electron-lattice interaction is small, and (c) The multiple structures of individual atoms. Besides, the carrier transport in organic is from the limitation of narrow band. From the uncertainty principle, if we consider the bandwidth W , which should follow

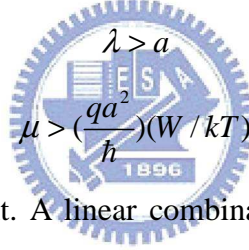
the inequality relation:

$$W \cdot \tau > \hbar \quad \text{and} \quad \tau = \frac{\lambda}{v}$$

τ is the relaxation time of carrier between scatterings, λ is the mean free path, and v is the drift velocity. If the bandwidth is less and $W < kT$, the carrier drift mobility is:

$$\mu = \left(\frac{q}{kT}\right) \langle \tau v^2 \rangle$$

We further estimate the mean drift velocity $\langle v^2 \rangle^{\frac{1}{2}}$, will at the order of v_{\max} . The v_{\max} is equal to $\frac{Wa}{\hbar}$, we may also estimate the approximated mobility by using the small mean free path and narrowband, we may rewrite the mobility in organic material as:



$$\lambda > a$$

$$\mu > \left(\frac{qa^2}{\hbar}\right) (W/kT)$$

Where a is the lattice constant. A linear combination of molecular wave function and potential well with Hückel's approximation is: [12]

$$\psi_k(\mathbf{r}) = \frac{1}{\sqrt{N}} \sum_{n=1}^N \exp(j\mathbf{k} \cdot \mathbf{r}_n) \cdot \phi_n(\mathbf{r} - \mathbf{r}_n), \quad V(\mathbf{r}) = \sum_{n=1}^N V_n(\mathbf{r} - \mathbf{r}_n)$$

If we further consider the modified assumptions (a) symmetric and anti-symmetric molecular wave function in unit cell, (b) the tail of wave function is also reconsidered, and (c) neglect three-center integral, we may instead the wave function as:

$$\psi_k(\mathbf{r}) = \frac{1}{\sqrt{N}} \sum_{l=0}^{N-1} (\pm 1)^l \exp(j\mathbf{k} \cdot \mathbf{r}_l) \cdot \phi(\mathbf{r} - \mathbf{r}_l)$$

By solving the Hamiltonian $H = -\frac{\hbar^2}{2m} \nabla^2 + V(r)$, we may observe the energy:

$$E_{\pm}(k) = \frac{\int \psi_{\pm}^* H \psi_{\pm} d\tau}{\int \psi_{\pm}^* \psi_{\pm} d\tau} = E_0 + \sum_n E_n + \sum_l (\pm 1)^l E_l \cos(\mathbf{k} \cdot \mathbf{r}_l)$$

where E_n and E_l are:

$$E_n = \int \phi^*(\mathbf{r}) \cdot V_n(\mathbf{r} - \mathbf{r}_n) \cdot \phi(\mathbf{r}) d\tau$$

$$E_l = \int \phi^*(\mathbf{r} - \mathbf{r}_l) \cdot V_n(\mathbf{r} - \mathbf{r}_l) \cdot \phi(r) d\tau$$

E_0 is the energy for isolated ion-pair from infinite separation, E_n and E_n represents the intermolecular resonance integral. Thus, we may obtain the relationship between wave vector k and energy and band structure.

In the early 1950s, Eley *et al.* [13] had proposed the “tunneling” model for organic materials. This model describes electron in a given π -orbit of one molecular may tunnel to the other higher energy levels (excited states) of neighbor molecular. The tunneling process is energy conserved and the other higher energy levels (excited states) may be a singlet or a triplet states. The tunneled electron in the neighbor molecular may return to its ground state or tunnels to the next neighbor molecular. In general, the electron has higher probability to tunnel to the next neighbor molecular. When the excited electron is situated in the triplet states, its life time will be prolonged and the probability of tunneling to the next neighbor molecular will also be increased. We may explain the process by using the following diagram. In an idea potential model, the potential barriers are located between the molecules and separate the π -orbits. However, in real cases, Kemeny and Rosenberg [14] proposed that the potential barriers should be a combination of Coulomb potential and the potential of electron affinity from the original molecule. As a result, the actual potential barrier should be smoother and more like a triangular potential barrier. This barrier has better approximation to the experimental result and barrier width is smaller for electron tunneling in a high energy levels. When a carrier is occupied at higher energy, the potential barrier width will lower. As a result, the tunneling probability will also be increased at the same time. However, the potential barrier widths between molecules are still not well verified, it is usually assumed that the barrier width is at the order of

10Å or less. In some organic material with periodic crystal, the tunneling model is also considered as a band-like model for carrier transport in organic material.

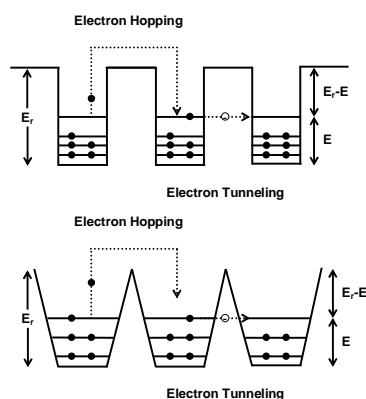


Fig. 2-5 Tunneling model for organic transport.

2-1-3 Tunneling and Hopping Model

In general, the carrier transport in organic material is still not well described by the band model. It is due to the carrier mobility is low (at the order of $1 \text{ cm}^2/\text{V}\cdot\text{sec}$ or less) and experimental results are also not good agreed with the theoretically prediction. In conventional, the organic material is narrow band and results in a band with high density of states (DOS).[15] When a carrier travels in the organic materials, it follows the momentum and energy conservation. As a result, the single phonon emission and annihilation will not valid to explain the transport. The multiple-phonon process with random electron motion should be a more suitable model to describe the carrier transport in organic material. Hence, the suitable model is usually named as “hopping model”, which describes the random jumping carriers between states. The transition between the “band-like” and “hopping-like” process may be determine by the carrier (electron/hole)-lattice (or the oscillator phonons) interaction.[16] For example, if the interaction between carrier and the lattice (inter-molecular) is larger than the interaction between carrier and internal nucleus (intra-molecular), it will be a “hopping-like” process.[17] We may judge the process more quantitatively by using

the carrier relaxation time constant τ . The typical inter-molecular vibration period (τ_{inter}) is about 10^{-12} sec and the intra-molecular vibration period (τ_{intra}) is about 10^{-14} sec. We will discuss the hopping process by the following two groups of time constant.

The Rapid Relaxation Time ($\tau < \tau_{\text{intra}} < \tau_{\text{inter}}$)

The carriers will move quickly in the materials, the lattice vibration (inter- or intra-molecular) is viewed as a small perturbation for motion carriers. The scattering effect from the lattice is not significant and the scattering probability for carriers is low. The carriers can travel freely through several molecules (lattice sites) and then suffer the scattering. The carrier motion can act as a traveling wave and the “band-like” model is valid to describe the carrier transport.

The Slow Relaxation Time ($\tau_{\text{intra}} < \tau < \tau_{\text{inter}}$)

The carriers usually stay on specific molecules (lattice sites), however, the nucleus will move to new equilibrium sites at the same time. When the carriers stay on the specific molecules, that will polarize the molecules. It will also result in a new self-trapping site and form polarons. In most of the organic materials, the inter-molecular vibration frequency is slow, which is also related to the acoustic phonon and the carrier-vibration interaction is weak. On the contrary, the intra-molecular vibration is fast, which is related to the optical phonon and carrier vibration, and such interaction is strong.

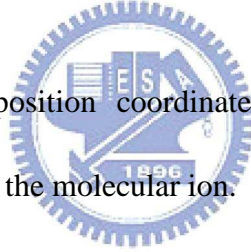
In general, the carrier-phonon interaction is strong and mainly related to intra-molecular in the hopping model. The carrier velocity is usually also determined by the phonon velocity. In the early stage of hopping model, a model of linear interaction model between charged carrier and optical phonon was proposed by Holstein. But the linear interaction model can not well describe the temperature

dependent mobility in some organic aromatic material. Afterward Munn and Siebrand proposed a “quadratic” carrier-phonon coupling model for aromatic materials [18,19]. Both hopping limit and band limit transports were also used. Three interactions were considered in the approximation: (a) mechanical coupling between neighboring oscillators with frequency ω_1 , (b) electronic coupling between neighboring molecules with coefficient J , and (c) carrier-phonon quadratic interaction with frequency ω_2 . We may observe the carrier mobility by solving the wave vectors and Hamiltonian equation:

$$\psi[\mathbf{R}, \{x_r\}] = \sum_n a_n \{x_r\} \cdot \phi(\mathbf{R} - na, x_n)$$

$$j\hbar \left(\frac{\partial a_n}{\partial t} \right) = \left\{ \sum_r \left[-\frac{\hbar^2}{2m_R} \left(\frac{\partial^2}{\partial x_r^2} \right) + \frac{1}{2} m_R \omega_0^2 x_r^2 + \frac{1}{4} m_R \omega_1^2 x_r (x_{r+1} + x_{r-1}) \right] - \frac{1}{2} m_R \omega_2^2 x_n^2 \right\} a_n - J(a_{n+1} + a_{n-1})$$

\mathbf{R} and $\{x_r\}$ is the carrier position coordinates and inter-nuclear coordinates, respectively. n is the n^{th} site of the molecular ion. m_R is the reduced mass.



(1) By using the “slow electron” limitation and the condition $\frac{\hbar^2 \omega_2^4}{\omega_0^3} \gg \frac{\hbar^2 \omega_1^2}{\omega_0} \gg 4J$,

we may get the single-oscillator mobility [18]:

$$\mu_{se} = \frac{2\pi q J^2 a^2}{\hbar B k T} \left[\frac{\sigma}{1 + \sigma} \right]$$

(2) By using the “slow phonon” limitation and the condition $\frac{\hbar^2 \omega_2^4}{\omega_0^3} \gg 4J \gg \frac{\hbar^2 \omega_1^2}{\omega_0}$, we

may get the single-oscillator mobility [18]:

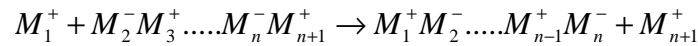
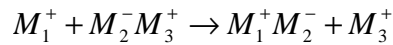
$$\mu_{sp} = \frac{\pi q B^2 a^2}{16 \hbar J k T} \left[\frac{\sigma(1 + \sigma^2)}{(1 + \sigma)(1 + \sigma)^3} \right]$$

where $\sigma = \exp(-\frac{\hbar\omega_0}{kT})$, $B = \frac{\hbar\omega_1^2}{\omega_0}$ B is the phonon band width.

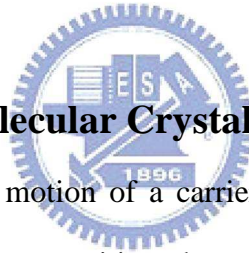
A generally used simple mobility model Mott and Gurney [20] in organic material can also be reduced as:

$$\mu = \frac{qa^2\nu}{kT} \exp(-\frac{\Delta E}{kT})$$

a is the width and ΔE is the height of the potential barrier. ν is the frequency. A different hopping model from ion-exciton complexes is also proposed by Pohl and Gutmann [21, 22] as:



n denotes the sites.



2-1-4 Polarons in the molecular Crystal

In the molecular crystal, the motion of a carrier will be influenced by the other ions.[23, 24] For example, when a positive charged carrier moves in the molecular crystal, it will attract the electron cloud. That will result in the ionic displacement and polarization, which will lower the electrostatic potential in a small region. The decrease of the electrostatic potential can be described as:

$$\frac{1}{4\pi\epsilon_0} \cdot \frac{q^2}{r} \cdot \left(\frac{1}{\epsilon_s} - \frac{1}{\epsilon_\infty} \right)$$

r is the distance between the moving carrier and the electron cloud. ϵ_∞ and ϵ_s represents the high-frequency and low-frequency dielectric constant, respectively. ϵ_0 is the dielectric constant of vacuum. The reduction of electrostatic potential will also become a potential well and bond the moving carrier; as a result, it forms a self-trapped state. That will enlarge the effective carrier mass. The self-trapped states are different from the impurity or the defect created trapping states. The self-trapped

states are not localized and it will move with the motion of the carrier. However, the impurity or the defect related trapping states are localized and fix the carrier at a specific region. The self-trapped states are viewed as motion carriers combined with lattice distortion, which are also viewed as a quasi particle. Based on the polarization range, the polarons can be classified into two arts. One is the large polaron and the other is the small polaron. In order to distinguish the type of polarons, we may define the carrier localization range as l , which is the uncertainty of a carrier. If the $l < r_0$, it will be a small polaron. When $l > r_0$, it will be a large polaron. Where r_0 is equal

to $\sqrt{\frac{\hbar}{2m^* \omega_{LO}}}$. Besides, the polaron magnitude can also be estimated by a

dimensionless factor α , which is given as [25]:

$$\alpha = \frac{q^2}{8\pi\epsilon_0 \hbar \omega_{LO}} \left(\frac{2m^* \omega_{LO}}{\hbar} \right)^{\frac{1}{2}} \left[\frac{1}{\epsilon_\infty} - \frac{1}{\epsilon_s} \right]$$

$\hbar\omega_{LO}$ is the longitudinal optical wave energy. The coupling coefficient α can denote the magnitude of carrier-phonon interaction. The large α represents more phonons interacting with the polarons; these phonons will drag the carriers and lower its motion in the molecular crystals. Besides, the large α will also increase the effective mass of polarons.

Large Polarons

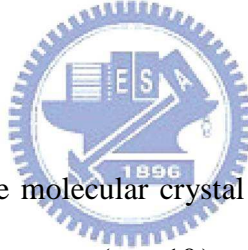
For large polarons, Fröhlich firstly calculated the eigenstates of these large polarons [26], which described the weak and medium-sized electron-phonon coupling. The energy eigenvalues of such polarns for small k value is given by:

$$E_p(k) = E_p(0) + \frac{(\hbar k)^2}{2m_p^*}$$

$$E_p(0) = -\alpha\hbar\omega, m_p^* = m^* \left(1 + \frac{\alpha}{6}\right)$$

$E_p(0)$ is the self trapping energy for large polarons. α is the coupling coefficient.

\hbar is the Plank constant. ω is the angular frequency of the lattice oscillation. m_p^* is the effective mass for polaron. m^* is the effective mass for carrier. If $\alpha < 1$, the self-trapped energy is low and viewed as weak coupling. If $\alpha \cong 5$, we consider it as intermediate coupling. If $\alpha > 10$, the coupling is strong. For actual example, if α is small, the carrier motion will be more free and the m_p^* will be more likely the m^* in the conduction band. Under such condition, the transport of the large polaron is similar to the transport of the electrons or holes. We may use some approximations, such as the corrected band theory, to describe the carrier behavior.



Small Polarons

Most of the polarons inside the molecular crystal are small polarons. The coupling between electron and phonon is strong ($\alpha > 10$) and lifetime of the small polaron is long. The interaction range between carrier and molecular is small, its lattice distortion is at the order of lattice constant, which is only happened around the carriers. The small polaron has smaller energy band-gap and the energy band-gap will be increased with the reducing of the temperature exponentially. Due to the strong carrier-phonon coupling, the small polaron can “tunnel” between the localized polaron states or “hop” between the non-equivalent localized states with phonon creation and annihilation. In generally, the small polaron transport shows two different behaviors under different temperature. Holstein [27] has found that if $T \leq 0.4 \frac{\hbar\omega}{k}$, the band-like transport is assumed for low-temperature small polaron transport. If $T > 0.5 \frac{\hbar\omega}{k}$, the hopping-like is assumed for high-temperature small polaron transport. Its polaron

bandwidth and effective mass will increase with the reduction of temperature. Under the low-temperature condition, the phonon number is low and the carrier-phonon coupling (interaction) is also reduced at the same time. As a result, the small polaron will not be scattered by the phonons significantly and move more likely in the energy band. Under the high-temperature condition, the phonon number is increased and the carrier-phonon coupling (interaction) becomes more strong. The polaron bandwidth will be significantly reduced and the band-like transport is no more valid. The small polarons will hop from one state to the other equivalent states and the motion energy is supported by the phonon. The “hopping process” is also viewed as phonon-assisted tunneling. [28]

It is usually concluded that the carrier motion is between band-like (coherent) and hopping-like transport in room temperature, when the carrier mobility is at the order of 1 cm²/V-sec. Kubo [29,30] proposed a carrier-phonon interaction and Vilfan [31] derived a mobility formula for small polaron model, the mobility equation includes both band-like and hopping-like transport is given as:

$$\mu = \frac{q}{\hbar^2 kT} \left[\frac{\pi}{8(B^2 - B_{ij}^2)} \right]^{1/2} \cdot \exp\left[-\frac{1}{2} \frac{(E_b - E_{ij})^2}{\hbar^2 (B^2 - B_{ij}^2)}\right] \cdot \sum_{i-j} \omega_{ij}^2 r_{ij} r_{ij} \quad (a)$$

$$E_b = \sum \frac{|V_\lambda|^2}{\hbar \omega_\lambda}, E_{ij} = \frac{96W^2}{M \cdot s} I_3'$$

$$B^2 = \frac{48W^2}{Mr^2 \cdot \frac{\hbar s}{r}} \left(\frac{2kT}{\hbar s} \cdot I_3 + I_4 \right), B_{ij}^2 = \frac{48W^2}{Mr^2 \cdot \frac{\hbar s}{r}} \left(\frac{2kT}{\hbar s} \cdot I_3' + I_4' \right)$$

ω_{ij} is the carrier transfer integrals; ω_{ij} is the distance between the center of nearest-neighbor i^{th} and j^{th} molecules; $\hbar \omega_\lambda$ is phonon energy in the λ^{th} states; M is the molecular mass; s is the sound velocity; r is the distance between the nearest-neighbor molecules; V_λ is the coupling constant of carrier and phonon in the

λ^{th} mode. W , I_n , and I_n' are also given as:

$$W = \frac{\alpha}{2} \left(\frac{q}{4\pi\epsilon_0} \right)^2 \frac{1}{r^4}$$

$$I_n = \frac{2\pi}{v} \int_0^{Q_m} Q^{n-3} \left(1 - \frac{\sin(2Q)}{2Q} \right) \cdot dQ$$

$$I_n' = \frac{2\pi}{v} \int_0^{Q_m} Q^{n-3} \left(1 - \frac{\sin(2Q)}{2Q} \right) \frac{\sin Q}{Q} \cdot dQ$$

where α is the mean molecular polarizability; v is the volume of the sphere; Q_m is the dimensionless radius of the Debye sphere; Q is equal to $k_q \cdot r$, where k_q represent the wave vector of phonon. The equation (a) consists the experimental and empirical mobility model, which is represented as :[32]

$$\mu = C \cdot T^{\frac{3}{2}} \exp\left[-\frac{E_a}{kT}\right]$$

E_a is the minimum energy between two equivalent states; T is the absolute temperature. The value of E_a is generally at the order of or smaller than the electron bandwidth of the organic molecular crystals. Besides, the time of formation of small polarons is given as by $\hbar \cdot B$, which is at the order of localized carrier lifetime from the estimation of carrier bandwidth.

2-2. Interface and Dielectric Engineering

2-2-1 Surface Energy and Polarity

The surface energy is defined by the interface tension between two different phases, generally between gas phase and solid phase.[33] It is because of at the interface, the atom value is much less than inside the bulk. The surface force or surface tensile should be re-defined as :[34]

$$\gamma_{gs} = \gamma_{gl} \cos \theta + \gamma_{ls}$$

γ_{gs} is the surface energy of a solid surface. γ_{gl} is the surface tensile of a liquid surface. γ_{ls} is the surface tensile between liquid and solid interface. θ is the contact angle between liquid and solid surface.

2-2-2 Surface Treatment and Organic/Interface Properties

Lowering surface energy of dielectric is a key to high performance OTFTs. However, for most of the conventional dielectrics, such as SiO_2 , SiN_x , or metal oxides, are high surface energy. If we want to lower these inorganic dielectric surface energies, surface treatment is necessary. In 1990s, Philips has proposed the usage of hexamethyldisilazene (HMDS) for surface treatment before organic semiconductor deposition.[35] Consequently, many researchers started the topic of surface treatment by using the self-assembled monolayers (SAMs) to enhance the OTFT performance. The silane based SAM, such as octadecyltrichlorosilane (OTS) and octadecylmethyldimethoxysilane (ODS), are well proposed to improve the OTFT characteristics. The structures of these SAM materials are shown as: [36, 37]

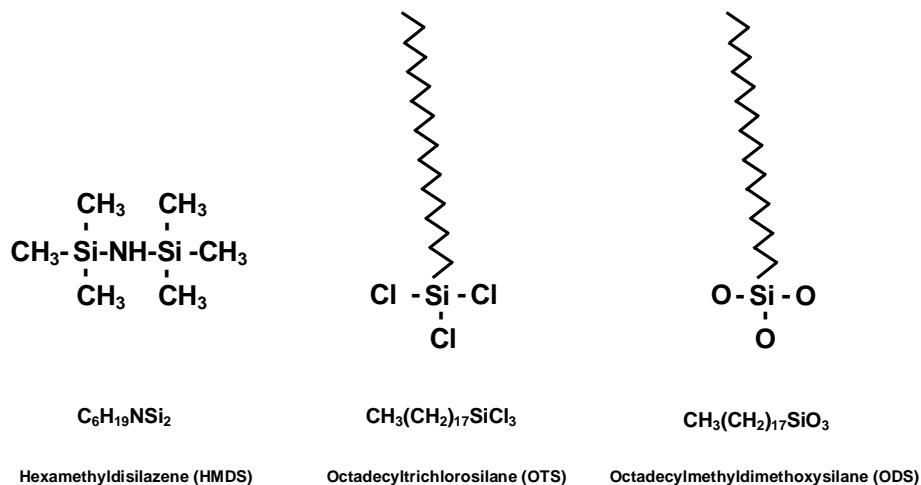


Fig. 2-6 The HMDS, OTS, ODS for surface treatment in OTFTs.

After surface treatment, the dielectric surface will turn into hydrophobic. The water contact angle can be as large as 100 degree or more. The surface energy can be lower

to less than $40\text{mJ}/\text{cm}^2$ at the same time. For most of reports, with the surface treatment on OTFT dielectrics, the OTFT mobility shows drastically increased. The high mobility about $2.1\text{-}3.3\text{cm}^2/\text{V}\cdot\text{sec}$ was reported with SAM treatment or even SAM with longer alkyl chains.[38] Many researchers have summarized that the possible reason for the SAM treatment on mobility improvement: (1) The SAM may increased the grain size, (2) The SAM may increase the number of flat-lying molecules, (3) The SAM will lead to high continuously grown molecules in the first few layers, (4) The SAM will reduce the surface roughness, (5) The terminal groups on SAM may produce high order film, (6) The SAM may form the interchain cross-linking, that will create a uniform surface, and (7) The SAM may neutralize the surface defects.[39]

As for controlling the surface energy of dielectrics, there is still a alternative method. We may use the low surface energy materials to act as the OTFT dielectrics. Due to the simple process, accessibility, and low cost, the polymers are the candidates for OTFT dielectrics. The commonly used for OTFT dielectrics are shown as follows :[39]

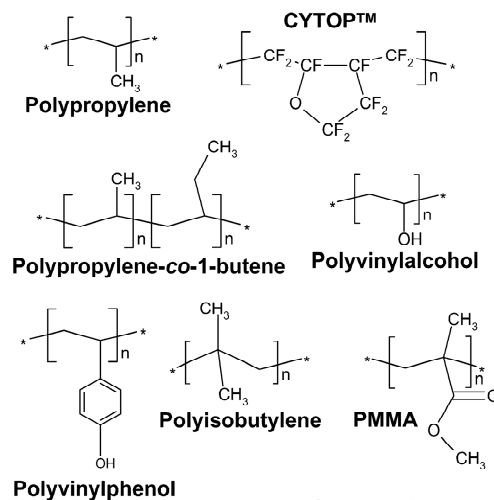


Fig. 2-7 The polymer dielectric for OTFTs.

(Janos Veres *et. al.*, AVECIA, Electronic Materials and Philips Research Laboratories)

In contrary to the conventional dielectrics, these materials are low dielectric permittivity and low polar. Most polymers are carbon or hydrogen compounds with special end groups, such as $-OH$, $-R$, $-CH_3$, or $-RO$ bonds. These dielectric constants are at the range between 2.1 to 4.5. With the use of polymer dielectrics, the high mobility about $1.5\text{-}3\text{cm}^2/\text{v}\text{-sec}$ may be observed in OTFTs with PVP or PMMA dielectrics. The reason of high mobility with the usage of polymer dielectrics is its low surface energy, which may match to the organic semiconductor. As a result, the voids or defect at the interface or inside bulks will be reduced. Besides, the low dielectric permittivity material is also low polar material. It is because of the high polar material will enhance the localization at the OTFT channel region and will result in randomly orientated interface dipoles. Potentially, the bulk density of states will be broadened and scattering probability will also be increased at the same time. Hence, with the usage of polymer dielectrics, that will provide a longer screening distance from polar sites and defects. The polar induced localization and bulk DOS extension may be illustrated as :[39]

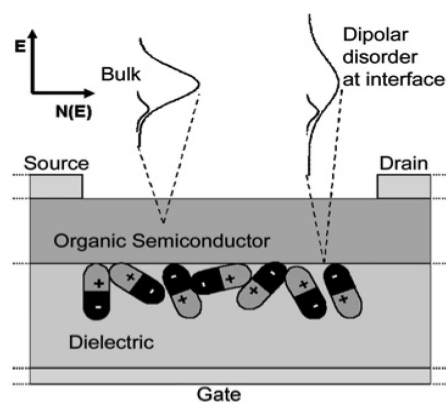


Fig. 2-8 The effects of polar dielectric result in local disorder and DOS extension.

(Janos Veres *et. al.*, AVECIA, *Electronic Materials and Philips Research Laboratories*)

2-3. Optoelectronic Interaction in Organic Semiconductors

2-3-1 Transition and Exciton Process

The optoelectronic process in organic semiconductor is usually explained by quantum theory with energy band-structure. The process involves the energy and momentum conservation between electron and photon exchanging. Electrons will be excited from occupied energy level to unoccupied higher energy level. As a result; the electrons excited to excited states will form excitons. In the view of molecular orbitals, the molecular orbit number is equal to π -electron number. The typical energy states: ground states, singlet states, and triplet states in organic orbitals can be illustrated as :[40]

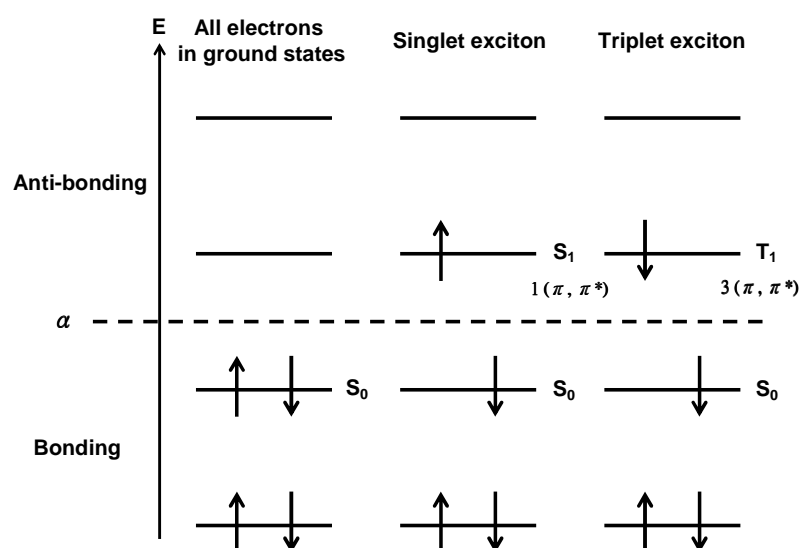


Fig. 2-9 The energy level of singlet and triplet states.

In the ground state, all the electrons are occupied under a specific energy and the total spin is zero. The multiplicity is equal to $2S + 1 = 1$ and shows a diamagnetic property. When an electron is excited to singlet state and forms an exciton, the total spin is still zero. The multiplicity is equal to $2S + 1 = 1$ and also shows a diamagnetic property. When the electron is excited to triplet state and forms an exciton, the total spin becomes 1, its multiplicity is equal to $2S + 1 = 3$ and shows a paramagnetic property.

In semiconductor, the generation of exciton usually contains the photon absorption and electron excitation.[41] When the phonon energy is larger than the material energy band-gap, the electron may be excited from the ground state into the excited states. The hole will also be created at the same time. However, when the incident phonon energy is equal to the energy band-gap, the electron and hole can not be separated. The electron and hole will be bounded together and move together. This bounded electron-hole pair will be viewed as an exciton and it acts as a quasi particle. But it will not influence the conductivity of molecule crystal. When the distance between the electron and hole ($r_{exciton}$) in an exciton is at the order of lattice constant, the Coulomb force is strong between electron and hole. This type of exciton is called “Frenkel exciton” or “Tightly bonded exciton”. When the $r_{exciton}$ is at the order of hundred lattice constant, the Coulomb force is weak between electron and hole, which is also acts as a hydrogen-like particle. This exciton is called “Mott-Wannier exciton” or “Loosely bonded exciton”. There is still another type of exciton, its $r_{exciton}$ is at the order between “Frenkel exciton” and “Mott-Wannier exciton”. Its electron and hole is existed on different molecule, respectively. The exciton energy is also less than the ionization energy of the crystal molecules and is created in the process of electron-hole pair recombination. The third exciton is called “Charge transfer exciton”, it is neutral and moves in the crystal. The three types of excitons can also be illustrated and explained as: [42]

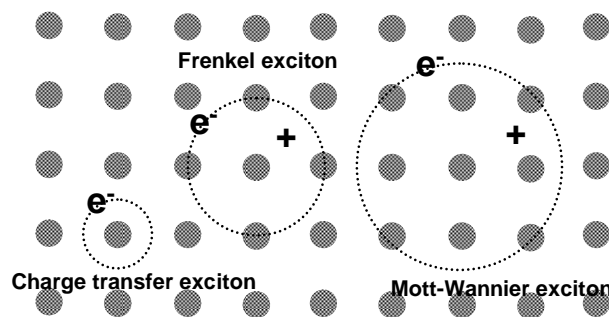
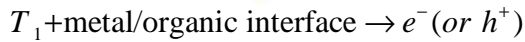
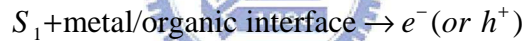


Fig. 2-10 Three types of excitons inside the crystalline materials.

Actually, in the organic crystals, the photo-generated charges are mainly from the dissociated excitons. When the photons are absorbed by organic crystal, the Frenkel excitons will be generated. These excitons will move or collide with crystal interface, impurities, and defects. As a result, the excitons will be dissociated into electrons and holes with a very high efficiency for non-radiative annihilation. The exciton dissociation process will be discussed as follows.

(I) Exciton dissociation at semiconductor/electrode interface

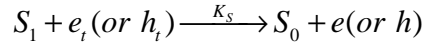
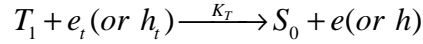
Researchers had reported the dissociation of excitons at the metal-organic interface. [43, 44] The process involves an exciton ejecting its electron to metal by a tunneling process and results in a oxidative dissociation. At the same time, an exciton dissociates with an electron injection from the metal and results in a reductive dissociation. The process can be described as:



S_1 and T_1 denotes the singlet exciton and triplet exciton, respectively. M^* is the molecule in the excited state.

(II) Exciton dissociation involves trapped carriers

When the trapped carrier is associated with the exciton dissociation, [45] the exciton will transfer its energy to the trapped carrier. This process is a detrapping process and its efficiency is a function of trap distribution, photon energy, and photon flux. The process is also described as:



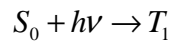
Where e_t and h_t is the trapped electron and holes, respectively. K_T and K_S is the rate constant for triplet and singlet state, respectively. In general, the interaction between triplet excitons and trapped carriers has higher efficiency. We may also estimate the carrier density with the exciton dissociation by the rate equation:

$$\frac{dp}{dt} = \eta_T \cdot K_T \cdot [T] \cdot p_t + \eta'_T \cdot \epsilon_{0p} i_T \cdot p_t - \frac{p}{\tau_T}$$

p is the free hole concentration. p_t is the trapped hole concentration. η_T and η'_T is the efficiency of exciton dissociation and optical detrapping, respectively. T is the triplet exciton concentration. ϵ_{0p} is the absorption coefficient of optical detrapping. i is the light intensity. Thus, we can observe the steady state free hole concentration as:

$$p = \tau_T \cdot i_T \cdot p_t [\eta_T \cdot K_T \cdot \epsilon_T (\beta_1 + \beta_2)^{-1} + \eta'_T \cdot \epsilon_{0p}]$$

β_i is also the rate constant. In short, the indirect interaction of triplet-exciton and trapped carriers can also be explained by the following



The excess carriers from the dissociation of excitons will result in the changes of conductivity in the organic semiconductors. The changes of conductivity require rise time and decay time, which is determined by the free carrier lifetime. The carrier lifetime is a caused by the trapping or de-trapping process, it can also be observed by the approximation by Rose :[\[46\]](#)

$$\tau_m = \tau_n \left(1 + \frac{n_t}{n}\right)$$

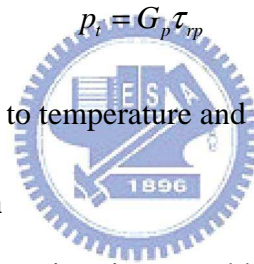
$$\tau_{rp} = \tau_p \left(1 + \frac{p_t}{p}\right)$$

Where τ_n and τ_p is the electron and hole lifetime, respectively. n_t and p_t is the electron and hole lifetime, respectively.

for an approximated example, if $p_t \gg p$, the hole will influence the organic conductance seriously after illumination, where leads to:

$$\tau_{rp} = \tau_p \left(\frac{p_t}{p}\right)$$

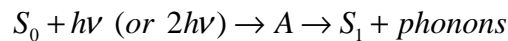
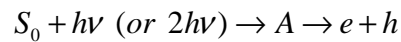
If we consider the conductance changes after photo-illumination, the free hole density is $\Delta p = G_p \tau_p$, we may estimate the trapped carrier density as:



Both p_t and τ_{rp} are sensitive to temperature and light intensity

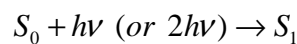
(III) Exciton auto-ionization

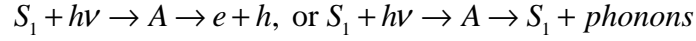
The process describes when the exciton is created by two or more photon absorption. After the formation of exciton, it will be dissociated into carriers or to the lower non-ionized states spontaneously. This process is called exciton “auto-ionization” and may describe by Bergman *et al.* :[47]



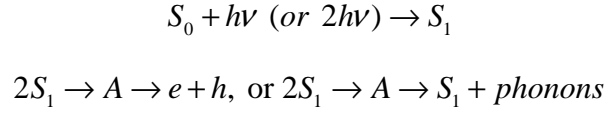
Where A is a metastable state.

Besides, the excited states below conduction band may be excited as a metastable state. For a singlet exciton photo-ionization, the “exciton photo-ionization” process is described as:





Finally, if the two relaxed singlet excitons collide, a possible “exciton collision ionization” will process as:



The mentioned process may also involve internal conversion process.

2-3-2 Extrinsic and Intrinsic Photoconduction

The photoconductive process can be classified into two groups. One is the “extrinsic photoconduction”, which contains (1) Carrier trapping and recombination, and (2) Exciton process. The extrinsic photoconduction is usually involves one type carriers mainly. The process involves carrier trapping and recombination. The carrier generation time and relaxation time will be a function of defect density, temperature, and light intensity. If we consider a quasi-static system with carrier injection and photo illumination, the modified photo-current equation may be described as:[48]

$$J = \frac{9}{8} \frac{\epsilon \mu_p N_v^{1/l}}{H_b} \left(\frac{\sigma_{op} \cdot i}{v \sigma_p} \right)^{(l-1)/l} \cdot \frac{V^2}{d^3}$$

Which is modified from the space-charge limits equation,[49] the equation describes trap associated carrier transport inside bulks. μ_p is the hole mobility, N_v is the effective density of state in valence band, H_b is the trap distribution function within forbidden energy gap, σ is the capture coefficient, and l is T_c/T .

If we consider a material illuminated with light without carrier injection, we rewrite the photo-current equation as:[50]

$$J = q \left(\frac{9}{8} \frac{\epsilon \mu_p \theta}{q} \right)^{\frac{1}{4}} \cdot (G_p)^{\frac{3}{4}} \cdot V^{\frac{1}{2}}$$

Where G_p is the hole generation rate and θ is the ratio of free carrier density.

These trap and light-intensity related photo-conductance equations all show the photocurrent J_{ph} versus light intensity i with a relation of $J_{ph} \propto i^w$, where i is the light intensity and w is the factor that determine the recombination channel.

Besides, the exciton dissociation is also one of the intrinsic photoconduction. If the dissociation is located at the interface of metal and organic material, there will be an oxidative or reductive dissociation. The exciton dissociation also involves with the trapped carriers and phonon or multi-photon process.

On the other hand, the “intrinsic photoconduction” has several origins in organic materials. For example, under a condition of high exciton density, the photo-ionization will through the multi-photon process or exciton collision and result in photoconduction. Additionally, when the incident photon energy is larger than the organic band-gaps and that will create electron-hole pairs and become a band-to-band transition. However, the direct band-to-band transition is much less in organic materials than in inorganic materials. The other example of intrinsic photoconduction is auto-ionization. This process describes the spontaneous exciton dissociation with multiple photon-assisted processes.

2-3-3 Defect, Disordered System and Localization

In crystal or poly-crystalline materials, the defect is easily to involve the photo or electrical process. The un-perfect sites inside the material usually create defect states, which are attractive or repulsive to carriers, such as electron, hole, and exciton. These defect states can be illustrated as a diagram: [\[51\]](#)

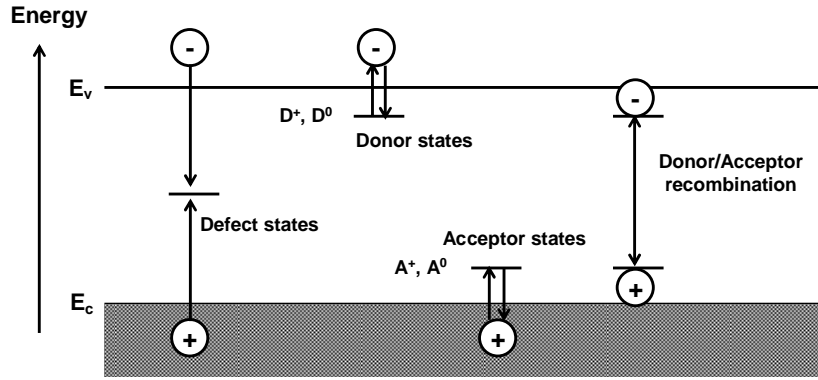


Fig. 2-11 The defect related optical transitions.

The defect states inside the energy band-gap will be neutral or charged. The carrier will also be captured, recombined, or be emitted from these states. The formation of these localized defect states can be considered from band theory. From a simplified and perfect periodical potential well, as show in follows [51-54]:

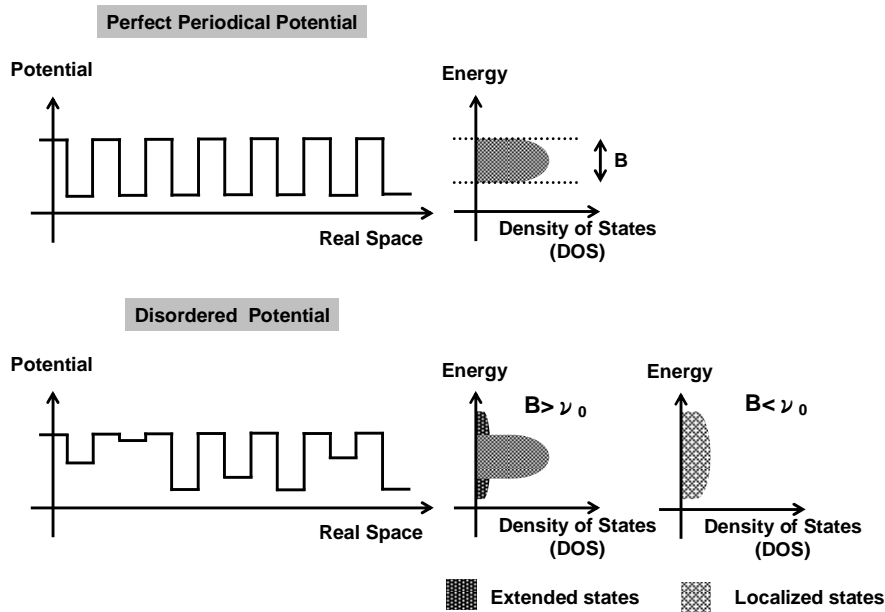


Fig. 2-12 The influence of local energy (potential) fluctuation on DOS.

In the case of perfect periodical potential with band width “B”, we may obtain a given distribution of density of state (DOS). When a potential perturbation ν_0 is introduced into the perfect potential, it becomes a disorder system. If the potential perturbation is small ($\nu_0 < B$), there will be some additional states that extended from

the original DOS. Both localized states (at band tail) and extended states exist. If the potential perturbation is large ($v_0 > B$), the original DOS will be broaden and only localized states exists in the band. We may further explain the states by using the Bloch wave functions as:

$$\phi_{\mathbf{k}}^{Bloch}(\mathbf{r}) = \sum_i e^{i\mathbf{k}\cdot\mathbf{R}_i} \cdot \phi_n(\mathbf{r} - \mathbf{R}_i) = e^{i\mathbf{k}\cdot\mathbf{r}} \sum_i e^{i\mathbf{k}\cdot(\mathbf{r}-\mathbf{R}_i)} \cdot \phi_n(\mathbf{r} - \mathbf{R}_i) = e^{i\mathbf{k}\cdot\mathbf{r}} \cdot u_{\mathbf{k}}(\mathbf{r})$$

This function is a superposition of atomic orbits ϕ_n at every lattice site \mathbf{R}_i with long-range phase correlation. When the extended states exist in a disordered system, we may lose the information long-range phase correlation. The Bloch wave function terms into an extended form:

$$\phi^{ext}(\mathbf{r}) = \sum_i c_i \cdot \phi_n(\mathbf{r} - \mathbf{R}_i)$$

On the other hand, if a localized state forms up, we should introduce an exponential decay term with a localization length δ :

$$\phi^{loc}(\mathbf{r}) = \sum_i d_i \cdot \phi_n(\mathbf{r} - \mathbf{R}_i) \cdot e^{-|\mathbf{r}-\mathbf{R}_i|/\delta}$$

We may also explain these localized or extended tail states by a diagram:[55]

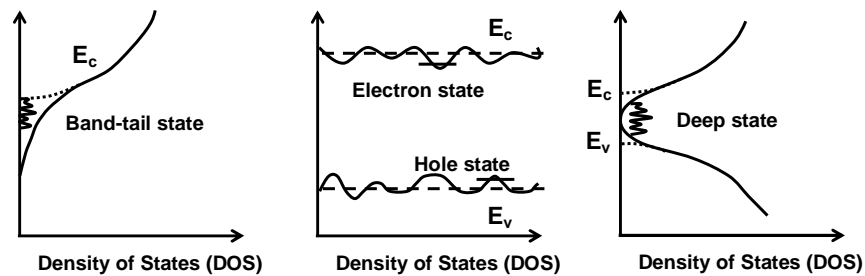


Fig. 2-13 The DOS of localized states and its energy distribution.

As for small disorder inside the bulk, the insufficiency of long-range phase will extend the states from conduction band or valence band and change the carrier concentration (doping density) in the material. The local potential fluctuation will create the electron or hole states near the conduction band or valence band. For large

disorder, it will lead to exponentially decayed tail states from both conduction band and valence band, which will cover over the whole energy band-gap. Furthermore, the un-bonded atomics will result in the dangling bond and form the deep states inside the energy band-gap.

2-4 Operation of Organic Devices and Parameter Definition

Actually, the general operation concepts are originated from MOSFET theory. When a bias (V_G) is applied to the gate electrode, the voltage-drop over the insulator and the semiconductor accumulates charges near the insulator/semiconductor interfaces. The typical I-V characteristics can be used to calculate the important parameters such as mobility, threshold voltage, and on/off current ratio.

Since the pentacene is a p-type semiconductor. Thus, negative bias is applied to the gate, the voltage-drop between insulator and semiconductor cause the band bending in the organic semiconductor. The additional positive charges will accumulate between the interfaces. The insulator serves as a capacitance per unit area which stores charges and can be represented as C_{ox} , then the accumulated charge per unit area is about $V_G C_i$. Additionally, assuming that a negligibly small voltage, V_{th} , is dropped across the semiconductor. In this situation, the applied drain bias can drive the current from source to drain. The conduction is determined by the mobility (μ) which represents the driving ability of the electrical field on the accumulated charges. Therefore, the increased gate voltage δV_G accounts for the increased charges $C_{ox} \delta V_G$ and the total charges accumulated over the channel region are $WLC_{ox} \delta V_G$, where W and L corresponds to the channel width and length, respectively. If the increment of charge has a mobility of μ , and a small drain bias: V_D is applied then an incremental current δI_D is represented as:

$$\delta I_D \approx \frac{W}{L} \mu C_{OX} V_D \delta V_G$$

In general, we can divide the operation of OTFTs into two regions, linear and saturation regions. The drain current in the linear region is determined from the following equation:[56]

$$I_D = \frac{W}{L} C_{OX} \mu (V_G - V_{TH} - \frac{V_D}{2}) V_D$$

Since the drain voltage is quite small, sometimes equation can be simplified as:

$$I_D = \frac{W}{L} C_{OX} \mu (V_G - V_{TH}) V_D$$

For $-V_D > -(V_G - V_{TH})$, I_D tends to saturate due to the pinch-off of the accumulation layer. The current equation is modified as:

$$I_D = \frac{W}{2L} C_{OX} \mu (V_G - V_{TH})^2$$



Parameter Extraction

In this section, the methods of extraction the mobility, the threshold voltage, the on/off current ratio, the subthreshold swing, the maximum interface trap density, and the surface free energy is characterized, respectively.[57]

(1) Mobility

Generally, mobility can be extracted from the transconductance maximum g_m in the linear region:

$$g_m = \left[\frac{\partial I_D}{\partial V_G} \right]_{V_D = \text{constant}} = \frac{WC_{OX}}{L} \mu V_D$$

Mobility can also be extracted from the slope of the curve of the square-root of drain current versus the gate voltage in the saturation region, i.e. $-V_D > -(V_G - V_{TH})$:

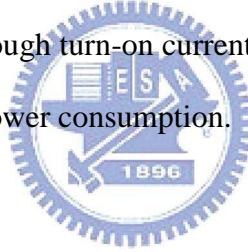
$$\sqrt{I_D} = \sqrt{\frac{W}{2L} \mu C_{OX}} (V_G - V_{TH})$$

(2) Threshold voltage

Threshold voltage is related to the operation voltage and the power consumptions of an OTFT. We extract the threshold voltage from equation (2.6), the intersection point of the square-root of drain current versus gate voltage when the device is in the saturation mode operation.

(3) On/Off current ratio

Devices with high on/off current ratio represent large turn-on current and small off current. It determines the gray-level switching of the displays. High on/off current ratio means there are enough turn-on current to drive the pixel and sufficiently low off current to keep in low power consumption.



(4) Subthreshold swing

Subthreshold swing is also important characteristics for device application. Its is a measure of how rapidly the device switches from the off state to the on state in the region of exponential current increase. Moverover, the subthreshold swing also represents the interface quality and the defect density.

$$S = \left. \frac{\partial V_G}{\partial (\log I_D)} \right|_{V_D = \text{constant}}, \text{ when } V_G < V_T \text{ for p-type.}$$

If we want to have good performance TFTs, we need to lower subthreshold swing of transistors.

(5) Maximum interface trap density

The maximum number of interface traps density, at the pentacene/dielectric interface can be estimated from the value of the subthreshold swing. Assuming that the densities of deep bulk states and interface states are independent of energy: [58]

$$N_{ss} = \left[\frac{S \cdot \log(e)}{kT/q} - 1 \right] \cdot \frac{C_i}{q}$$

where S is the subthreshold swing, C_i is the capacitance density, k is Boltzmann's constant, and T is the absolute temperature.



Chapter 3.

Experiment Details

The low temperature AlN films were deposited by a radio frequency inductively coupled plasma (RF-ICP) system. In this system, a 2-inch Al target (purity 99.999%) of the RF gun was immersed in a 4-inch inductive coil which can be controlled by an independent RF coil power. Before the AlN films deposition, the n⁺-Si wafer used as the substrate was rinsed in the deionization water, followed by the initial RCA cleaning. Right before we transferred the wafer into the RF-ICP system, we used acetone with ultrasonic to remove the particles and the impurities and dipped the wafer in the dilute HF solution (HF:H₂O=1:100) to remove the native oxide on the Si wafer. The system was pumped down to a base pressure less than 2×10^{-6} torr before admitting gas in. A mixed gas of argon and nitrogen was monitored by mass flow controllers at different Ar:N₂ ratio. AlN films were deposited at a total pressure of 2.5mtorr and at a substrate temperature varied from room temperature to 250°C. The RF gun and the inductively coupled coil power can be varied from 0 to 200W and 0 to 180W, respectively. All the relative experiment details were published in our previous reports. The thickness of AlN was estimated by the cross-section image of the scanning electron microscopy (SEM).

The devices used in this series of experiments are the top contact (TC) structure, which means the organic semiconductor layer is deposited on the bottom of the contact electrodes. The detail fabrication processes are following:

Step1. Substrate and gate electrode

4-inch n-type heavily-doped single crystal silicon wafer with (100) orientation is used as substrate and gate electrode.

Step2. Gate dielectric formation

After the initial acetone cleaning and dilute HF solution, the gate dielectric layer is formed in RF-ICP sputter system. High quality AlN film can be formed under low temperature.

Step3. Pentacene film deposition through the shadow mask

The pentacene material obtained from Aldrich without any purification was directly placed in the thermal coater for the deposition. It is well known that the deposition pressure, deposition rate, and deposition temperature are the three critical parameters to the quality of the organic film. The deposition is started at the pressure around 1×10^{-6} torr. The deposition rate is controlled at $\sim 0.5 \text{ \AA}/\text{sec}$ and the thickness of pentacene film was about 100nm, monitored by the quartz crystal oscillator. Slower deposition rate is expected to result in smoother and better ordering of the organic molecules. The deposition temperature is also a factor influencing the pentacene film formation. The temperature we use in depositing pentacene films is 70°C . We use shadow mask to define the active region of each device.

Step4. Source/Drain deposition through the shadow mask

The injection barrier of the OTFT device is determined by the materials of the source and drain electrodes. Materials with large work function are preferred to form Ohmic contact. The Au with work function $\sim 5.1\text{eV}$ does help to provide a better injection. Then, we deposited Au as the source/drain electrodes on the pentacene film. The thickness of the electrode pad is 1000 \AA .

In this study, all the measured data were obtained from the semiconductor parameter analyzer (HP 4156A) in the darks at room temperature. And we measure the OTFTs immediately when the samples were unloaded from the evaporation

chamber. The structures of metal-insulator-silicon (MIS)-Au/AlN/Si capacitors were fabricated using the following procedure. First, heavily doped n-type silicon (100) substrates were degreased and acid cleaned using an initial RCA cleaning and an HF solution dip. The AlN films were deposited by RF-ICP system. A mixture gas of argon and nitrogen at different Ar:N₂ ratio and the substrates were heated during deposition at different temperature. The top electrodes (Au) were defined by shadow mask. The area of the Au pad is 500×500μm². The Au thickness is about 700Å. In the MIS capacitors, AlN films were deposited on blank silicon wafers, and subsequently covered with Au. The MIS was electrically characterized in terms of leakage current and dielectric constant. Current-voltage (I-V) measurements were done with an HP 4156A parameter analyzer. Capacitance-voltage (C-V) curves were obtained by an HP 4284A C-V meter. The frequency dependence of the capacitances was measured at frequencies from 50Hz to 960KHz.

A glass substrate was rinsed in the (KG detergent) and de-ionized water in an ultrasonic system before the device fabrication. Consequently, a 10Å Ni layer and a 200Å Pd layer were deposited as gate electrodes. PMMA [poly(methyl methacrylate)] we used was obtained from MicroChem Corp (with a molecular weight of 95000), which was dissolved in anisole at 95 wt %. The PMMA was then spun onto the gate electrodes at a speed about 4000 to 5000rpm. After spin-on coating, the PMMA was transferred to a hot-plate and annealed at 90°C for 30minutes. The thickness of PMMA was estimated by the cross-section image of the scanning electron microscopy (SEM) and capacitance measurement, respectively. After the dielectric fabrication, a portion of PMMA dielectrics were chosen to expose to the UV-light in ambient atmosphere about 60-90sec. The UV-light we used was with an output power 40mW and a wavelength around 175-285nm. To study the effects of

light-illumination on PMMA-OTFTs, we setup a probing stage with a light-source. The light-source we used in the experiment is a 150W halogen lamp, which is filtered at 460nm by a band-pass filter with a full width half maximum (FWHM) about 10nm. The filtered-light is guided by an optical fiber and focused by a microscope. The total light power and the spot diameter on the probing stage was about 1.5-2.7 μ W and 2.5mm, respectively.

In this study, the OTFT devices we used are top-contact structures. A p-type, single crystal silicon wafer (100) was used as the substrate and the gate electrode. After RCA cleaning, a 1000 \AA thermally-grown SiO₂ layer was deposited by furnace. After the SiO₂ deposition, we try to remove the SiO₂ layer from the wafer of unpolished-side. The etching-solution we used is buffered oxide etching (B.O.E.) solution (40% NH₄F and 1 part 49% HF). Hence, the wafer of unpolished-side without SiO₂ layer can serve as a gate-electrode. Finally, the substrate was cleaned in ultrasonic tank by the sequence of: de-ionic water (5 minutes), acetone (1 minutes), and de-ionic water (5 minutes). After substrate cleaning, we spin the solution-based Polymethylmethacrylate (PMMA) onto the substrate. The content of solution-based PMMA is a mix of PMMA and anisole with a concentration of 95wt%. Consequently, we try to remove the residual solvent. The substrate is then baked on hot-plate at 90 $^{\circ}$ C about 30 minutes. As shown in Fig. 3.1, the gas-sensing system consists of three major parts: a gaseous analyte controller, a gas-proof chamber, and a semiconductor parameter analyzer. The gaseous analyte was introduced into the gas-proof chamber via the mass flow controllers (MFC; 5850E, Brooks Instrument). The pressure inside the gas-proof chamber is monitored by vacuum gauge (PC-615). The total volume of the gas-proof chamber is about 40 liter. The system is equipped with five Kelvin-probes and positioners. The probes were connected to the semiconductor

analyzer (Keithley 4200-SCS) via tri-axial cables. The bottom pipe and the upper pipe serve as the gas-inlet and gas-exhaust, respectively. After mounting a metal cap with transparent window, the gas-proof chamber can be pumped down to less than 1 torr. Consequently, we introduce the pure nitrogen gas into the gas-proof chamber. Thus, all the gaseous-sensing experiments can be processed in a low-humidity and low-oxygen ambience. All the experiments were also be operated at a pressure about 760 torr.



Chapter 4

High Performance Aluminum Nitride Organic Thin-Film Transistors

4-1 Introduction

Organic thin film transistors (OTFTs) had attracted lots of interest for the applications such as organic electronics or flexible displays.[1-3] To improve the OTFTs performance, gate dielectric films with smooth morphology, low leakage current, and high relative electrical permittivity are needed. In recently progress, the spin-on polymer dielectrics have been intensively studied.[4-6] However, pinholes may arise when the polymer thickness is reduced. This results in the rough surface as well as the leakage current of the dielectric film. On the other hand, several high-k materials were also proposed to increase capacitance and lower down the OTFT operation voltage.[7-10] For these ceramic-based high-k dielectrics, high leakage current is also a critical issue to overcome.[11-13] As well as the increase in capacitance, the surface polarity (hydrophilic or hydrophobic) of the gate-dielectric is an important factor. Many researchers have shown that the surface polarity of polymer dielectric is suitable for organic film deposition, because they have similar surface energies to those of organic films. The dielectric polarity is usually altered by the self-assembled monolayer (SAM) on inorganic dielectrics. Inorganic dielectrics with lower surface energy should improve device performance; such surfaces reduce the number of interface traps in OTFTs.[14,15]

Among the group III-Nitrides, AlN has been proposed as a kind of high-k material for gate-dielectric in transistors. The AlN film has high chemical stability, high physical stability, and high dielectric permittivity.[16] With the progress of deposition technology, the AlN-capacitance is successfully fabricated and well investigated.

[17,18] For high-k materials, it is known that the control of gate leakage is a major concern. To enhance dielectric strength, several methods such as exchanging the sputtering target, doping or annealing the dielectric have been proposed. [19,20] It is also suggested that repair the defects in dielectrics might suppress the leakage. As for the AlN film, the defects in the forbidden-gap are broadly investigated. [21-23] It is suggested that the defects near the conduction band edge might be a leakage path. The carriers through the traps and reemission would result in a Poole-Frenkel transport. In other metal-oxide dielectrics, the oxygen vacancies were the principal defects that degrade the dielectric. [24] Some researchers introduced the oxygen flow to restore the defects by compensating the oxygen component. The dielectric leakage was significantly suppressed based on their results. [25] Thus, by compensating the none-metallic element in the compound-dielectric should be a practicable way to suppress the leakage. In this study, we will show that the RF-sputtered AlN can be used as the low-temperature dielectric for pentacene-based organic thin film transistors (OTFTs). We fabricated the OTFTs using AlN film as a new gate dielectric. Low temperature sputtered AlN film, which sputtered at different deposition temperature (250°C, 200°C, and 150°C), were compared. We investigated these AlN film surface roughness and dielectric leakage properties by measuring the AFM images and capacitance leakage. We also tried to reduce the AlN gate-leakage by altering the reactive gas (Ar/N₂) ratio during the sputtering process. Thus, the thin (<100nm) and low-leakage AlN gate dielectric was achieved. The AlN film was hydrophobic and the surface energy was similar to that of the pentacene film. The demonstrated AlN-OTFTs can be operated at low voltage (<5V). High field effect mobility (>1.6cm²/v-sec), low threshold voltage (-2V), and extremely low sub-threshold swing (~130mV/dec) were also obtained.

4-2. Experimental

The low temperature AlN films were deposited by a radio frequency inductively coupled plasma (RF-ICP) system.[26] In this system, a 2-inch Al target (purity 99.999%) of the RF gun was immersed in a 4-inch inductive coil which can be controlled by an independent RF coil power. Before the AlN deposition, the n⁺-Si wafer used as the substrate was rinsed in the deionization water, followed by the acetone with ultrasonic to remove the particles and the impurities. Right before we transferred the wafer into the RF-ICP system, we dipped the wafer in the dilute HF solution (HF:H₂O=1:100) to remove the native oxide on the Si wafer. The system was pumped down to a base pressure less than 2×10⁻⁶torr before admitting gas in. A mixed gas of argon and nitrogen was monitored by mass flow controllers at a Ar:N₂ ratio of 2:9. AlN films were deposited at a total pressure of 2.5 mtorr and at a substrate temperature varied from 150 °C to 250 °C . The RF gun and the inductively coupled coil power can be varied from 0 to 200W and 0 to 180W, respectively. A mixed gas of argon and nitrogen was also monitored by mass flow controllers (MFC) at different Ar/N₂ ratios: 2/5, 2/7, and 2/9, respectively. The AlN films (thickness ~100nm or less) were deposited at a total pressure of 2.5m torr and a substrate temperature at 150 °C . All the relative experiment details were published in the previous reports. The thickness of AlN was estimated by the cross-section image of the scanning electron microscopy (SEM). After the AlN film being deposited, we deposited the pentacene film through the shadow mask. The pentacene material obtained from Aldrich without any purification was directly placed in the thermal coater for the deposition. The substrate was heated to 70 °C during the deposition at the pressure around 1×10⁻⁶ torr. The thickness of pentacene film was about 100nm and the deposition rate was ~0.5Å/sec, monitored by the quartz crystal oscillator.

Then, we deposited Au as the source/drain electrodes on the pentacene film. The thickness of the electrode pad is 1000Å, and the channel width and length were defined as 600µm and 100µm. Metal-insulator-semiconductor (MIS) –Au/AlN/Si was also fabricated to analyze the gate leakage and the dielectric properties. The area of the Au pad was 500×500µm². All electrical properties were measured by Agilent 4156 and Agilent 4284 analyzers.

4-3. Effects of Deposition Temperature on AlN Gate Insulator

Firstly, we discuss the electrical properties of the MIS capacitance structure. The leakage current measured from the MIS structure with 95-nm-thick AlN is shown in Fig. 4-3-1. AlN films deposited at different temperatures are compared. For AlN deposited at 150°C, low leakage current about 1×10⁻⁹ A/cm² can be obtained at electric field as 1 MV/cm and the breakdown field is more than 5 MV/cm. These dielectric properties are comparable to those of the thermal SiO₂, high-k, or polymer gate dielectrics in some reports.[4,8,10-12] The 200°C -AlN and 250°C -AlN dielectric exhibited larger leakage (2.4×10⁻⁹ A/cm² for 200°C and 6.2×10⁻⁹ A/cm² for 250°C at 1MV/cm), yet these value are acceptable for device fabrication. The capacitance-frequency characteristic is also shown in the inset of Fig. 1. Under a wide frequency operation range, from 50 Hz to 1 kHz, the capacitance and the calculated dielectric permittivity are around ~64 nf/cm² and ~7, respectively.

The transfer characteristics of devices with AlN dielectrics grown at different temperatures are shown in Fig. 4-3-2(a). The drain voltage is biased as -3V to keep the devices operated under linear region and the gate voltage is scanned from +2V to -10V. When the AlN deposition temperature is varied from 250°C, 200°C, to 150°C, the device subthreshold swing is improved from 0.6V/decade to 0.4V/decade and the device output current is enlarged more than one order. Since the subthreshold swing

represents the interface quality and the defect density, we calculate the maximum interface trap density by the approximation [15,27,28]:

$$N_{ss} = \left[\frac{S \cdot \log(e)}{kT/q} - 1 \right] \cdot \frac{C_i}{q},$$

where S is the subthreshold swing, C_i is the capacitance density, k is Boltzmann's constant, and T is the absolute temperature. By assuming $C_i = 64 \text{ nf/cm}^2$ and $S = 0.4 \text{ V/decade}$, the approximate interface trap density in our devices is $2.28 \times 10^{12} \text{ cm}^{-2} \text{ eV}^{-1}$. This result is comparable to other dielectrics in OTFTs.[4,16, 29-31]

Additionally, lowering the AlN temperature also reduces the device threshold voltage.

The inset of Fig. 4-3-2(a) depicts the curves of $\sqrt{I_D}$ v.s. V_G , the x-axis interval reveals that OTFTs with 250 °C AlN film have higher threshold voltage as -6 V while those with 200 °C and 150 °C AlN films have lower threshold voltage as -2 V. The

output characteristics of the proposed OTFT with 150 °C AlN-dielectric (AlN-OTFTs) was also shown in Fig. 4-3-2(b). The improvement of the device performance by

reducing the AlN deposition temperature can be further studied by comparing their field effect mobility in Fig. 4-3-3. The mobility is extracted from the linear region

transconductance as :

$$\mu = \frac{L}{V_D W C_i} \left. \frac{\partial I_D}{\partial V_G} \right|_{V_D = \text{const}}$$

When we compare the mobility of devices with 150 °C AlN film, 200 °C AlN film, and 250 °C AlN film, obviously the former two have larger maximum mobility such as $0.24 \text{ cm}^2/\text{V-sec}$ for 150 °C AlN-OTFTs and $0.04 \text{ cm}^2/\text{V-sec}$ for 200 °C AlN-OTFTs. Those devices with AlN deposited at 250 °C , however, exhibit much lower maximum mobility around $10^{-3} \text{ cm}^2/\text{V-sec}$. It is also observed that the field effect mobility of devices with 250 °C AlN film suffers pronounce degradation under high gate bias. Since the field effect mobility can be strongly affected by the dielectric

conditions, [32,33] we compare the surface morphology and the leaky properties of these AlN films deposited at different temperatures. As shown in Fig. 4-3-4 (a), (b) and (c), the AFM images reveal that the average surface roughness decreases from 0.34, 0.21 to 0.14nm while the deposition temperature is reduced from 250°C, 200°C, to 150°C. On the other hand, as shown in Fig. 1, the leakage current of AlN film also decreases with decreasing deposition temperature. It is known that the surface irregular causes locally strong electric field and results in leakage. [34] Reducing the roughness effectively suppresses the leakage and also reduces the surface scattering effect. Moreover, dielectric surface roughness is also a crucial parameter that influences the pentacene deposition. [35] When we compare the morphology of pentacene film grown on these three kinds of AlN films in Fig. 4-3-4 (d), (e), and(f), pentacene film turns to be dendritic structure and exhibits larger grain size as the AlN surface becomes smoother. Therefore, it can be concluded that lowering the AlN deposition temperature gives smaller leakage current and larger pentacene grain size. The field effect mobility is accordingly improved. The process is promising for the development of low-temperature OTFTs.

Besides, we also tried to deposit the AlN film at room temperature (25°C). The surface roughness and the profile image were verified by the AFM and SEM microscope. As show in the AFM image of Fig. 4-3-5(a), we can observe that under a very low deposition temperature, the surface was pinhole free and its roughness was still less than 0.2nm. The result can be as well as the AlN film deposited at 150°C. In Fig. 4-3-5(b), we can observe that the deposited AlN film thickness is less than 70nm. We further compare the crystalline changes in the AlN films, when we change the AlN film deposition temperature. In Fig. 4-3-6, we show the x-ray diffraction (XRD) spectrum of AlN films, which are deposited at 250°C, 150°C, and 25°C. When the AlN deposition temperature was lowered, the crystalline signal was also reduced at

the same time. The result is a proof of that higher deposition temperature may result in higher AlN crystallinity. The high AlN crystallinity implied the existence of grain or micro crystalline structure inside the AlN film. As a result, since the low temperature AlN film is not perfect crystalline, the grain or micro crystalline structure may be inserted between amorphous AlN. The amorphous and crystalline boundary may be a leakage path. However, when the deposition temperature was reduced, the AlN will become more amorphous and the crystalline boundary will also decrease at the same time. The AlN dielectric leakage was than be reduced.

In Fig. 4-3-7(a), we showed the dielectric leakage of room temperature deposited and thin AlN film (<70nm). The leakage current can be kept at a very low level about $10^{-8} \sim 10^{-9} \text{ A/cm}^2$, which was similar to the result of AlN film deposited at 150°C . We also utilized this AlN dielectric to fabricate the OTFT. The AlN-OTFT transfer characteristic was shown in Fig. 4-3-7(b), the device can also be operated at a low voltage (<5V) with high on/off current ratio ($>10^5$). The field effect mobility is about $0.05 \text{ cm}^2/\text{V}\cdot\text{sec}$ and the subthreshold swing is about 0.12V/decade. It shows the potential of using the room temperature AlN gate-dielectric for OTFT for advance application.

The pentacene-based OTFTs with AlN gate insulator had been fabricated and characterized. By using RF-ICP sputtering system, AlN film exhibiting low leakage current and high breakdown field can be deposited at low temperature. The surface roughness can be controlled to be less than 2\AA by lowering the deposition temperature. As a result, the morphology is suitable for the pentacene dendritic structure growth and therefore improves carrier mobility. The field effect mobility about $0.24\text{cm}^2/\text{V}\cdot\text{sec}$ and the sub-threshold swing about 0.4V/decade can be obtained from our devices. Further improvement is expected by pentacene purification in future studies.

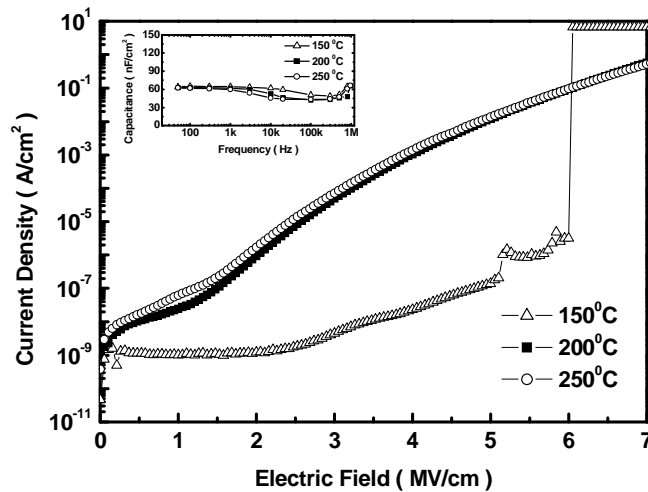


Fig. 4-3-1 The leakage current of the Au-AlN-Si structure as a function of the electrical field and gate voltage. The inset is the capacitance measured from the same structure under various frequencies.

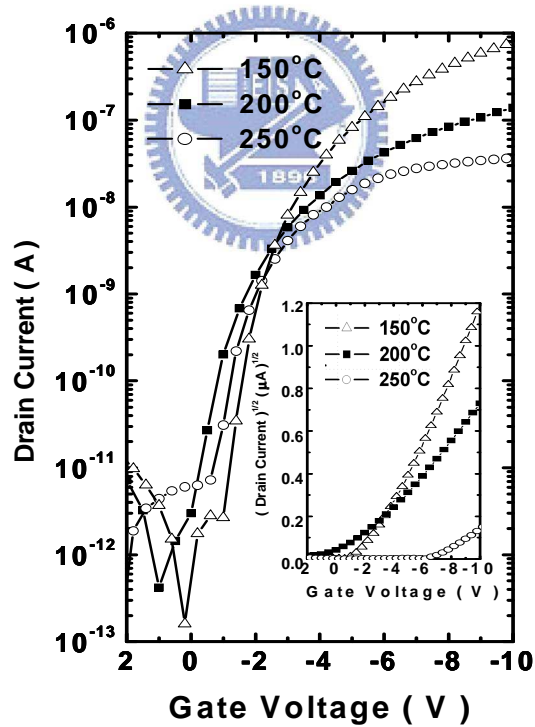


Fig. 4-3-2(a) The transfer characteristics of OTFTs with 150°C, 200°C, and 250°C AlN gate dielectric. The drain bias is -3V. The inset shows the plot of square root of drain current versus the gate voltage when the drain bias is -7 V.

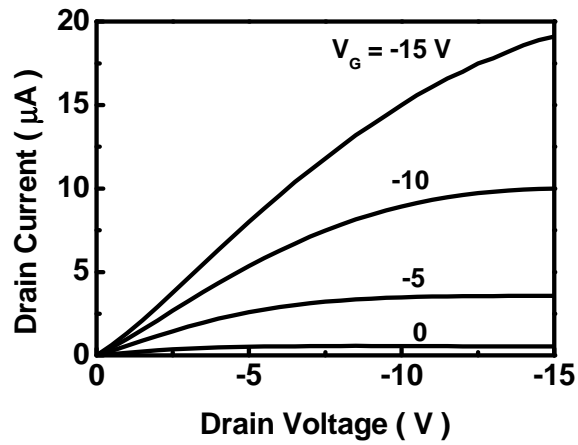


Fig. 4-3-2(b) The output characteristic of the OTFTs with 150°C AlN gate dielectric.

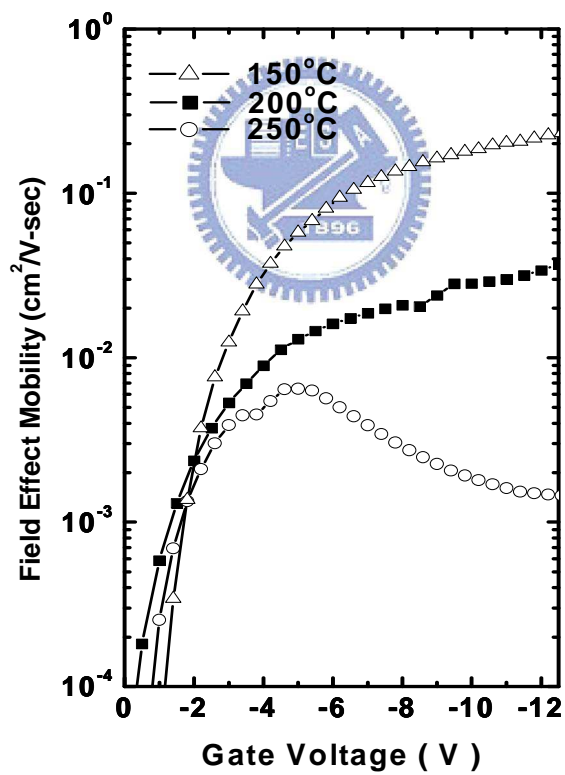


Fig. 4-3-3 The field effect mobility of OTFTs with 150°C, 200°C, and 250°C AlN gate dielectric. The drain bias is -3 V. The field effect mobility is extracted from the linear region transconductance.

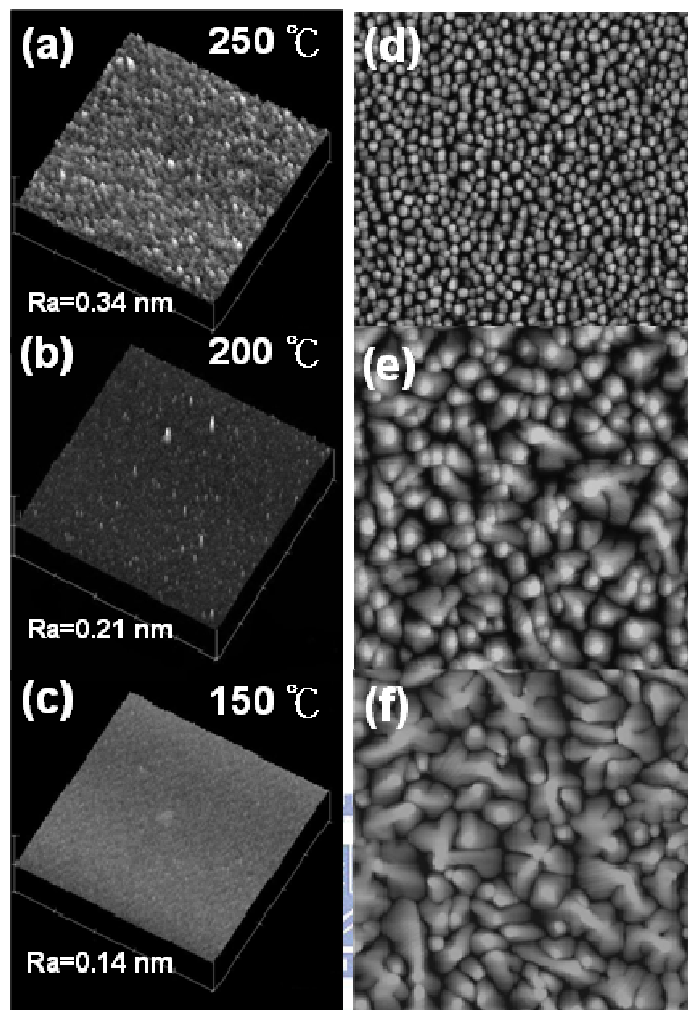


Fig. 4-3-4 The AFM images of AlN films deposited at 250 °C, 200 °C, and 150 °C are shown in Fig. 4(a), (b), and 4(c), respectively. The corresponding AFM images of pentacene films grown on the 250 °C, 200 °C, and 150 °C AlN dielectrics are shown in Fig. 4(d), 4(e), and 4(f). The scanning size is fixed to be $5 \times 5 \mu\text{m}^2$.

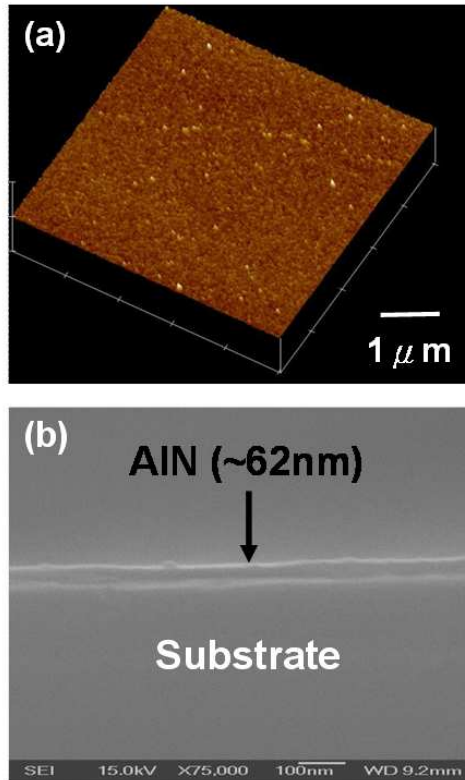
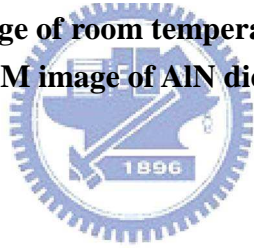


Fig. 4-3-5 (a) The AFM image of room temperature deposited AlN film surface, and (b) is the SEM image of AlN dielectric profile.



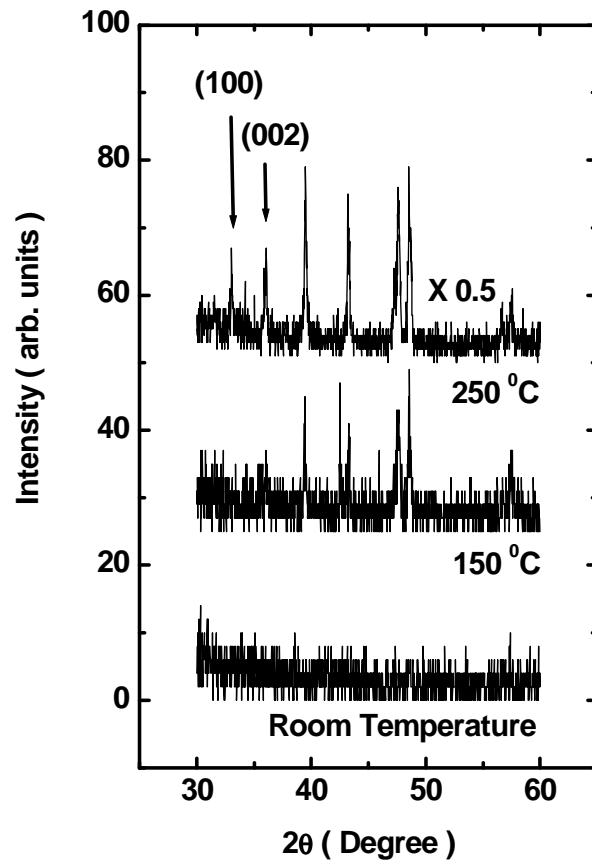


Fig. 4-3-6 The x-ray diffraction spectrum of AlN film deposited on the Si wafer under different deposition temperature (250°C, 150°C, 25°C room temperature).

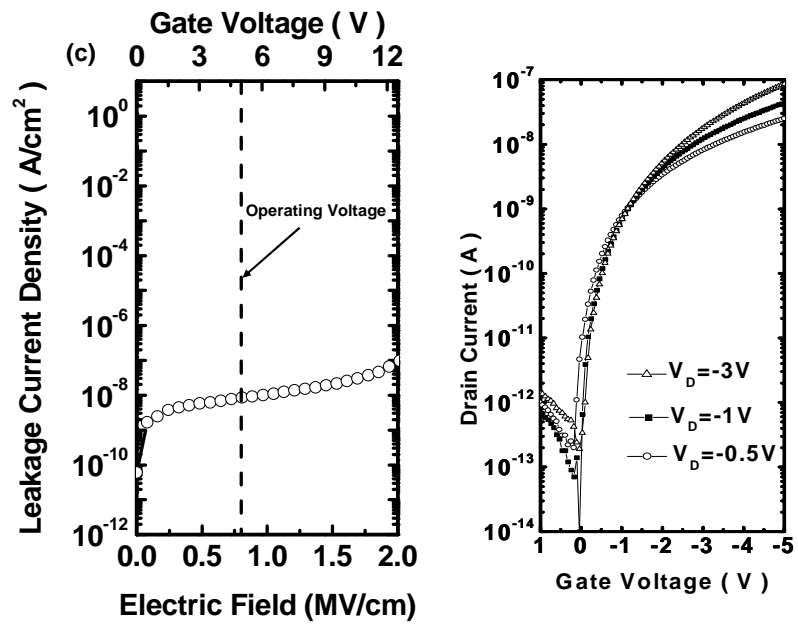
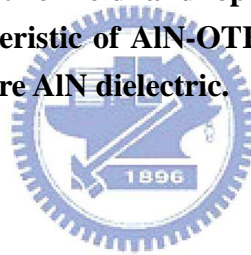


Fig. 4-3-7 (a) The room temperature AlN dielectric leakage is plotted as a function of electric field and operation voltage, and (b) is the transfer characteristic of AlN-OTFT, which was fabricated on the room temperature AlN dielectric.



4-4. Effects of Ar/N₂ Flow Ratio on AlN Gate Insulator

Fig. 4-4-1(a) plots the X-ray photoemission intensity of nitrogen versus binding energy. As presented in the X-ray photoemission spectrum (XPS), the N 1s core level emission around 397eV and the azide emission around 402eV were observed from the three AlN samples. When the Ar/N₂ ratios were altered from 2/5 to 2/7 and to 2/9, the nitrogen signals became more intense and the azide signals were unchanged. Accordingly, in the AlN film, the mass of nitrogen should increase with the nitrogen-gas component. Evidently, increasing the nitrogen gas ratio effectively increases the nitrogen chemical composition in the AlN. Fig. 4-4-1(b) presents the leakage-current densities (J) from three MIS samples in various electric fields (E). The Ar/N₂-gas ratio was then changed from 2/5 to 2/7 and 2/9, to suppress leakage. As shown in Fig. 4-4-1 (b), the leakage current was suppressed from $3.8 \times 10^{-6} \text{ A/cm}^2$ to $6.2 \times 10^{-7} \text{ A/cm}^2$ and $2.2 \times 10^{-10} \text{ A/cm}^2$ in an electric field of 2MV/cm.

To further study the conduction mechanism in AlN, the leakage current density was plotted as the function of electric field in log-log scale ($\log(J)$ vs. $\log(E)$) in Fig. 4-4-2(a). Clearly, two transports mechanisms are observed under the low electric field and high electric field. An Ohmic-conduction can be linearly fitted under low electric field, but the conduction transferred into nonlinear under high electric field. If the Ar/N₂ gas ratios were changed from 2/5 to 2/7 and 2/9, the transfer points were also changed from 0.8 to 1.2 and 2.7 MV/cm, respectively. We illustrated the J-E curves as Poole-Frenkel plots ($\ln(J/E)$ vs. $E^{1/2}$) in Fig. 4-4-2(b). As shown in the plots, a satisfactory fitting can be observed in each curve under the high electric field. Our result was good agreed with the proposed Poole-Frenkel transport in AlN. If we consider the defect distribution in AlN film, it is investigated that the corresponding defects near the conduction band were the nitrogen vacancies.[4,27] Thus, the

increase of nitrogen flow rate in the sputtering process may be an effective way to compensate the nitrogen vacancies and suppress the potential leakage path in AlN.

To further understand the Poole-Frenkel-like transport in the AlN film. We tried to verify its leakage properties by measuring the temperature dependent AlN film leakage. Since it has been suggested that the nitrogen related defect should be influence the AlN film leakage. Thus, we chose the AlN films deposited under different nitrogen flow rate (Ar/N₂ is 2/7, 2/9, and 2/12) with different nitrogen containment for comparison. By using the Poole-Frenkel current formula [36]:

$$J = C \cdot E \exp\left(-\frac{\beta_{PF} E^{1/2} - q\phi_{PF}}{k_B T}\right)$$

Where C is a constant, E is the electric field, β_{PF} is the Poole-Frenkel coefficient, which is defined as $\sqrt{\frac{e}{\pi\epsilon}}$, and ϵ is the dielectric constant. ϕ_{PF} is the potential depth of defect, k_B is the Boltzmann constant, and T is the absolute temperature. We can understand the effects of the Ar/N₂ gas flow ratio on Poole-Frenkel-like defect distribution. As we plotted the electric field dependent Poole-Frenkel barrier height, we can observe the original Poole-Frenkel barrier height under zero biasing from Fig. 4-4-3(a), 3(b), and 3(c). When the nitrogen flow rate is increased from 7sccm, to 9sccm, or to 12sccm, the barrier height of Poole-Frenkel-like defects will increase from 0.34eV, to 0.5eV, and to 0.63eV. The result shows that the increase of nitrogen flow rate may influence the nitrogen related defect distribution significantly. It is probable that when the defect distribution is shifted toward a deeper level, the probability of carrier reemission from the defect sites may be reduced at the same time. As a result, the AlN film dielectric leakage was than be reduced.

To fabricate the low-voltage OTFTs, we used the thinner AlN film (~70nm) as the gate dielectric. From our measurement, the capacitances were about 92nf/cm². The

output characteristics are shown in Fig. 4-4-4, the transistor can be saturated at low drain voltage (about -3V). The transfer characteristic is shown in Fig. 4-4-5(a). In Fig. 4-4-5(a), the AlN-OTFTs are operated lower than 5V. The high on/off current ratio about 10^6 can be achieved even under an extremely low drain bias -0.5 V. Additionally, the subthreshold swing can be as low as $\sim 104\text{mV/decade}$. The squared-drain-current ($I_D^{1/2}$) plotted as a function of gate voltage is shown in Fig. 4-4-5(b). When the drain-voltage is biased at -3V, the extracted threshold voltage and the field effect mobility was about -1.5 V and $0.02\text{cm}^2/\text{V}\cdot\text{sec}$, respectively. Since the maximum interface trap density can be estimated by the approximation [15]:

$$N_{ss} = \left[\frac{S \cdot \log(e)}{kT/q} - 1 \right] \cdot \frac{C_i}{q}$$

where S is the subthreshold swing, C_i is the capacitance per unit area, k is Boltzmann's constant, and T is the absolute temperature. By assuming $C_i = 92\text{nf}/\text{cm}^2$ and $S = 104\text{mV/decade}$. From our calculation, the approximate interface trap density in our devices is $4.2 \times 10^{11}\text{cm}^{-2}\text{eV}^{-1}$. This trap density is quite low and slightly better than the best records of other OTFTs. [37-39] Many researchers proposed that dielectrics with lower surface-free-energy were good for pentacene deposition and created lower interfacial traps. [40,41] When the surface-free-energy reduced, the pentacene grains were more close-packed and stacked in higher coverage. Thus, the OTFTs performances were also improved. The result indicated that the surface-free-energy may be an important factor that influences the interfacial defects between dielectrics and pentacene. So we tried to use the contact-angle measurement to determine the surface-free-energy of AlN. [40] The contact-angle between deionization water and AlN was about $77.0^\circ \pm 2$. The result showed that AlN film was more hydrophobic than the oxide-based dielectrics. Based on the measurement, the surface energy was

about $38.5 \pm 1 \text{ mJ/m}^2$. The magnitude was similar to those of polymer dielectrics and close to that of the pentacene film.[41] Accordingly, the outstanding subthreshold swing and low interfacial traps may be attributed to the hydrophobic AlN dielectric. Like the polymer dielectrics, low-surface-energy AlN film provides a similar surface condition for pentacene crystallization and minimizes the interfacial trapping defects.

In summary, the pentacene-based OTFTs with low temperature AlN gate insulator had been fabricated and characterized. By using RF-sputtering system, the AlN thickness can be controlled as thin as $\sim 70\text{nm}$. It was also demonstrated that the Ar/N₂ flow ratio in sputtering process was a key parameter to reduce AlN gate leakage. The Poole-Frenkel related conduction could be suppressed and retarded to higher electric field. With the extremely thin AlN film as gate dielectric, the OTFT operating voltage was dramatically reduced to less than 5V. The lowest subthreshold swing $\sim 0.104\text{V/decade}$ and threshold voltage -1.5V can be obtained from AlN-OTFTs. The field effect mobility and the on/off current ratio was about $0.02\text{cm}^2/\text{V-sec}$ and more than 10^5 , respectively.

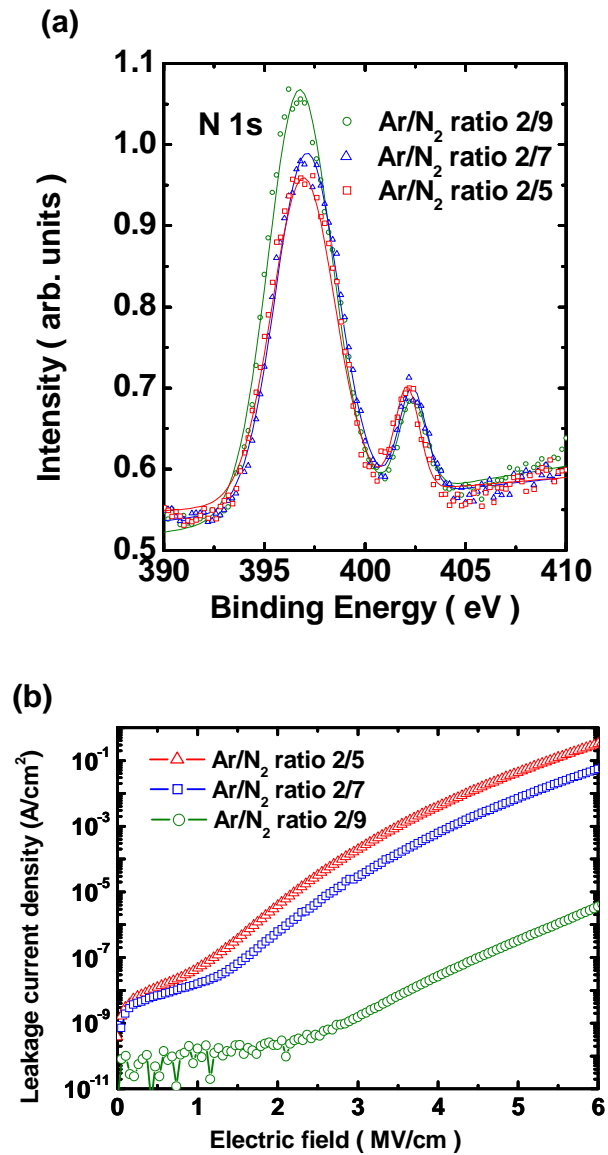


Fig. 4-4-1 (a) The x-ray photoemission spectrum (XPS) of three distinct AlN samples, the AlN samples were sputtered under different Ar/N₂ gas ratio: 2/5, 2/7 and 2/9, respectively. (b) The comparison of leakage-current (J) vs. the electric field (E) from these three MIS structures.

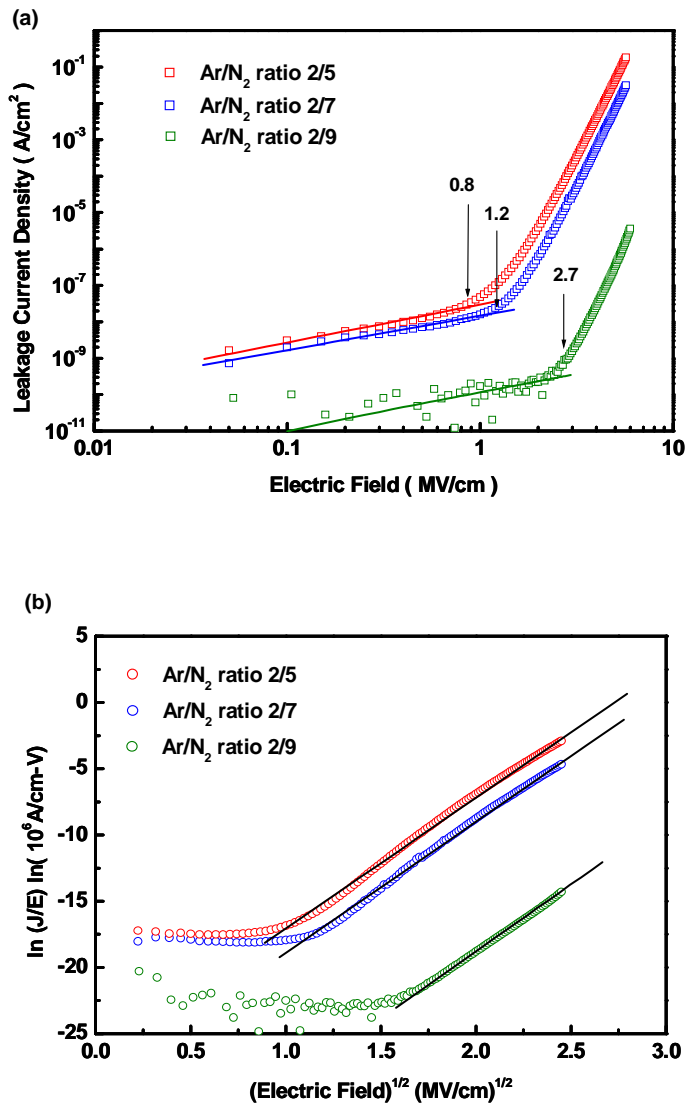


Fig. 4-4-2 (a) The leakage current from three MIS structures are plotted as a function of electric field in $\log(J)$ - $\log(E)$ scale and (b) in $\ln(J/E)$ - $(E)^{1/2}$.

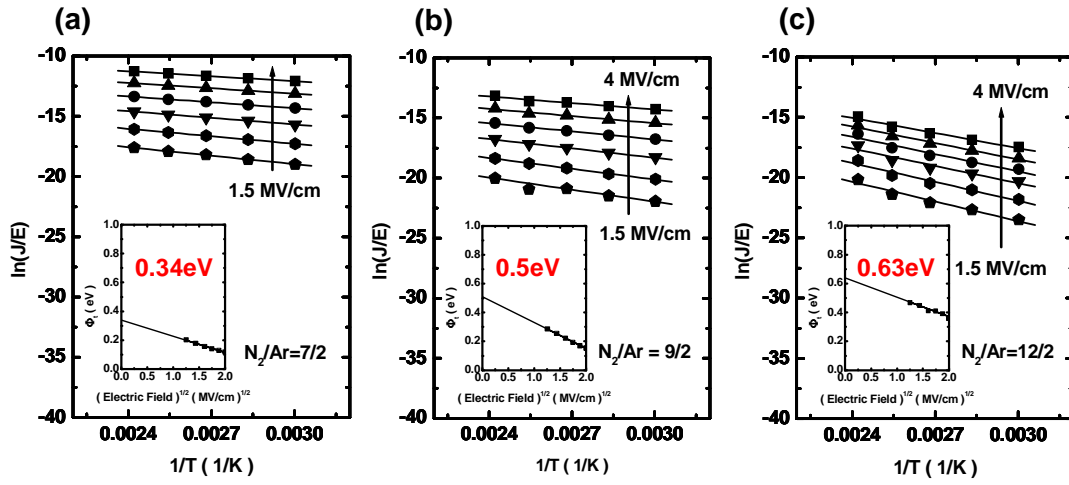
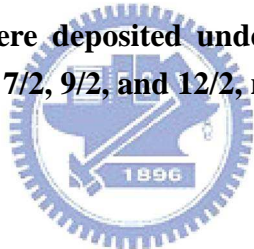


Fig. 4-4-3 (a), (b), and (c) are the Poole-Frenkel plots measured under different temperatures and electric field. We may extract the zero biasing Poole-Frenkel-like defect barrier depth by plotting the ϕ_{PF} as a function of electric field. The AlN films we used for measurement were deposited under different Ar/N₂ ratio, which was varied from 7/2, 9/2, and 12/2, respectively.



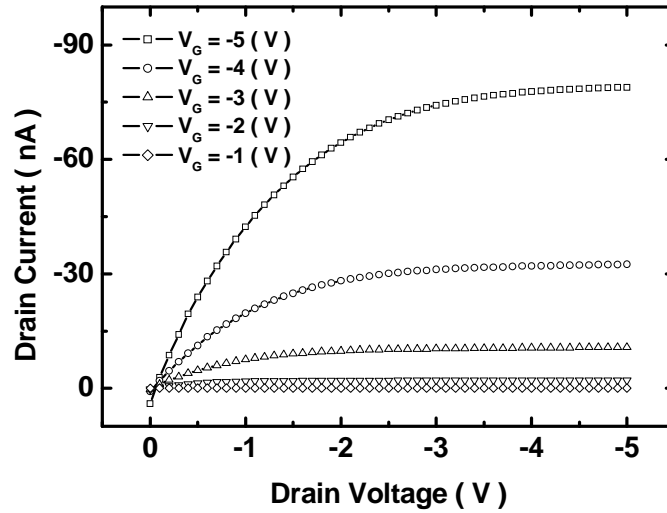


Fig. 4-4-4 The output characteristic of the OTFTs with 150°C AlN gate dielectric.

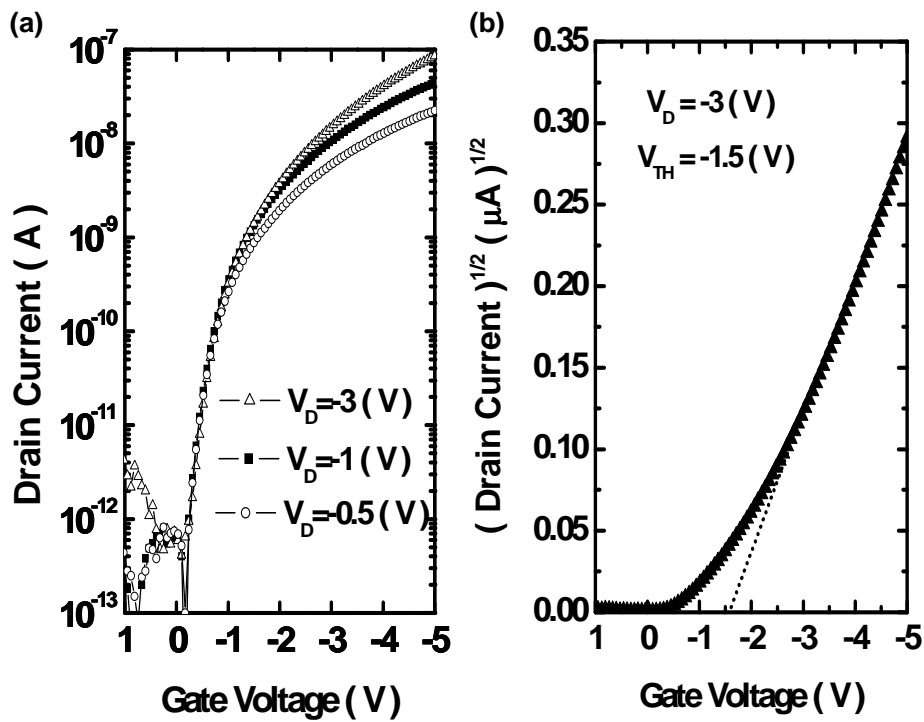


Fig. 4-4-5 (a) The transfer characteristics of AlN-OTFTs under different drain voltages. (b) The squared drain current ($\sqrt{I_D}$) is plotted as a function of gate voltage. The drain voltage is -3V and the threshold voltage is -1.5V, respectively.

4-5. Low-Voltage Organic Thin Film Transistors with Hydrophobic Aluminum Nitride Gate Insulator

In our previous investigation, the AlN film was deposited at a higher substrate temperature [42]. The AlN film has a grain-structure and is highly c-axis oriented. If the AlN film is deposited at high temperature to form the gate-dielectrics, the grain boundaries will affect the surface roughness and reduce the uniformity. The grain boundaries commonly serve as leakage paths. Since the dielectric roughness and leakage are critical in OTFT fabrication, in this work, AlN was deposited at a lower substrate temperature (150°C). Fig 4-5-1(a) reveals the AFM image of the 150°C AlN film. Unlike a high-temperature AlN film, the 150°C AlN film was smooth. The surface roughness was only 0.18nm. Fig 4-5-1(b) presents the scanning electron microscopic (SEM) image to verify the dielectric quality. In the 150°C sputtered AlN film (with a thickness of around 50nm), no significant surface irregular and pinholes were observed. The fluctuation of dielectric thickness is appeared; it may result in performance variation when OTFT size is reduced to micro-scale. The 150°C AlN film had favorable surface properties. The dielectric properties were also examined. The measured capacitance of the MIS structure was approximately 104nF/cm². Fig 4-5-1(c) shows the gate-leakage, which was as low as $\sim 10^{-8}$ A/cm² in an electric field of 1MV/cm.

In this investigation, OTFTs were fabricated with thin AlN film (thickness is about 50nm, dielectric constant is about 6~7 as gate-dielectric. Fig 4-5-2(a) presents the transfer characteristics. The AlN-OTFTs can be operated at a relatively low voltage (~ 5 V). The on/off current ratio was about 10^6 ; the threshold voltage was only -2.1V; the field effect mobility was 1.67cm²/V-sec. The subthreshold swing was 170mV/decade. The magnitude approached the theoretical minimum, ~ 60 mV/decade

$(kT/q \cdot \ln(10))$ [15]. Fig 4-5-2(b) shows the output characteristics, the AlN-OTFT were operated in the saturation region at low drain bias ($\sim 3V$). Since the subthreshold swing represents the interface quality and the trap behavior, [43] the maximum interface trap density is given by the approximation, [15]

$$N_{ss} = \left[\frac{S \cdot \log(e)}{kT/q} - 1 \right] \cdot \frac{C_i}{q}$$

where S is the subthreshold swing; C_i is the capacitance per unit area; k is Boltzmann's constant, and T is the absolute temperature. Substituting $C_i = 104 \text{ nf/cm}^2$ and $S = 170 \text{ mV/decade}$ yields an approximate interface trap density in the devices of $1.2 \times 10^{12} \text{ cm}^{-2} \text{ eV}^{-1}$. To the authors' limited knowledge, this value is close to the lowest reported for organic transistors. [31, 44]

The organic/dielectric interface defects strongly affect the performance of OTFTs. Surface polarity is key to reducing the interface defect. SAM-treatment and a polymer dielectric are widely employed to change the polarity of the surface. Researchers have recently demonstrated that interface defects can be minimized by changing the dielectric polarity. Accordingly, the AlN surface polarity was determined herein. The modified Fowkes' equation for the surface polarity in terms of the surface energy is introduced: [40]

$$(1 + \cos \theta) \gamma_L = 2(\gamma_S^d \gamma_L^d)^{1/2} + 2(\gamma_S^p \gamma_L^p)^{1/2}$$

where θ is the contact angle between probing liquid and the solid surface; γ_L is the total surface free energy of the probing liquid; γ_L^d is the dispersion component, and γ_L^p is the polarity component. Based on this approximation, the total surface free energy of the solid surface is,

$$\gamma_S = \gamma_S^d + \gamma_S^p$$

where the total surface free energy γ_s is the sum of γ_L^d (dispersion component) and γ_L^p (polar component). The surface free energy can be calculated by measuring the contact-angle between the solid surface and the different probing liquids. As shown in Figs. 4-5-3(a), (b), and (c), the optical images of various liquid drops on the 150°C AlN films were captured using a CCD camera. The water-AlN, ethylen glycerol-AlN and diiodo methone-AlN contact angles were $72.9^\circ \pm 5^\circ$, $60.7^\circ \pm 4^\circ$ and $43.8^\circ \pm 2^\circ$, respectively. The Owens-Wendt-Rabel and Kaelble's method [40] yields an estimated surface energy of AlN of $38.3(\text{mJ}/\text{m}^2)$. As stated in Table 4-5-1; compared to the inorganic dielectrics, the AlN had a low surface free energy [45,46]. The surface free energy was unusually lower than those of polymer dielectrics [4,41], pentacene, [41] and the HMDs-treated SiO_2 [47]. It was close to that of OTS-treated SiO_2 [47]. The particular characteristic differs from those of the other ceramic-based dielectrics. According to Chou *et al.*'s investigation [48], the deposited pentacene film is composed of both orthorhombic and triclinic pentacene. The “dielectric” surface free energy matched to the “orthorhombic pentacene film” ($38\text{mJ}/\text{m}^2$) is the key factor to the high mobility OTFTs. It is believed that the voids and the incompletely stacked layers, which limited the carrier transport in the pentacene film, are reduced due to the match of surface energy [49]. In this study, the surface free energy of AlN agrees very well with that of the orthorhombic pentacene film, but not to the triclinic pentacene film [50]. Based on these arguments, the high performance AlN-OTFT is attributed to the match of orthorhombic pentacene film with AlN.

An AlN film was used as the gate dielectric for OTFTs. The pinhole free, smooth and extremely thin AlN film can be deposited by the RF-sputtering system at 150°C. This low-temperature deposition process enables the potential application on polymer substrates. The dielectric leakage was significantly low, and the AlN has a surface

free energy that is similar to that of the pentacene film. The transfer and output characteristics demonstrate that the AlN-OTFT has potential application in low-voltage and rapid-switching organic transistors.



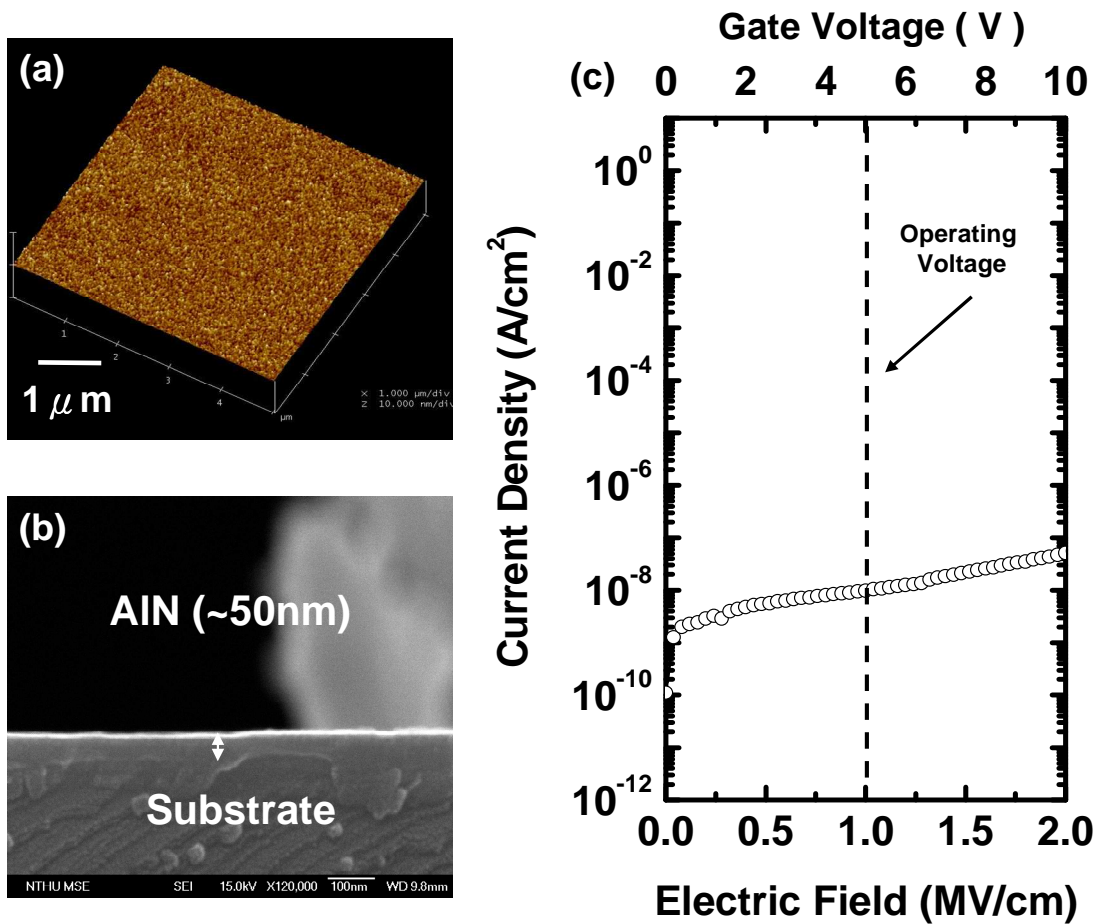


Fig. 4-5-1. (a) The AFM image shows the 150°C AlN film, and the scanning size is 5×5 μm². (b) The SEM image is the cross-section view of the AlN film on substrate. (c) The leakage current of the Au-AlN-Si structure as a function of the electric field and gate voltage.

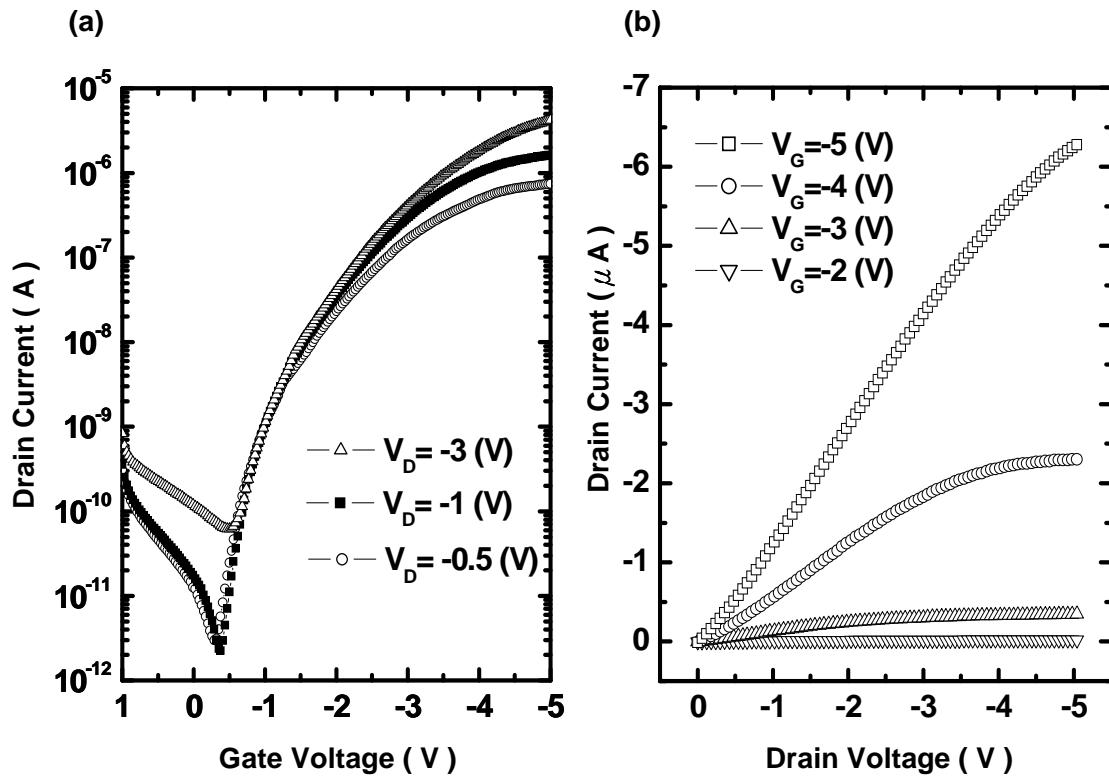
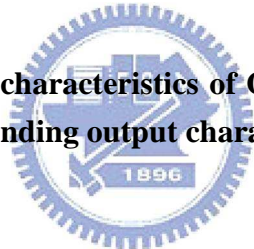
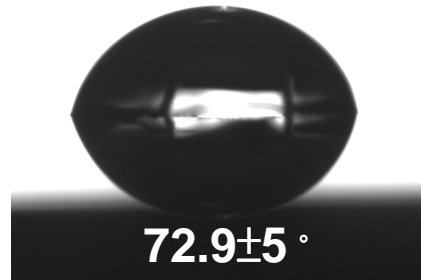


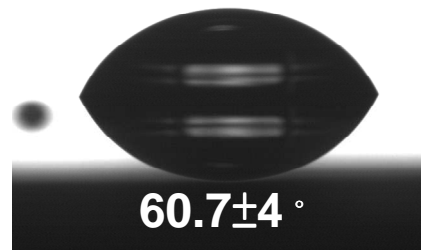
Fig. 4-5-2. (a) The transfer characteristics of OTFTs with AlN gate dielectric.
 (b) The corresponding output characteristic.



(a) Water



(b) Ethylen glycol



(c) Diiodo-Methane

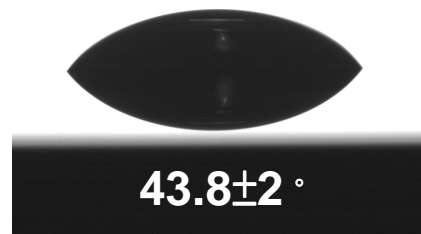


Fig. 4-5-3. (a) The water, (b) ethylene glycol, and (c) diiodo-methane drops on the 150°C AlN film for the surface-energy measurement. Each value below the drop indicates the contact-angle between the liquid drop and the AlN film. The entire optical images were captured from the CCD camera.

Substrate	Contact Angle between Liquid and Sample			Surface Free Energy (mJ/m ²)	Reference
	D.I. Water	Glycerol	Di-iodomethane		
Al ₂ O ₃	20-37			68-78	[15]
Si ₃ N ₄	20-30			55-60	[16]
SiO ₂	35.7	22.4	25.1	60	[20]
PVA	53.9	54		46.3	[17]
HMDs+SiO ₂	53.7	53.7	43.9	45.4	[20]
PVP-copolymer	50-60			42	[18]
Pentacene				38,42-48	[19],[21]
AlN	72.9±5	60.7±4	43.8±2	38.3	This work
OTS+SiO ₂	78.9	81.8	43.9	34.9	[20]

Table. 4-5-1. Contact-angle measurements and the corresponding surface free energy of the commonly used dielectrics in the OTFTs fabrication.



Chapter 5

High Photo Responsivity of Pentacene-based Organic Thin-Film Transistors with UV-treated PMMA Dielectrics

5-1. Introduction

Organic thin-film transistors (OTFTs) have received intense attention due to their low cost, light weight, and low-temperature processing compatible with flexible substrates. The integration of OTFTs with other organic devices such as the organic light-emitting devices and the organic solar cells also opens up the field of flexible optoelectronics.[1, 2] In this field, OTFTs not only act as field-effect transistors, but their application in phototransistors is also important for light detection and photoswitching. However, only a small number of researchers have published works on the organic photo transistors. Researchers have observed reversible photo current and light-induced threshold voltage shift.[3-5] Pentacene-based OTFTs with Ta₂O₅ gate dielectrics was also proposed to obtain high photo responsivity.[4] In this paper, a new approach to enhance photo responsivity of pentacene-based OTFTs is proposed. By using poly(methyl methacrylate) (PMMA) as the dielectric and applying UV-light treatment, photo responsivity of OTFTs can be significantly enhanced. By analyzing the response lifetime, the underlying mechanism is investigated carefully. The proposed approach is simple and compatible with the development of all-organic electronics.

5-2. Experimental

5-2-1 Device Fabrication

First, the Ni/Pd bi-layer was deposited on a glass substrate as gate electrodes. The PMMA was dissolved with a 95 weight percent (wt %) in anisole and was spun onto the gate electrodes. Following the curing process, the solvent was removed and the PMMA was solidified to serve as a gate dielectric. Then, some samples were exposed to UV-light (wavelength = 175-285nm and output power = 40mW) for 90sec. Before the OTFT fabrication, the surface energy of standard PMMA and UV-treated PMMA were verified. As demonstrated in [Table 5-1](#), the UV-treatment seemed not influence the significantly. The surface energy of both PMMA dielectric were about 44-46 mJ/m². Both the UV-treated PMMA and the untreated (standard) PMMA dielectrics were transferred into a vacuum chamber for the deposition of 100-nm-thick pentacene film and the 100-nm-thick gold (Au) electrodes. The device channel width (W) and length (L) were 1000 μ m and 100 μ m, respectively.

5-2-1 Illumination System

The illumination system was a combination of a probing bench (Cascade microtech, RHM-06) and a halogen lamp (OPTeM, Lamplink 2). The maximum lamp power was 150W and filtered at a wavelength of about 460nm by using a band-pass filter with a full width half maximum (FWHM) about 10nm. The filtered-light was guided by an optical fiber and focused on the OTFTs by using a microscope. The illumination system was shown in [Fig 5-1](#). The excitation light is guided by the optical fiber and focus by the microscope. We put the band pass filter before the light was projected onto the OTFT. The system is stepped on a probing stage, thus, we may measure the real-time OTFT IV characteristic under light excitation.

5-3. PMMA OTFT with/without UV-treatment (before illumination)

The transfer characteristics of standard PMMA-OTFTs and UV-treated OTFTs are compared in Fig. 5-2. The latter ones exhibit larger subthreshold swing ($S.S.$) and positively-shifted threshold voltage (V_{th}). The results are consistent with other reports and a plausible explanation is that UV treatment creates excess negative-charged sites on the pentacene/PMMA interface.[6,7] Accordingly, the $S.S.$ was enlarged and V_{th} positively shifted. However, the linear field-effect mobility (μ_{FET}) was not affected by UV- treatment and was about $0.1\text{cm}^2/\text{Vs}$ for both devices. This indicates that UV treatment does not change pentacene bulk properties. To verify this assumption, the absorption spectrum and X-ray diffraction spectrum of pentacene films deposited on standard PMMA surfaces and on UV-treated PMMA surfaces are compared in Fig. 5-3(a) and in Fig. 5-3(b), respectively. No significant difference could be found between the standard sample and the UV-treated sample. Thus, it is suggested that the UV-treatment affects the interface properties significantly, but does not influence bulk properties of pentacene.

5-4. PMMA OTFT under Illumination

In Fig. 5-4, photo responsivities (R_{ph}) of standard devices and of UV-treated devices are plotted as a function of gate bias minus initial threshold voltage ($V_G - V_{th}^{int}$). This measurement was taken after 1000-sec illumination at an intensity of about $45\mu\text{W}/\text{cm}^2$. Photo responsivity (R_{ph}) is estimated by using: $R_{ph} = I_{ph} / (E \cdot W \cdot L)$, where I_{ph} is photo-induced excess drain current and E is incident light intensity (W/cm^2).[8] When the gate bias increases, the R_{ph} is enlarged. This is known as the photo-field effect, when electron-hole pairs generated in the band-bending region are swept away by the electric field (from applied gate-voltage V_G and drain-voltage V_D).[3,9] The larger the gate bias, the easier it is to separate the electron-hole pairs to form the photo current. When comparing the R_{ph} of standard

and UV-treated devices, the latter ones exhibit larger R_{ph} than the former. Liang *et al.*[4] reported that carrier trapping in the insulator or at the insulator/pentacene interface may cause a photo-induced threshold voltage shift (ΔV_{th}).[3,4,10] In our experiment, it is plausible that the excess negative-charged sites on the pentacene/PMMA interface produced by UV treatment also enhanced the photo-induced ΔV_{th} .

In Fig. 5-5(a), ΔV_{th} of standard devices and of UV-treated devices are plotted for comparison as a function of time. The devices are illuminated in the initial 1000 sec and then recovered in the dark environment. Obviously, the ΔV_{th} of UV-treated devices is more pronounced than that of standard devices. Since ΔV_{th} under illumination is due to an increase in carrier density,[3,4,10] it is speculated that UV-treatment created negative-charged sites, which enhanced the attraction of photo-generated holes and thus enlarged the threshold voltage shift. When UV-treated devices return to the dark, the negative-charged sites also retard the neutralization of light-induced carriers. The separation and neutralization of light-induced carriers can also be observed by plotting the I_{ph} as a function of time as in Fig. 5-5(b). UV treatment enlarges the photo excess current under illumination and enhances the persistent photo current (PPC) effect during relaxation.[11] The PPC effect has been proposed to be strongly related to interfacial states.[12] PPC can be analyzed by using a double exponential form to fit the photo current relaxation.[11]

5-5. Time-constant Analysis

In the following discussion, the I_{ph} under illumination is fitted by using $I_{ph}(t) = I_1[1-\exp(-t/\tau_1)] + I_2[1-\exp(-t/\tau_2)]$ and the excess current during relaxation I_{ex} is fitted by using $I_{ex}(t) = I_3\exp(-t/\tau_3) + I_4\exp(-t/\tau_4)$, where τ_1 and τ_3 are fast time constants, and τ_2 and τ_4 are slow time constants. The fitted result of OTFT under light excitation and

after light off was shown in Fig 5-6. The rising time constants (τ_1 and τ_2) and recovering time constants (τ_3 and τ_4), which were extracted within the observation time and obtained under different V_G , are plotted as a function of V_G in Fig. 5-7(a) and 5-7(b), respectively. It was observed that the fast time constants (τ_1 and τ_3) are independent of V_G and are not influenced by the UV treatment. On the contrary, the slow time constants (τ_2 and τ_4) exhibited a strong dependence on V_G and were significantly changed by the UV treatment.

5-6. Molecular Simulation

Based on previous discussions, the influence of the UV-treatment on slow time constants can be easily understood. The UV-treatment may modify the PMMA functional end-groups from $-\text{CH}_3$ to $-\text{COOH}$, [13] which will result in the changes of charged-states near PMMA surface. Based on these assumptions, the standard (with $-\text{CH}_3$ end groups) PMMA and UV-treated (with $-\text{COOH}$ end groups) PMMA monomers were estimated by Gaussian 03 with *ab initio* calculation. [14] The basis sets we used in these calculations were 6-311G(d,p), 6-311+G(2d,p), and 6-311+G(2df,2p). After Hartree-Fock (HF) optimization, as shown in Fig. 5-8, it is found the UV-treated PMMA monomer shows a larger dipole moment (2.42-2.5 Debye) than standard PMMA monomer (1.81-1.91 Debye). A larger dipole moment implies that a larger voltage-drop will appear at PMMA surface, which will create a larger built-in electric field (E_{bi}) and enhances hole attraction. Therefore, the generation of I_{ph} is accelerated and the τ_2 of UV-treated devices is smaller than that of standard devices. After the removal of light, the recombination of excess electron-hole pairs is retarded due to E_{bi} . As a result, the τ_4 of UV-treated devices is larger than that of standard devices.

The underlying mechanism of fast time constants, however, is not well understood.

A spatial separation model has been proposed for photo current in OTFTs. As illustrated in Fig. 5-9, the charged sites between PMMA dielectric and pentacene film will influence the carrier concentration locally. When the light was illuminated on UV-treated PMMA OTFT, the charged sites will attract the hole and result in larger photo current and responsivity. After the illumination, the charged site may result in the spatial electron-hole pair separation and retarded the OTFT recovering after photo illumination.

The photo current should be the combination of channel-current and bulk-current.[15] The channel-term has a longer time scale than bulk-term and is gate-voltage dependent. However, the bulk-term is signature of fast response and is independent of gate-voltage. In our study, the fast time constants are not affected by UV treatment and are independent of gate-voltage. A reasonable explanation of fast time constants should be come from photo current, which is weakly connected to channel region.

UV-treatment of PMMA-dielectric is proposed to enhance photo responsivity of pentacene OTFTs. With UV-treated PMMA, a high responsivity of about 10 A/W can be obtained. The enhanced photo responsivity may be due to negatively-charged sites produced by UV treatment on the PMMA surface. As a result, UV-treated devices exhibit increased subthreshold swing, positively-shifted threshold voltage, enhanced photo responsivity, and prolonged persistent photo current during relaxation. By analyzing photo current response time, it was found that gate-bias-dependent time constants are significantly influenced by UV treatment. This analysis explains the UV-treatment effect and gives insight into photo excitation.

Sample	D.I. Water	Glycerol	Di-iodomethane	Surface Energy (mJ/m ²)
PMMA	68.1	47.8	33.8	44.8
PMMA (UV-treated)	62.8	43	34.1	46.9

Table 5-1. The comparison of liquid contact angle and surface energy between standard PMMA (non-treated) and UV-treated PMMA.

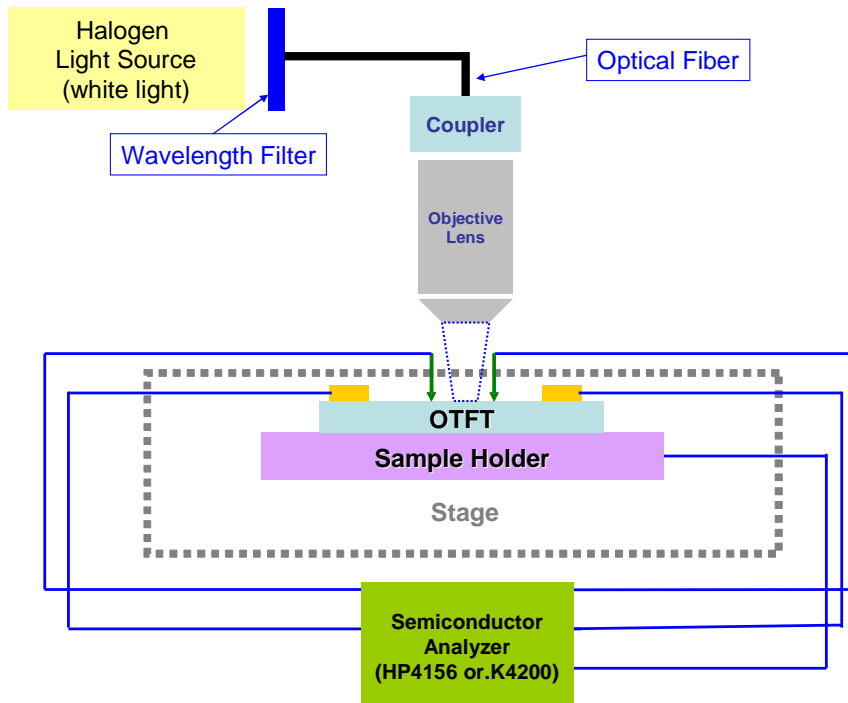


Fig. 5-1 The illumination system of light-excitation on OTFTs.

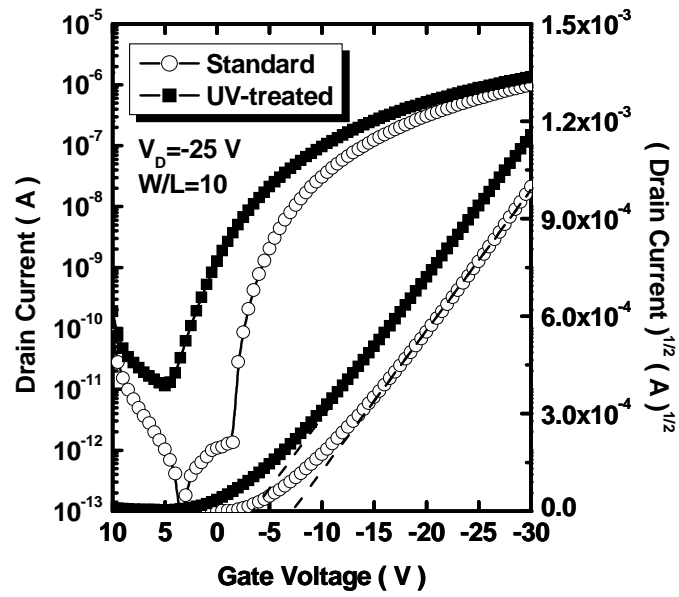


Fig. 5-2. The transfer characteristics of standard PMMA-OTFT (opened circle) and UV-treated PMMA-OTFT (solid square).



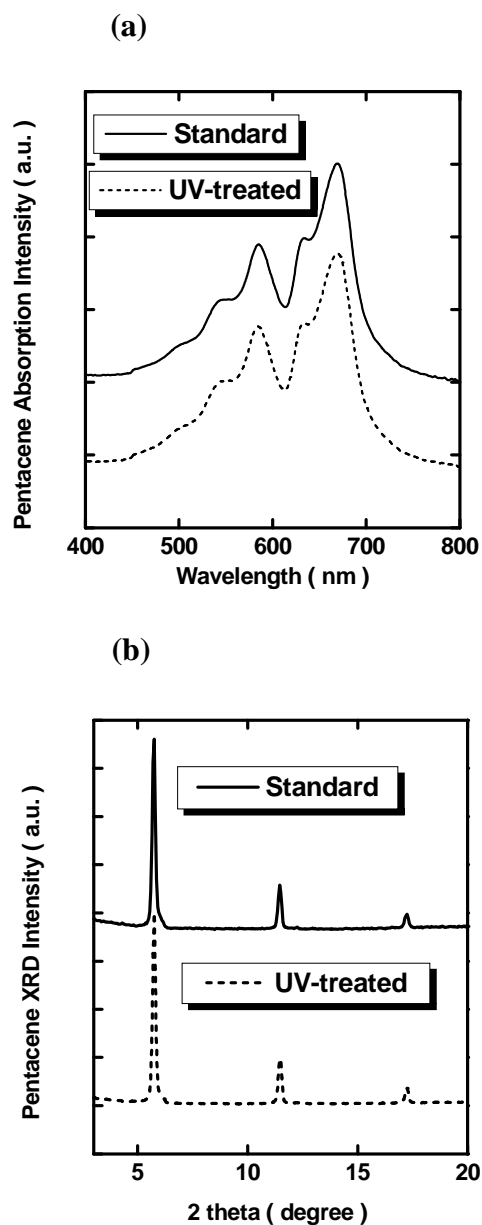


Fig. 5-3. (a) The absorption spectra of pentacene films on standard PMMA dielectric and UV-treated PMMA dielectric. (b) The X-ray diffraction spectra of pentacene films on standard PMMA dielectric and UV-treated PMMA dielectric.

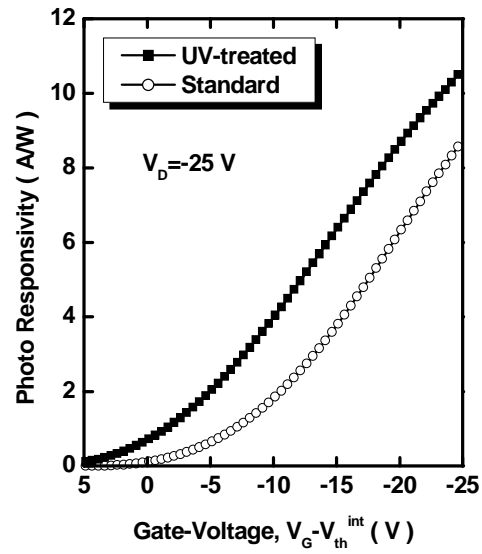
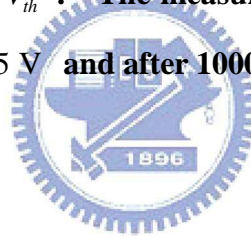


Fig. 5-4. The photo responsivity of standard PMMA-OTFT (opened circle) and UV-treated PMMA-OTFT (solid square) are plotted as a function of $V_G - V_{th}^{int}$. The measurement was made under a drain voltage $V_D = -25 V$ and after 1000sec light-illumination.



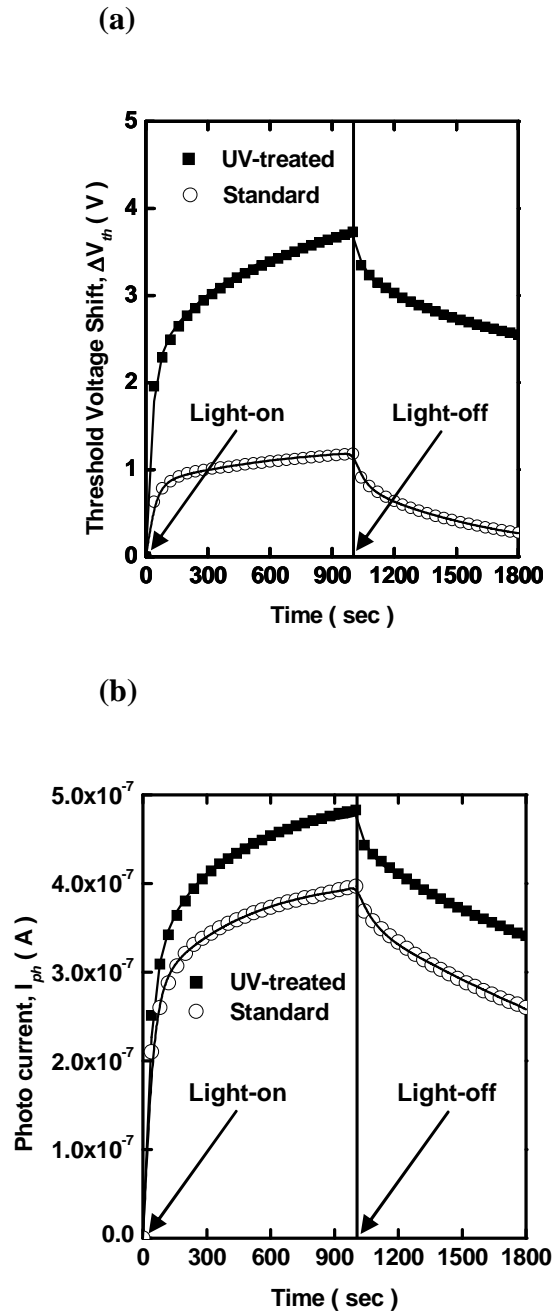


Fig. 5-5. (a) The threshold voltage shift (ΔV_{th}) of standard PMMA-OTFT (opened circle) and UV-treated PMMA-OTFT (solid square) are plotted as a function of time. (b) The photo-induced drain current (I_{ph}) of standard PMMA-OTFT (opened circle) and UV-treated PMMA-OTFT (solid square) are also plotted as a function of time. Both measurements were made under a $V_D = -25$ V.

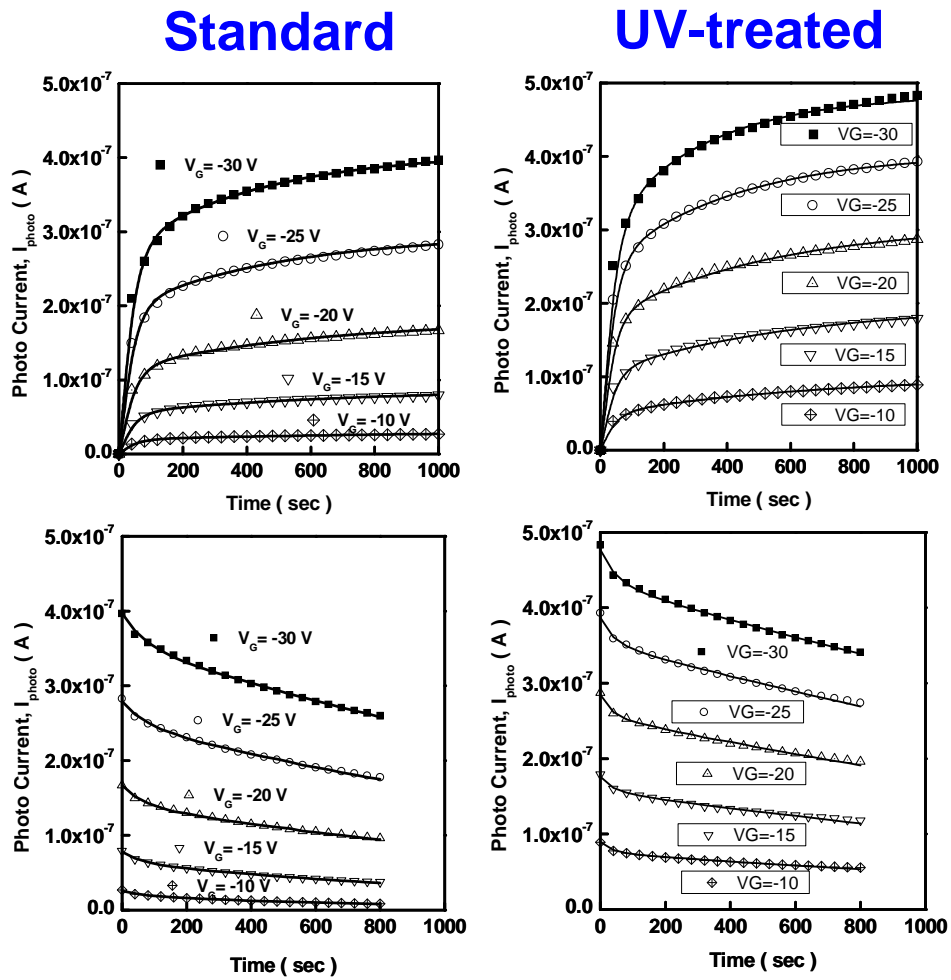
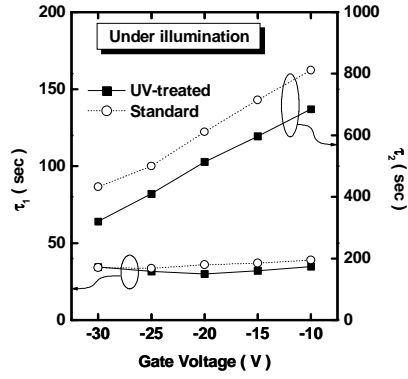


Fig. 5-6. The fitted photocurrents (standard and UV-treated) are plotted as a function of time, which are extracted under different gate-voltage (V_G).

(a)



(b)

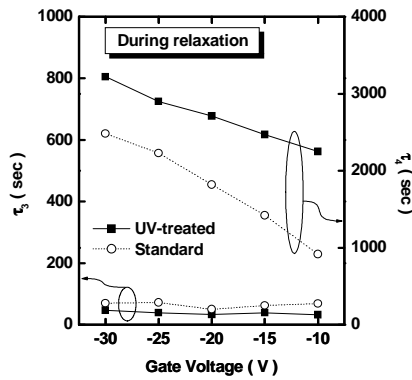
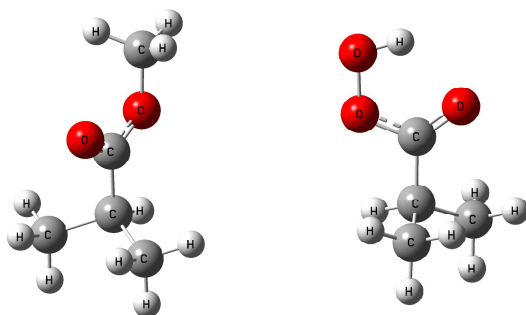


Fig. 5-7. (a) The rising time constants (τ_1 and τ_2) of the fitting curve $I_{ph}(t) = I_1[1-\exp(-t/\tau_1)] + I_2[1-\exp(-t/\tau_2)]$ are plotted as a function of gate-voltage (b) The recovering time constants (τ_3 and τ_4) of the fitting curve $I_{ex}(t) = I_3\exp(-t/\tau_3) + I_4\exp(-t/\tau_4)$ are plotted as a function of gate-voltage.

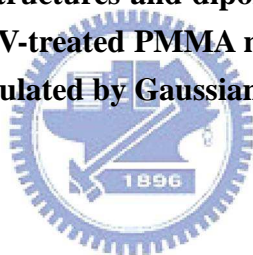


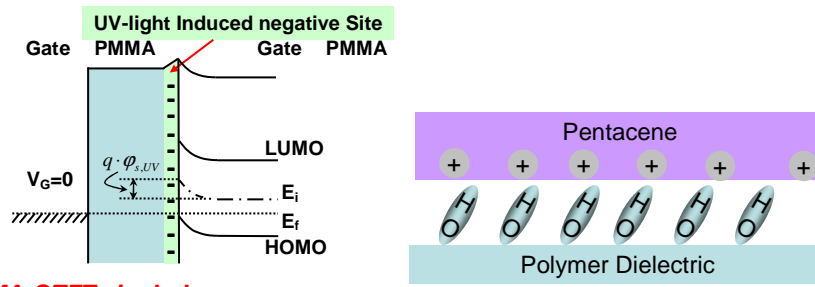
PMMA

UV-treated PMMA

Basis set	Dipole moment (Debye)	
6-311G (d,p)	1.815	2.424
6-311+G (2d,p)	1.894	2.502
6-311+G (2df,2p)	1.912	2.489

Fig. 5-8. The optimized structures and dipole moments of standard PMMA monomer and UV-treated PMMA monomer are plotted as ball and bond type. (Calculated by Gaussian 03, Hartree-Fork method)





PMMA-OTFTs in dark and without biasing

Fig. 5-9. The illustration of UV-treatment induced charged sites on the interface between PMMA dielectric and pentacene film. The interface charge sites may influence the PMMA OTFT photo responsivity significantly.



Chapter 6

Gated-Four-Probed OTFTs in Ammonia (NH₃) Gas Sensing

6-1. Introduction

Recently, organic thin-film transistors (OTFTs) have been intensively studied for used in flexible displays, smart cards, and various kinds of sensors.[1-3] Great progress has been achieved in device engineering and fabrication technologies, OTFT light weight arrays, low-cost processing, and low-voltage drives.[4] Due to organic active layers, OTFTs were found to exhibit high sensitivity to many kinds of gas molecules.[5] The concept of using solution-based OTFTs incorporating ink-jet printing technology for electronic noses has been proposed.[6] Gas sensing mechanisms for OTFTs have also been researched.[7-9] It has been proposed that gas molecules interact with carriers in conduction channels at dielectric interface. Polarized molecules, such as water molecules, are believed to diffuse into grain boundaries and interact with conducting molecules. This may increase grain boundary barrier for carrier transport. This interaction may lead to a reduction in on-current and field-effect mobility.[10] However, it has also been proposed that the source/drain contact resistance or the contact injection barrier is influenced by vapor molecules.[11] The above description indicates that the gas sensing mechanism of OTFTs needs to be clarified, since the variation of contact resistance is incorporated into external field-effect mobility variation. Besides, OTFTs are treated as “multi-parameter” gas sensors,[12] threshold voltage shift and the mobility degradation should be distinguished in sensing behaviors. Therefore, in this report, Gated-four-probed devices are proposed to separately explore device parameter variations in gas sensing.[13] Ammonia (NH₃) was chosen as the analyte in this study. NH₃ gas sensors are useful in many fields such as the food industry, medical

diagnostics, environmental protection and various industrial processes.[14]

6-2. Experimental

Gated-four-probed OTFTs fabricated on p-type Si wafers were used as NH₃ sensors. A 100-nm-thick SiO₂ layer was deposited on the heavily-doped Si. Then, soluble polymethylmethacrylate (PMMA) was spun onto the SiO₂ layer to modify the surface. The capacity of PMMA/SiO₂ dielectric was about 23-24 nF/cm². The pentacene powder we used in this experiment was obtained from Aldrich was about 99%. A 100-nm-thick pentacene layer evaporated through shadow masks at a deposition rate of 0.5 Å/sec at a pressure of ~10⁻⁶ torr. After the pentacene deposition, a 100-nm-thick gold (Au) layer was deposited through shadow masks to serve as source/drain electrodes. The channel width (W) and length (L) of the Gated-four-probed OTFTs were 800 μm and 1200μm, respectively. The distance between two internal probes was about 400 μm. The geometry of the gated-4-probed OTFTs was shown in Fig. 6-1(a). Devices were measured by using a semiconductor analyzer (Keithley 4200-SCS) in a sealed chamber. The inside total chamber-volume was about 42 L and its configuration image was also shown in Fig. 6-1(b). The chamber was initially vacuumed and purged with high-purity (99.99%) nitrogen (N₂). Then, NH₃ gas (Airproduct, >99%) was injected through a mass flow controller (Brooks, MFC 5850E) into the chamber during a controlled time period. The concentration of NH₃ gas in the chamber was estimated as a unit of ppm (mg/L).

6-3. Results and Discussion

The device transfer characteristics measured under different NH₃ concentrations are depicted in Fig. 6-2. NH₃ concentration varied from 0 to 0.52 ppm in increments of 0.065ppm per 6 min. After NH₃ injection, a minimum of 150 sec was allowed to let

the samples come to equilibrium with the environment. The samples were measured after equilibrium. It was observed that, as NH_3 concentration increased, the transfer characteristics shifted, the threshold voltage (V_{th}) became more negative, and on-current ($I_{D,on}$) decreased. The decrease in on-current is generally explained by the interaction between gas molecules and carriers that degrades carrier mobility. The higher the concentration of gas, the lower the mobility and drain current. However, the influence of V_{th} on the $I_{D,on}$ is excluded by plotting drain current as a function of $V_G - V_{th}$ as in the inset of Fig. 6-2. The drain current is still decreased by increasing NH_3 concentration.

To clearly illustrate the variation of device parameters while varying NH_3 concentration, on-current ($I_{D,on}$), threshold voltage (V_{th}), subthreshold swing ($S. S.$), and intrinsic mobility (μ_{int}) were all normalized to their initial values and plotted as a function of NH_3 concentration in Fig. 6-3. The μ_{int} is obtained from the voltage difference between the two interior probes of Gated-four-probed devices.[13] Obviously, both the $I_{D,on}$ and the V_{th} are significantly influenced by varying NH_3 gas concentration. The $S. S.$ remains almost constant. The μ_{int} is decreased with the increase of NH_3 gas concentration. The reason for the threshold voltage shift is still not very clear. A possible reason is that the polarized NH_3 molecules attract carriers from the channel region. As a result, a more negative threshold voltage is needed to turn on the device. The unchanged $S. S.$ denotes that the interface between pentacene and the gate dielectric layer is not affected by NH_3 . [15] The result also verifies the assumption that the gas sensing mechanism is a surface reaction (including grain boundaries) rather than a bulk reaction.[3] The reduction of mobility has been reported in many previous studies.[7-9,16] It is proposed that the

gas molecules adhered to or penetrated into the organic film produces electric dipoles to influence carrier transport.[17] Polarized gas molecules may cause spatial fluctuations of potential energy, which affect the carriers transport in pentacene film. Specifically, grain-boundaries are active regions for the gas molecules interaction.

In those reports, the reduction of on current is mainly attributed to the variation of mobility.[7-9,16] However, in our study, the reduction of on current is much larger than the variation of mobility. The discrepancy between previous reports and our result can be explained in the following discussion.

In previous reports, the external mobility (μ_{ext}) is used to represent the real mobility. Both film resistance (R_{film}) and contact resistance (R_{cont}) influence μ_{ext} . In our study, the intrinsic mobility (μ_{int}) obtained from the voltage difference between the two interior probes of Gated-four-probed devices is used. The variation of R_{cont} is excluded from the variation of μ_{int} . Accordingly, previously reported behavior of μ_{ext} may be strongly influenced by the variation of R_{cont} during gas sensing.

In Fig. 6-4(a), the R_{film} and R_{cont} extracted from Gated-four-probed devices are plotted as a function of NH_3 concentration. The extraction method was proposed by P. V. Pesavento *et al.*[13, 18] The R_{cont} is the sum of total contact resistance from the source side and the drain side. Fig. 6-4(a) shows that the variation of R_{cont} is more drastic than that of R_{film} in the variation of NH_3 concentrations. Since μ_{ext} is extracted from total turn-on resistance including R_{film} and R_{cont} , the variation of R_{cont} during gas sensing may give rise to a significant change of μ_{ext} , especially when R_{cont} is compared to the value of R_{film} . To quantitatively discuss the influence of R_{cont} on μ_{ext} , the following equations were used to extract μ_{ext} and μ_{int} :

$$\mu_{int} = \frac{L}{WC_G(V_G - V_{th}) \cdot R_{film}} \quad (1)$$

$$\mu_{ext} = \frac{L}{WC_G(V_G - V_{th}) \cdot (R_{film} + R_{cont})} \quad (2)$$

$$\frac{1}{\mu_{ext}} = \frac{1}{\mu_{int}} + \frac{WC_G(V_G - V_{th}) \cdot R_{cont}}{L} \quad (3)$$

where C_G is the gate capacity per unit area, L is the channel length, and W is the channel width.

In Fig. 6-4(b), measured and estimated field-effect mobility are plotted as a function of NH_3 concentration. It can be found that μ_{ext} exhibits a larger variation than μ_{int} . In addition, the influence of channel length on the observed μ_{ext} is also considered. The long channel of Gated-four-probed devices ($L = 1200 \mu\text{m}$) produced a larger R_{film} compared to R_{cont} , which reduced the influence of R_{cont} on the total resistance and on μ_{ext} . When the device channel length was reduced to $500 \mu\text{m}$ or $100 \mu\text{m}$, it was expected that R_{cont} would influence μ_{ext} more significantly. We estimated the μ_{ext} of devices with different channel lengths by reducing L in Eq. (3). R_{cont} , μ_{int} , and V_{th} were assumed to be independent of channel length and was obtained from Gated-four-probed devices. The estimated μ_{ext} for devices with channel lengths of $500 \mu\text{m}$ and $100 \mu\text{m}$ are shown in Fig. 6-4(b) for comparison. Obviously, when channel length decreases, the variation of μ_{ext} becomes more pronounced and exhibits a strong dependence on NH_3 concentration.

In summary, pentacene-OTFTs were used as a “multi-parameter” gas sensor which showed a high sensitivity to NH_3 gas. With less than 0.5 ppm NH_3 molecules, OTFTs performed significant turn on current reduction and threshold voltage shift. With the aid of Gated-four-probed OTFTs, the influences of contact resistance and pentacene bulk resistance on the sensing behavior were firstly separately discussed. The current

reduction was not only due to the decreasing of carrier transport mobility but also strongly influenced by carrier injection properties. Polar NH₃ molecules may reduce carrier injection at metal/organic interface and enlarge the contact resistance. When the channel length is scaled down, the influence of contact resistance on turn on current and on external field-effect mobility is more pronounced. It is clearly demonstrated that the OTFT sensing regions include pentacene film via grain boundaries and the metal/organic interface. Gated-four-probed structure successfully separates the variation of these two regions and provides more parameters for monitoring gas sensing.



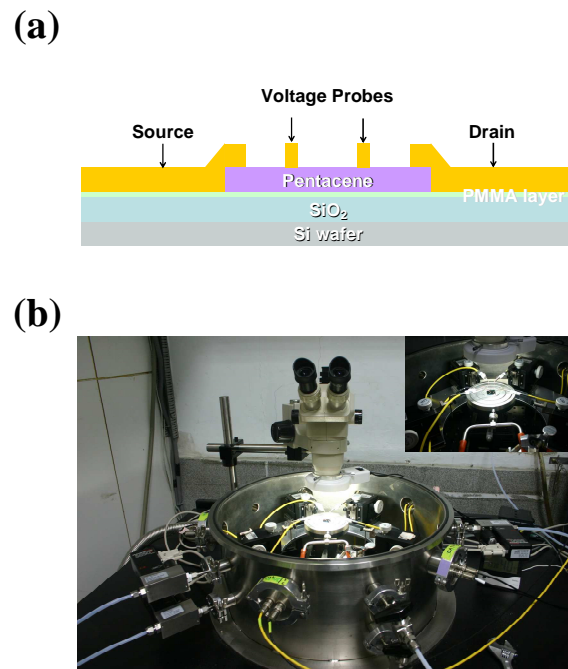


Fig. 6-1 (a) The geometry of Gated-four-probed OTFTs, and (b) the photo image of gas sensing chamber.



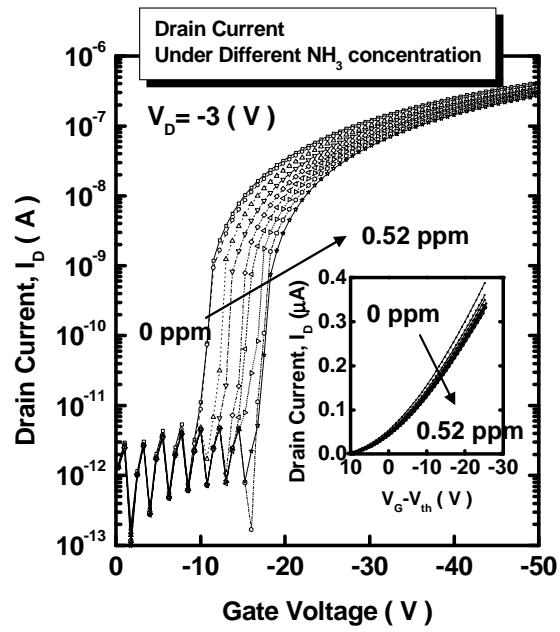
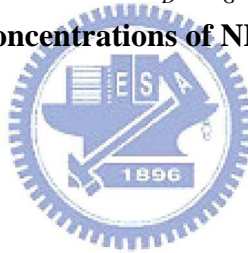


Fig. 6-2 Transfer characteristics ($I_D - V_G$) of Gated-four-probed OTFTs with varied concentrations of NH₃ gas.



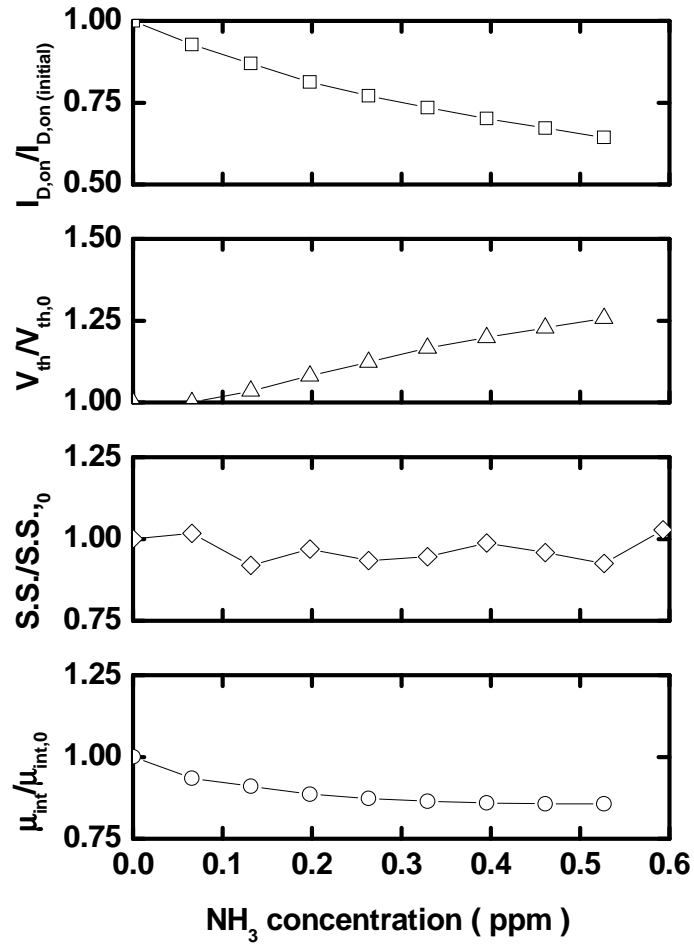


Fig. 6-3 Normalized turn-on current ($I_{D,on}$), threshold voltage shift (ΔV_{th}), subthreshold swing ($S.S.$), and intrinsic mobility (μ_{int}) as a function of NH_3 concentration. $I_{D,on}$ is extracted at $V_D = -3 \text{ V}$, $V_G = -50 \text{ V}$ and μ_{int} is extracted at $V_D = -3 \text{ V}$, $V_G - V_{th} = -25 \text{ V}$.

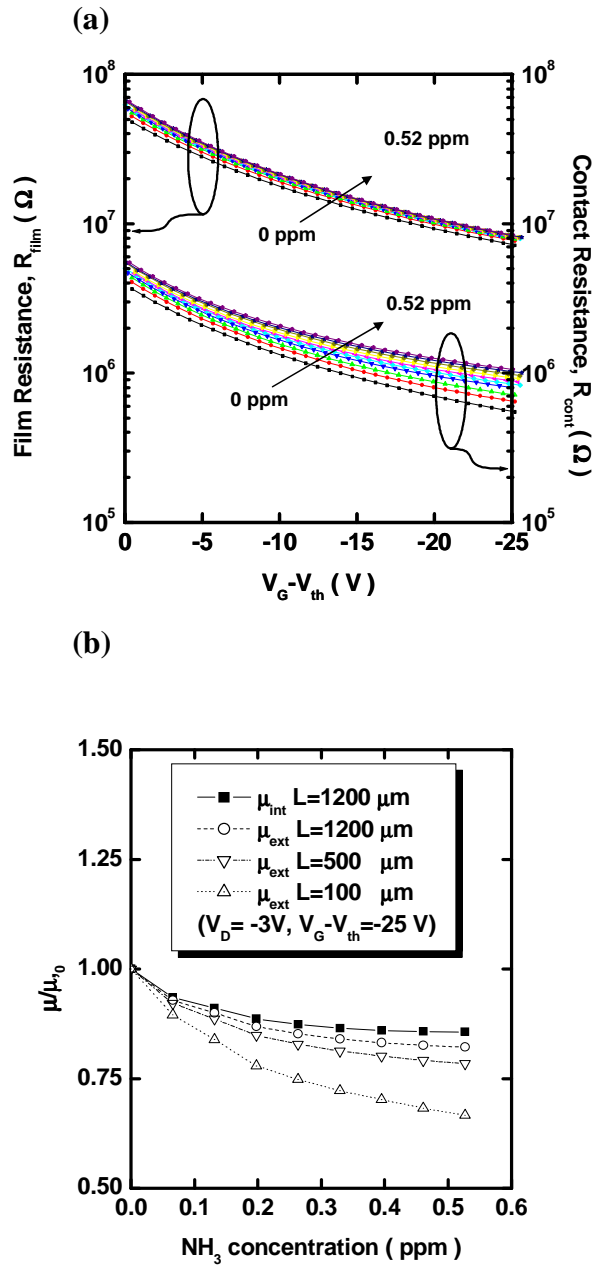


Fig. 6-4 (a) Pentacene film resistance (R_{film}) and contact resistance (R_{cont}) are plotted as a function of $V_G - V_{th}$ under different NH_3 concentrations. (b) The measured ($L=1200\mu m$) and estimated ($L=500\mu m$ and $100\mu m$) intrinsic mobility (μ_{int}) and extrinsic mobility (μ_{ext}) of different channel lengths are plotted as a function of NH_3 concentration.

Chapter 7

Vertical Channel Organic Thin Film Transistors with Meshed Electrode and Low Leakage Current

7-1. Introduction

Recently, OTFTs have drawn much attention due to its potentially applications on flat panel display or flexible electronics.[1-3] To improve the OTFT performances, many methods such as the surface treatment, new electrode material, and new dielectric materials were proposed.[4-6] In addition to increase the output driving current, it was also essential to lower down the driving voltage. As a result, new device structures with short channel length were proposed.[7-12] With high resolution lithography systems such as the G-line photolithography, the I-Line photolithography, and the e-beam direct writer, the organic devices with nano-scale channel length have been realized. The device operation voltage could be scaled down to less than ten volts. However, production cost was increased by using these advanced lithography system. To develop short-channel OTFTs with low production cost, a vertical structure with top drain contact and bottom source contact (TBC-OTFTs) was demonstrated.[11-12] Influences of the electrode materials and electrode configurations have been discussed, while the unsaturated characteristics required further improvement.

In this paper, we firstly investigated the conducting mechanism of the TBC-OTFTs. The unsaturated characteristics were found to be governed by the Fowler-Nordheim tunneling. The F-N tunneling from source to drain reduced the control ability of gate bias and increased the leakage current of the devices. To

suppress the tunneling effect, TBC-OTFTs with meshed source electrode were proposed. By utilizing the fringing field effect generated by the gate bias around the source electrode, the tunneling effect can be significantly suppressed. As a result, better saturated turn-on characteristics and smaller leakage current were obtained.

7-2. Device Fabrication

The process flows are illustrated in Fig. 7-1(a)-(e). In Fig. 7-1(a), we grown the thermal oxide about 1000Å on the slightly boron doped Si wafer, the wafer resistance is about 15-25 ohm-cm. Then, the bi-layer metals (Pd/Ti) are deposited as source and drain electrodes by the E-gun deposition system (ULVAC EBX-10C). The deposition pressure is at 3×10^{-6} torr with the deposition rate of 0.5~1 Å/sec. The thicknesses of the Pd and Ti layers are 1000Å and 10Å, respectively. The source electrode is then patterned by photolithography process after metal deposition and shown in Fig. 7-1(b). With the etching in the dilute aqua regia ($\text{HNO}_3:\text{HCl}:\text{H}_2\text{O}=1:3:4$ at temperature $>70^\circ\text{C}$), the electrode pads are formed. The pentacene material that we used is obtained from the Aldrich without any purification; the as-received material is placed in the thermal coater for the deposition directly. In Fig. 7-1(c), we use the photoresist to define the active regions, we may also use the shadow mask to define pattern of the pentacene film. During the pentacene deposition, the substrate temperature is heated to 70°C . The deposition rate is 0.5Å/sec and the pressure is less than 3×10^{-6} torr. Then, the window-like source electrode is fully covered with 100nm pentacene film. On the top of the pentacene film, we mount the other shadow mask for depositing drain electrodes. As illustrated in Fig. 7-1(d), we deposit the Au (50nm) via the thermal evaporator as the drain electrode pad. Several individual drain electrodes are formed on the pentacene film as shown in Fig. 7-1(e). The short-channel TBC-OTFTs, in which the drain electrodes were overlapped with

the source electrodes, were defined as the Group-A devices. The long-channel TBC-OTFTs were defined as the Group-B devices in which the drain electrodes were far separated from the source electrodes. The top-view image that captured from the microscope CCD is shown in [Fig. 7-2](#).

Then, we fabricated the TBC-OTFTs with meshed-like source electrodes by the process flow described above. The only difference was that we replaced the window-like source electrodes to be the meshed-like source electrodes. The top-view image of the devices with meshed-like source electrodes is shown in [Fig. 7-3](#).

7-3. Result and Discussion

Firstly, the output characteristics of the Group-A devices are shown in [Fig. 7-4\(a\)](#). It is obviously that unsaturated drain current is observed. This is consistent with previous reports on short channel organic thin film transistors.^[13] [Fig. 7-4\(b\)](#) depicts their transfer characteristics, higher ON/OFF current ratio can be achieved when the drain electrode bias is higher. For Group-B devices, apparently different output characteristics are observed in [Fig. 7-5](#). Very well saturated behavior can be obtained under large drain bias. To understand this difference, we consider the carrier transport mechanism in OTFTs. It has been well accepted that the carrier transport in OTFTs strongly affected by two distinct mechanism. One is the carrier injection through the barrier at metal/organic interface. The other is the multiple trapping mechanisms when the carrier transport inside the organic thin film.

For Group-B devices, actually the current path follows long-channel current path that carriers have to travel a certain lateral distance from source side to drain side. As a result, conventional long-channel device characteristics are obtained. For Group-A devices, carriers inject from source side and transport inside the pentacene layer through a very short range ($\sim 100\text{nm}$) then arrive the drain side. It is plausible that

under the large electric field, carrier may tunnel through the potential barrier between metal contact and pentacene film. The process can be described by Fowler-Nordheim transport as the following equation:[14]

$$I_D \propto F \cdot e^{-\frac{F_0}{F}}$$

Where $F=|V_D/L|$, V_D is drain bias, L is the channel length and F_0 is a potential barrier related constant. If the Fowler-Nordheim transport is the dominant mechanism, linear relationship can be found in the $\ln(I_D/V_D)$ v.s. $1/|V_D|$ plot. In Fig. 7-6(a) we show the $\ln(I_D/V_D)$ v.s. $1/|V_D|$ plot for Group-A devices. Very clear linear relationship can be found. For Group-B devices, as shown in Fig. 7-6(b), no obvious dependence can be found. This comparison clearly demonstrates that Group-A devices and Group-B devices exhibit totally different carrier transport mechanism. This also explains their different behavior in the output characteristics.

Since the vertical devices with ultra short channel length (Group A devices) exhibit Fowler-Nordheim transport mechanism, it is found that increasing the gate control ability can improve the device performance. Therefore, we further modify the source electrode pad to be meshed-like shape as illustrated in Fig. 7-3. The small pinholes arrayed on the electrode allow gate electric field penetrate into the channel region and give better control ability. The output characteristics of this new device are shown in Fig. 7-7(a), It is found that relatively good performance can be obtained even when the operation voltage is smaller than 5 V. Their transfer characteristics are also depicted in Fig. 7-7(b), improved subthreshold swing and reduced leakage current can be found by comparing with those in Fig. 7-4(b).

To further study the influence of the source electrode shape on the leakage current, the electric field distribution was simulated by the Silvaco TCAD (ATLAS and ATHENA). By setting the gate bias as 20 V and the drain bias as -20 V, the

electric field distribution of the Group A devices is shown in Fig. 7-8 (a). A large electric field higher than 2 MV/cm is located between the drain and the source electrode. It is very possible that this large electric field causes tunneling effect or barrier lowering effect to produce a large leakage current from the source to the drain. The TBC-OTFT with meshed-like source electrodes, on the other hand, exhibits a very different electric field distribution as shown in Fig. 7-8 (b). Significant gate-field fringing effect is observed. It reduces the electric field around the source electrodes and blocks the high field from the source to the drain. The result explains the reduced leakage current in the TBC-OTFTs with meshed-like source electrode and gives an insight of the OTFT leakage mechanism.

In summary, we used a simple method to fabricate the nano-scale vertical channel organic devices without high resolution photolithography process. The process can be completed by only using shadow mask and simple aligner. Channel length is defined by the pentacene thin film thickness and the source/drain electrode configuration. When the drain electrode pad is overlapped with source electrode, ultra-short channel device characteristics are observed. Fowler-Norheim transport mechanism is found to dominate the output characteristics because of the large electric field located in the channel region. When the drain electrode is not overlapped with source electrode, typical long-channel device performances are observed and the carrier transport in pentacene layer follow conventional multiple trapping theory. To further enhance the gate control ability and lower down the leakage current of the ultra-short channel devices, we introduced the meshed source electrode. In the renewed device, low drain voltage (<10 V) and higher ON/OFF current ratio (about 4 orders) can be successfully obtained. Further studies are in the progress to discover and identify more specific short channel properties for TBC-OTFTs.

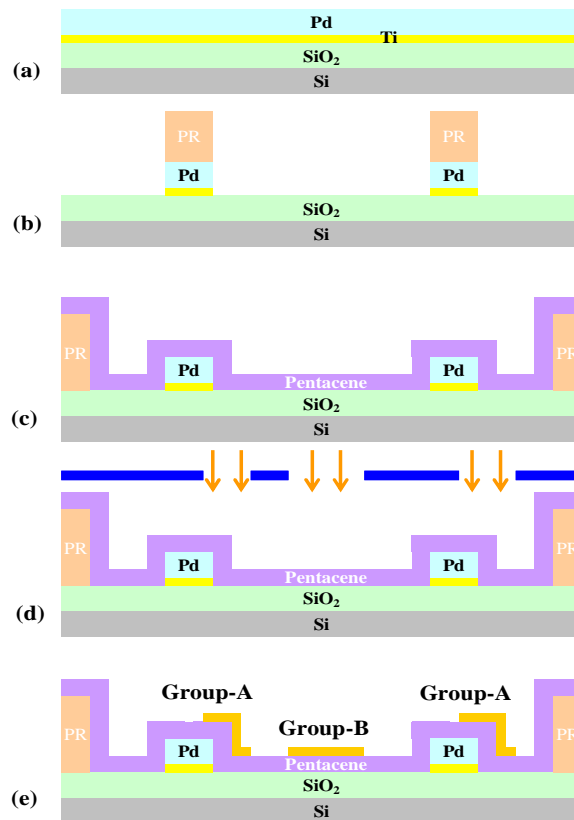


Fig. 7-1 The structure and the process flow of vertical-channel organic thin film transistors with top drain contact and bottom source contact. (TBC-OTFTs).

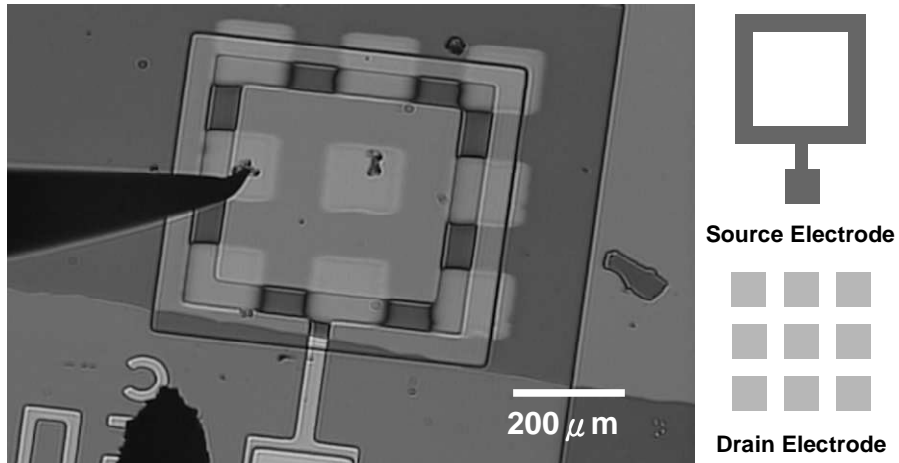


Fig. 7-2 Topview microscope images of the TBC-OTFTs. The shapes of source/drain electrodes are also shown.

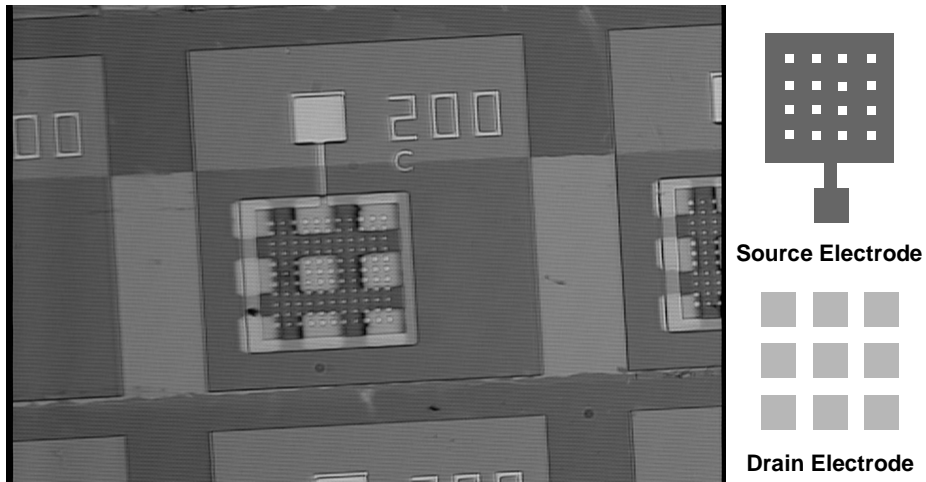
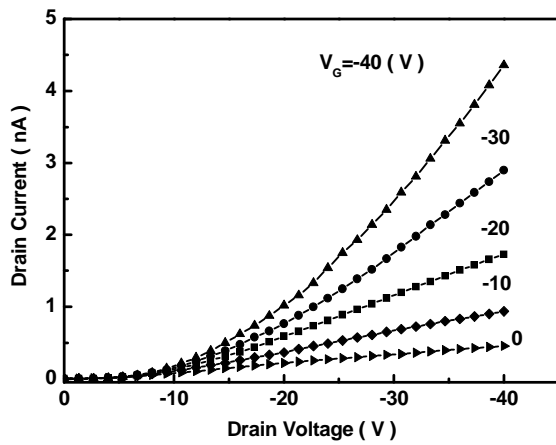


Fig. 7-3 Topview microscope images of the TBC-OTFTs with meshed source electrode. The shapes of the bottom source and top drain electrode pad are also shown.

(a)



(b)

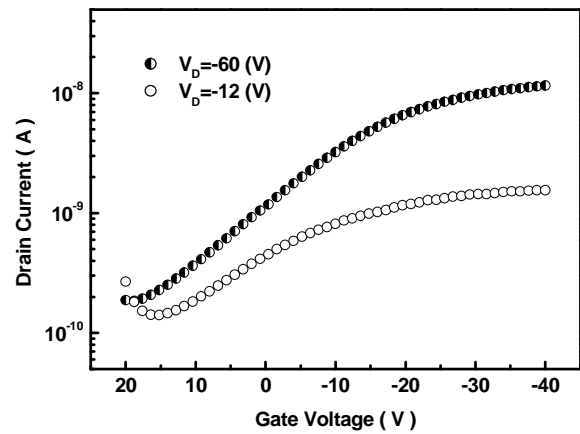


Fig. 7-4 (a) Output characteristics and (b) transfer characteristics of Group-A TBC-OTFTs.

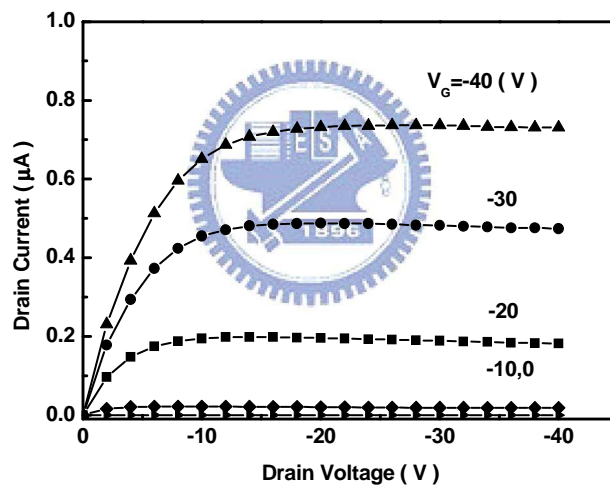


Fig. 7-5 Output characteristics of Group-B devices.

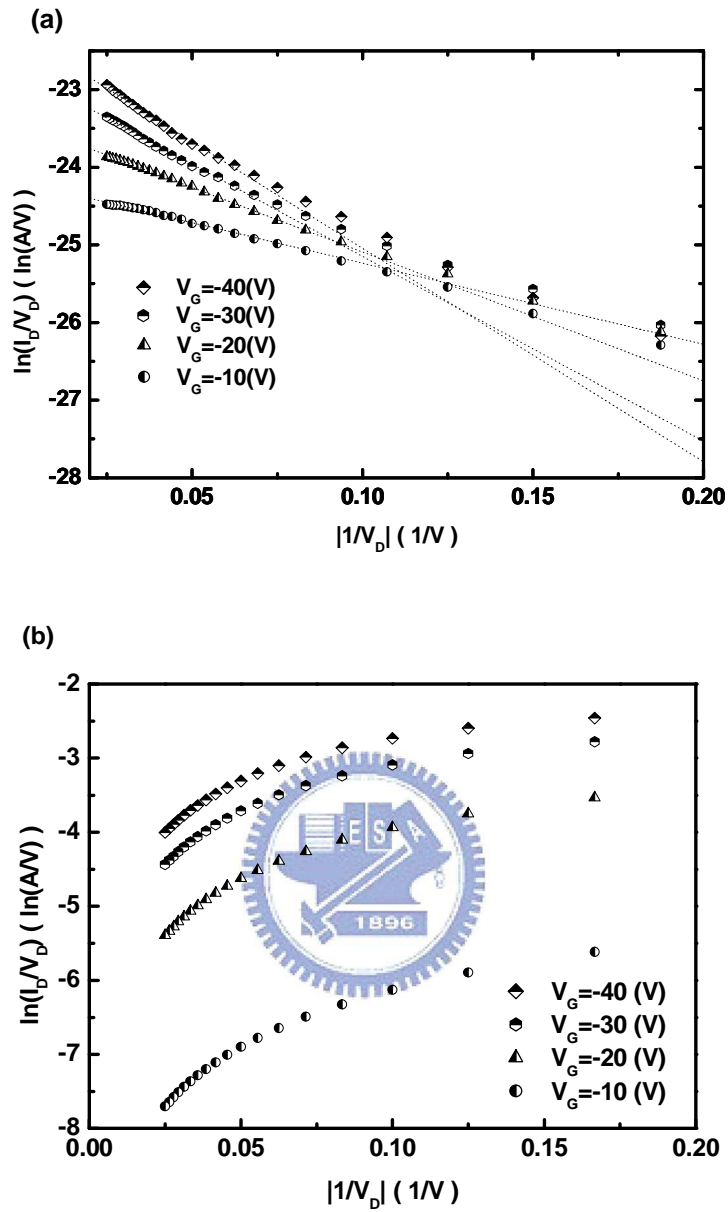
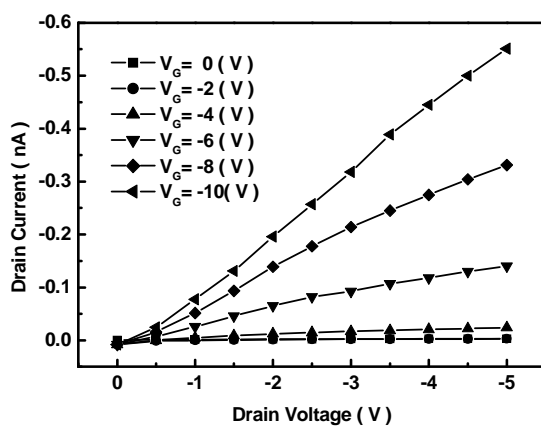


Fig. 7-6 The $\ln(I_D/V_D)$ v.s. $1/|V_D|$ plots for: (a) Group-A devices with ultra short channel length and (b) Group-B devices with long channel length.

(a)



(b)

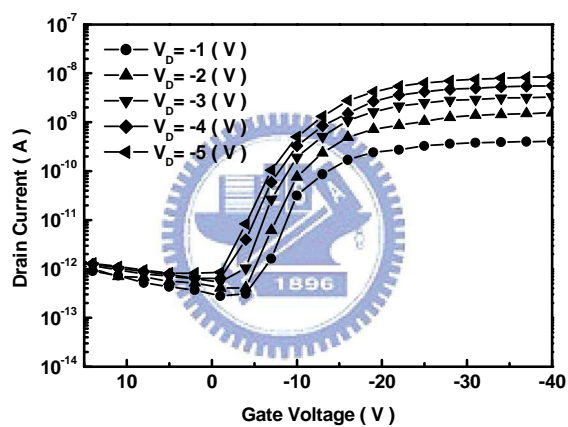


Fig. 7-7 (a) The output characteristics and (b) the transfer characteristics of TBC-OTFTs with meshed source electrode.

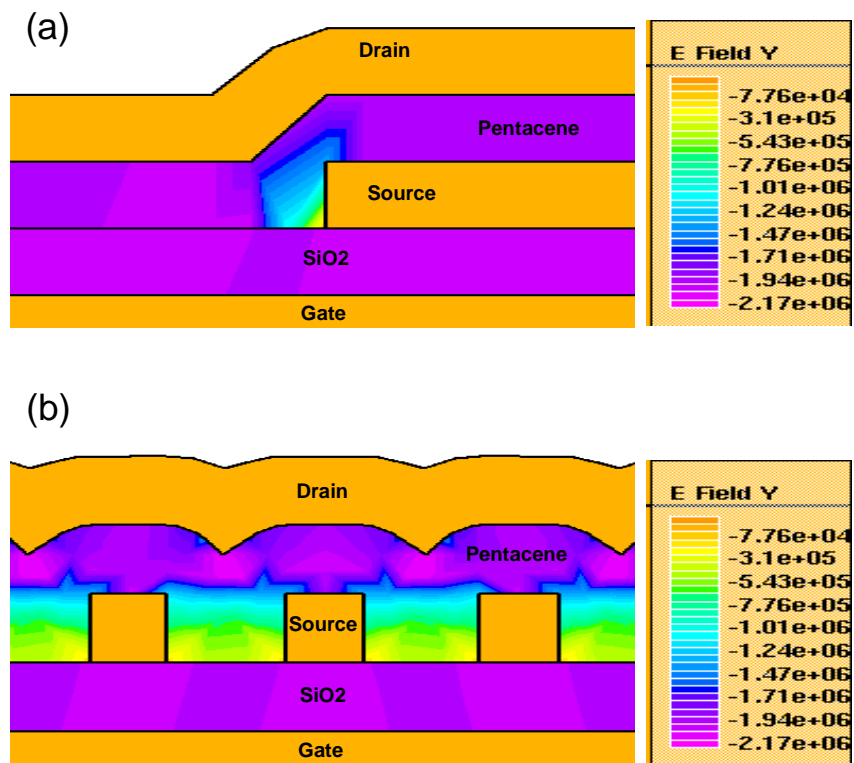


Fig. 7-8 The simulated electric field distribution of: (a) Group-A TBC-OTFTs and (b) the TBC-OTFTs with meshed source. The gate bias is 20V and the drain bias is -20V, the source is connected to ground.

Chapter 8

Conclusion

Low-temperature gate-dielectric, AlN films, is proposed for OTFTs. The pinhole free, smooth and extremely thin AlN film can be deposited by the RF-sputtering system at low deposition temperature. The dielectric leakage was significantly low, and the AlN has a surface free energy that is similar to that of the pentacene film. It can be concluded that lowering the AlN deposition temperature gives smaller leakage current and larger pentacene grain size. The field effect mobility is accordingly improved. The process is promising for the development of low-temperature OTFTs. The Ar/N₂ flow ratio in the sputtering process was demonstrated to be a key parameter in reducing AlN gate leakage. Poole-Frenkel-related leakage is suppressed as the electric field increased. Based on experimental result, the low-voltage and high performance OTFTs are realized. With the thinner AlN gate-dielectric, lower substrate temperature, and higher Ar:N₂ ratio, the AlN-OTFTs can be operated at low-voltage (about 5V). From the series of the experiments, the highest field effect mobility is 1.67cm²/V-sec, the lowest subthreshold swing is 104mV/decade, and the lowest threshold voltage -1.3V, respectively. The high on/off current ratio about 10⁶ were all observed from these AlN-OTFTs. According to the mentioned electric properties, it is demonstrated that the AlN-OTFT has potential application in low-voltage and rapid-switching organic transistors.

The OTFTs with solution-based PMMA gate-dielectrics and investigate the effects of UV-light treatment on PMMA gate-dielectrics. With the UV-light treatment, the threshold voltage and the subthreshold swing will be significantly altered, but the field-effect mobility remains almost unchanged. When the light-irradiation on these OTFTs, the devices with UV-light treatment will show a larger threshold

voltage shift and a larger photo responsivity than those devices without UV-light treatment. In order to investigate the effect of UV-light treatment on OTFTs characteristics, the material analysis and the dielectric leakage-current measurement are proceeded. It is found that the variation of the semiconductor layer and the trapping in the dielectric layer should not be the dominated factors. By the time-dependent analysis of threshold voltage shift and photo-generated current, the saturated time and the recovering time show a strong correlation to the gate-voltage. That implies the electric-field in the organic semiconductor film will influence the behavior drastically. It is most probably the UV-light treatment may create the charged traps at the interface of the PMMA-dielectric and the organic semiconductor, which will result in a build-in electric-field in the organic semiconductor near the PMMA gate-dielectric. Hence, the OTFTs with UV-light treatment will show different characteristics, such as a faster saturation time and a longer recovering time.

We constructed a gas-sensing system and investigated the interaction of pentacene film to NH_3 gas via the gated-4-probes OTFT. In our observation, when NH_3 gas interacted with the OTFT, both the contact resistance and the pentacene film resistance are increased, which resulted in the reduction of drain-current. The threshold voltage is also shifted negatively to a larger value; however, the subthreshold swing was almost unchanged. According to our estimation, the increase of pentacene-film resistance will reduce the intrinsic field-effect mobility. It should be attributed to the interaction of NH_3 gas and pentacene film will create additional traps in the pentacene grain, which will increase of grain boundary (GB) barrier height. On the other hand, based on the negatively increased threshold voltage and the almost unchanged subthreshold swing, the NH_3 shows a character of “hole withdrawing” in pentacene film but do not influence the distribution of

interface trap significantly. We suggest that the strong interaction between NH_3 gas and OTFT may be connected to the highly polarized NH_3 molecule, but further work is needed to determine the detail of related mechanism.

In this investigation, the novel vertical organic thin film transistors (VOTFTs) and the Top-bottom-contact OTFTs was proposed. With the metal shadow-mask and the simple photolithography, the short channel (channel length less than 100nm) OTFTs with vertical structure was fabricated. As well as the common short channel transistors, the unsaturated drain current (under high drain-voltage) was observed in the proposed VOTFTs. It is found that the Fowler-Nordheim tunneling dominated the carrier transport in VOTFTs, resulting in the unsaturated drain-current. To further improve the VOTFTs performance, the modified meshed-source pad was proposed. The control of the gate bias was enhanced and the drain voltage can be significantly reduced. The modified VOTFTs can be operated at low drain-voltage and low gate-voltage (about -5V) and the on/off current ratio was also increased from 10^2 orders to 10^4 orders.